POLITECNICO DI MILANO

Scuola di Ingegneria dei Processi Industriali

Dipartimento di Chimica, Materiali e Ingegneria Chimica “Giulio Natta”

MASTER OF SCIENCE IN MATERIALS ENGINEERING
AND NANOTECHNOLOGY

Critical Analysis of Hydrogen Permeation Techniques. Application to Different Steel Microstructures

Supervisor: Prof. Fabio Maria Bolzoni

Assistant supervisors: Prof. Gabriele Fumagalli
Ing. Giorgio Re
Ing. Ehsan Fallahmohammadi

Giacomo Benassi

ID 782526

Academic year 2012 – 2013

RINGRAZIAMENTI

Desidero innanzitutto ringraziare il Professor Fumagalli e l'Ingegner Re per la pazienza avuta, per la passione e per le competenze che mi hanno trasmesso durante questo progetto, facendomi crescere. Un ringraziamento doveroso anche ad Ehsan, con cui ho condiviso le gioie e i dolori dell'attività sperimentale, al Professor Bolzoni, per i preziosi consigli che mi ha fatto pervenire quando ne ho avuto bisogno e al Professor Lazzari, che mi ha offerto l'occasione di poter approfondire le mie conoscenze oltre il mondo universitario. Non posso inoltre dimenticare di ringraziare tutti i professori e il personale del dipartimento che mi hanno assistito e i colleghi Cescor, in particolare Virgilio e Marco, che mi hanno aiutato in questi ultimi mesi ad inserirmi nell'attività lavorativa, dandomi la serenità per finire di scrivere questa tesi.

Durante questi anni in università ho avuto la grande fortuna di avere vicino amici che mi hanno aiutato, incoraggiato e fatto passare tantissimi momenti felici. Un grazie speciale ad Albi, Andrea, Bea, Guido, Marco, Mich, Robi, Sama, Sofia, Teo e Valeria, spero che le avventure passate insieme finora siano solo un inizio.

Grazie a Marco, che mi ha insegnato i valori dell'amicizia e a cui devo veramente tantissimo, ad Elia, che purtroppo non posso vedere quanto vorrei ma che ha sempre rappresentato per me un'isola felice, a Orso, Desa e Sara, se ripenso a quante ne abbiamo passate dalla 1ª C..

Je, mi hai donato talmente tanto, hai avuto così tanta pazienza in questi anni da non sapere come ringraziarti (però mi raccomando, a questa laurea comportiamoci bene!).

Infine devo ringraziare la mia famiglia, mamma, papà, Fede e ovviamente Rex, senza di voi tutto questo non sarebbe stato possibile. Ve ne sono grato ogni giorno.

TABLE OF CONTENTS

LIST OF FIGURES

LIST OF TABLES

ABSTRACT

The hydrogen diffusion understanding has assumed great importance due to hydrogen embrittlement related problems.

This thesis has investigated, with electrochemical permeation tests, the hydrogen diffusion into API 5L X65 pipeline steel with three metallurgical microstructures. It has a dual purpose:

- critical analysis of hydrogen permeation techniques;
- the application to three different microstructures.

The main results are listed below.

The charging transient analysis (Devanathan and Stachurski's method standardized in ISO 17081) gives an apparent diffusion coefficient D_{app} strongly influenced by metal-hydrogen trapping effect and cathodic surface electrochemical alteration. Indeed D_{app} values are affected by high dispersion, they are insensitive to microstructural variations and they result at least one order of magnitude lower than lattice diffusion coefficient.

Diffusion coefficient measured during the first part of discharge is sensitive to microstructural variations, it is less influenced by trapping and electrochemical alterations, it is higher than D_{app} and only slightly lower than D_L estimated with other procedures.

Cathodic current partial charge and discharge procedure (Zakroczymski's method) shows less experimental data dispersion, it gives experimental curves perfectly symmetric (intrinsic reproducibility) which follow diffusion Fick's laws. The obtained D values can be reasonably assumed as "true" lattice diffusion coefficient of materials. These values are sensitive to microstructural variations.

Martensitic (quenched) X65 steel has D_L about 3 times lower than bainitic (quenched and tempered) X65 steel and about 14 times lower than ferritic pearlitic (annealed) X65 steel.

In conclusion, the electrochemical experimental procedure adopted in this project consist of: 1) D_{app} estimation during hydrogen charge; 2) D_L estimation during hydrogen partial charge and discharge; 3) D_L verification and hydrogen content estimation (in lattice and reversibly trapped sites), during hydrogen discharge. This procedure leads to reliable and meaningful results in permeation phenomena.

RIASSUNTO DELLA TESI

La comprensione delle modalità di diffusione dell'idrogeno nei materiali metallici ha acquisito una notevole importanza a causa delle problematiche legate all'infragilimento da idrogeno. Ciò ha portato alla formulazione di modelli matematici descriventi il fenomeno e di procedure sperimentali opportunamente allestite per approfondire le conoscenze su di esso.

Nel presente progetto di tesi sono state eseguite prove di permeazione di tipo elettrochimico su un acciaio al carbonio per condotte del tipo API 5L X65 trattato termicamente per ottenere tre diverse microstrutture. Il progetto ha avuto un duplice scopo:

- l'analisi critica delle tecniche di misurazione del coefficiente di diffusione dell'idrogeno;
- l'applicazione di queste tecniche a tre differenti microstrutture metallurgiche.

I risultati dei transitori di carica, indicati nella norma ISO 17081, forniscono un coefficiente di diffusione apparente D_{app} fortemente influenzato dagli effetti dell'intrappolamento dell'idrogeno nel metallo e dalle alterazioni elettrochimiche superficiali del catodo. I valori di D_{app} infatti sono affetti da elevata dispersione, non sono sensibili alle variazioni microstrutturali e risultano essere almeno un ordine di grandezza più bassi del coefficiente di diffusione reticolare.

I coefficienti di diffusione misurabili durante la prima parte della scarica di idrogeno sono meno influenzati dall'intrappolamento e dalle alterazioni elettrochimiche, sono sensibili alle variazioni microstrutturali e risultano essere solo leggermente inferiori ai coefficienti di diffusione reticolare D_L stimati mediante altre procedure.

I transitori di carica parziale e di scarica parziale, ottenibili mediante la procedura suggerita da Zakroczymski, forniscono delle curve sperimentali che seguono molto bene le curve teoriche secondo il modello di Fick, mostrano un'intrinseca riproducibilità sullo stesso provino e una contenuta dispersione su provini diversi. Il coefficiente di diffusione così ottenuto può essere ragionevolmente considerato il "vero" coefficiente di diffusione reticolare D_L. Questi valori sono sensibili alle variazioni microstrutturali e, anche se leggermente maggiori, sono paragonabili a quelli desumibili nella prima fase di scarica dell’idrogeno.

In particolare, è stato misurato un D_L per l'acciaio X65 martensitico (temprato) circa 3 volte più basso dell'acciaio X65 bainitico (temprato e rinvenuto) e circa 14 volte più basso dell'acciaio X65 ferritico-perlitico (ricotto).

In conclusione la procedura sperimentale di tipo elettrochimico adottata consiste: 1) stima del D_{app} nella fase di carica dell’idrogeno; 2) stima del D_L nelle fasi di carica parziale e scarica parziale dell’idrogeno; 3) verifica del D_L e stima della quantità di idrogeno, permeante sia nel solo reticolo sia anche attraverso trappole reversibili, nella fase di scarica

dello stesso. Tale procedura fornisce risultati affidabili e significativi riguardo i fenomeni di permeazione poiché è in grado di eliminare gli elementi di disturbo presenti e di separare i fenomeni reticolari da quelli di intrappolamento reversibile.

INTRODUCTION

This thesis is part of a research activity devoted to study the hydrogen diffusion in pipeline steels.

The background of this research is related to previous studies of the same research group in which pipeline steel specimens has been electrochemically charged with hydrogen and submitted to mechanical tests, fatigue and fracture toughness. One of the main results of this research program was that the effect of the hydrogen on mechanical properties of steels can be related to the diffusion rate of atomic hydrogen.

The present research project is carried out with permeation tests. In the previous thesis the efforts were focused on the diffusion coefficient measurement, and in particular on the development of a standard procedure to measure it properly. This thesis represents a continuation of this effort, and it consists to study the hydrogen diffusion and trapping processes into API 5L X65 pipeline steel with three metallographic microstructures by means of the permeation tests. It has a dual purpose:

- critical analysis of hydrogen permeation techniques;
- the application to three different steel metallurgical microstructures.

The present thesis work is composed by seven chapters.

In the first chapter the role of corrosion and hydrogen embrittlement in Oil & Gas industry are presented, with particular attention to sour environment, hydrogen damages and relation between hydrogen and mechanical properties.

In the second chapter, the interaction between hydrogen and steels (hydrogen evolution and adsorption/absorption), starting from the solution to the absorbed state into the metal, with appropriate models and theories, is illustrated. Then, relations between hydrogen solubility and relevant environmental variables are pointed out.

The third chapter presents mathematical models which are used to describe hydrogen diffusion, with specific equations and relations. Diffusion with and without traps is distinctly considered.

The fourth chapter is dedicated to trapping phenomenon. Various trapping definitions and classifications are proposed and a literature research concerning microstructure-hydrogen diffusion relationship are presented, with appropriate final comments.

The fifth chapter deals with permeation techniques. In particular, Devanathan and Stachurski's experience is analyzed in detail, because it represents the starting point for all the following hydrogen permeation experiments. Then evolutions of this technique are considered, with special attention to ISO 17081 standard and Zakroczymski (“partial transient”) procedure.

In the sixth chapter the heat treatment of the material, the metallurgical characterization of different microstructures and the sample preparation are explained. The second part is dedicated to the explanation of the peculiar permeation procedure adopted including detailed information on data acquisition and storage.

The seventh chapter includes all the results with the related discussions. The chapter is divided in the analysis of permeation techniques described previously and their application to different steel microstructures. Some relevant conclusions are pointed out.

1) HYDROGEN EMBRITTLEMENT AND DAMAGES

1.1 Corrosion in oil & gas industry

Nowadays corrosion is one of the main problems of Oil & Gas industry because it represents a risk for the environment and for the employees of related companies. The costs of prevention, monitoring and remedial actions due to corrosion phenomena are remarkable. In order to lower these costs oil companies invest substantial resources to develop more performing materials and to increase the know-how about plant protection against corrosion. Moreover the huge increase of oil and gas demand is leading to exploit hydrocarbon resources in more severe conditions (e.g. arctic sites or deep off-shore). This represents a further engineering challenge for corrosion engineers too.

In the oil & gas industry corrosion engineers must face problems that are common to many other environments, such as general corrosion, corrosion by galvanic contact, erosion corrosion, microbiological corrosion, and others that are specific to the oil industry, as CO_2 and H_2S corrosion (corrosion in sour environment) [5], [6], [7].

The present work will deal with a specific aspect of the corrosion in sour environment, i. e. the penetration and diffusion of atomic hydrogen into metallic materials causing embrittlement.

Moreover hydrogen embrittlement can be promoted by cathodic reaction of hydrogen evolution in specific condition, as acid corrosion (pickling) or cathodic polarization (overprotection).

1.2 Sour service

In hydrocarbon environments, hydrogen embrittlement acts preferentially in sour service, a condition given by specific values of H_2S and CO_2 concentration. In Figure 1.1 sour service definition according to new NACE Mr0175/ ISO 15156 standard diagram is represented [1], which easily allows to distinguish between different service zones. The standard also gives guidance in the selection of proper material.

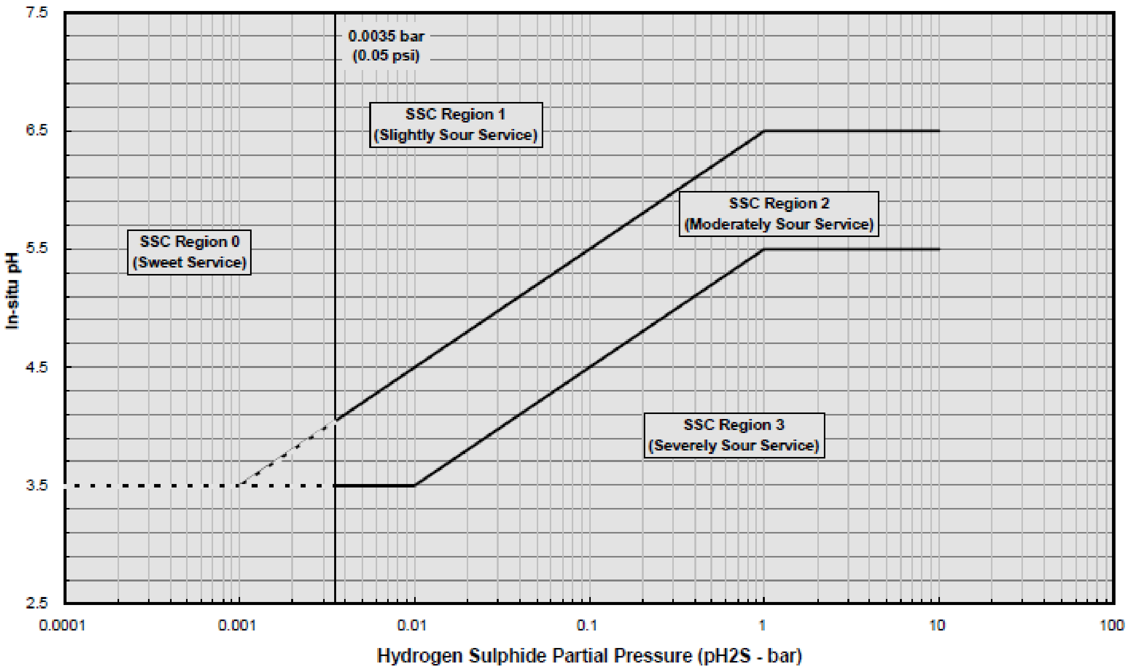

Figure 1.1 - ISO 15156 diagram for the environmental severity [1], [2].

The diagram considers H_2S partial pressure on the x-axis and in-situ pH on the y-axis (function of CO_2 concentration). It is divided into four regions (0, 1, 2, 3), representing environmental aggressiveness from the sweet service to the severely sour service.

Specific effects of H_2S in the hydrogen solubility will be expressed in detail in Chapter 2.

Also the temperature plays an important role, indeed the embrittling effect of hydrogen is reduced at higher temperature. This benefit can be used for example to decrease material requirements if the temperature of exposition is continuously above 65°C [6].

1.3 Typologies of hydrogen damaging

When condensed water phase and high values of H_2S and CO_2 partial pressure are simultaneously present, carbon steels are susceptible to hydrogen embrittlement. In the following paragraphs how hydrogen atoms can impair steels properties once they enter in the metallic lattice are illustrated.

In order to fully understand the mechanisms of hydrogen embrittlement which cause the damages described below, a substantial analysis should be done. This is not the aim of this thesis and particularly of this introductive chapter, which wants only to contextualize the experimental work done.

1.3.1 Hydrogen induced cracking (HIC)

Hydrogen induced cracking is intended as the deterioration of the properties of the materials caused by hydrogen atoms that enter and diffuse into the metal and which may develop without any residual or applied stress. Atomic hydrogen into the lattice tends to accumulate in particular sites, called trap sites. Segregation bands or elongate inclusions along rolling direction allow accumulation and recombination of hydrogen to form molecular hydrogen H_2. This reaction is characterized by a great expansion of the products and the increased pressure leads to local deformation of the metal.

Formation of microcracks or blisters (Figure 1.2 on the left) don't alter mechanical properties of the material; only the coalescence of blisters or microcracks activates the so-called stepwise cracking (SWC), with the typical stepping form shown in Figure 1.2 on the right.

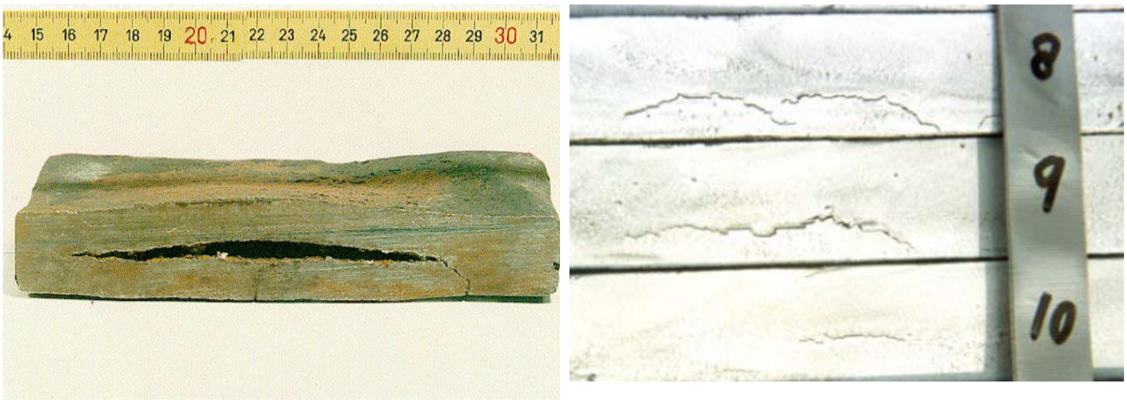

Figure 1.2 - On the left, example of blistering; on the right, SWC typical form [2].

In order to limit HIC, low inclusion content material should be used, especially without elongated manganese sulfide inclusions. Therefore steels to be used in sour environments are produced with a very low content of S and P and are treated with calcium or rare earth in order to produce spheroidal inclusions.

1.3.2 Sulfide stress cracking (SSC)

Sulfide stress cracking occurs on susceptible metals when specific environmental conditions are verified, such as H_2S presence and external applied stress or also residual stress. Cracking happens due to the interaction between tensile stresses (not critical in sweet environment) and atomic hydrogen inside the metal. Sour service makes the situation critical because H_2S increases greatly the absorption of hydrogen usually present outside the metal, related to corrosion phenomena. This mechanism will be deeply analyzed later. The interaction stress-hydrogen impairs the ductility of the material and enhances the cracking probability.

Relations between sour environment and SSC of low alloy steels can be evaluate in Figure 1.1, referring to ISO 15156 [1] for specific severity and material selection.

The most SSC susceptible steels are high-strength and high-hardness steels. The choice of the proper steel should be done looking the acceptable hardness limits to avoid SCC, such as 26 HRC for quenched and tempered low alloy steels [6].

A particular form of SSC acts in soft areas of heat affected zones of welding, in which staggered small cracks are formed approximately perpendicular to the principal stress (external or residual), resulting in a "ladder-like" cracks array [6]. This SSC form is named stress oriented hydrogen induced cracking (SOHIC).

1.4 Importance of diffusion coefficient in fatigue properties

Fassina at alii [3], [4], [8], [9] investigated the influence of hydrogen on toughness and fatigue properties of API 5L X65 and 2 ¼ Cr 1 Mo steel, namely ASTM A182 F 22. Hydrogen charged and uncharged samples were tested at different temperatures and frequencies.

Hydrogen effect is evident, the hydrogen charge causes embrittlement and crack growth acceleration in all the considered conditions: in particular in fatigue tests, low frequencies allow H to migrate at the crack tip, as a consequence hydrogen embrittlement effect on crack growth rate is enhanced; low temperature reduces the mobility of hydrogen in the lattice (i.e. reduce diffusion coefficient), decreasing the embrittlement effect. The resulting crack growth rate can be expressed as the sum of a mechanical contribution (frequency dependent) and a second due to hydrogen effect (time dependent). When crack growth rate increases, the “mechanical” contribution prevails because hydrogen atoms do not have enough time to accumulate at the crack tip: as a consequence crack growth rate is no longer hydrogen dependent.

In particular the results presented in [6], [7] exhibit a remarkable aspect: the charged specimens show, in da/dN - ΔK diagram, a fatigue crack growth kinetic faster than uncharged ones and a peculiar behaviour, with a plateau similar to "Stress Corrosion Fatigue" [10]. Since the fatigue tests were performed in inert environment, the controlling process (K and time dependent) could not be Stress Corrosion Cracking, but it is probably due to bulk hydrogen diffusion to the moving crack tip.

From these tests emerge the leading role of diffusion rate, strictly related to diffusion coefficient, in the explanation of temperature and frequency influences on the fatigue crack propagation rate.

2) HYDROGEN SOLUBILITY AND DIFFUSION

2.1 Hydrogen evolution and absorption

Hydrogen can be easily picked up by many metals from environment in different situations. Among all the possibilities, relevant examples are:

- if molecular hydrogen H_2 is present in the surrounding environment
- during electrochemical processes when hydrogen develops as reaction products (e.g. pickling or electroplating)
- during cathodic protection (especially in the case of "overprotection")
- in the presence of hydrogenated species (H_3O^+, H_2S, etc..), which can be reduced during corrosive processes

It is possible to divide these cases in two main entry ways: the former is chemical adsorption (or chemisorption) and the latter involves electrochemical reactions.

2.1.1 Chemical adsorption

Due to high temperature, some metallic alloys show an increased solubility of atomic hydrogen. This can be observed during working process or during service.

This phenomena involves chemisorption of H_2 on the surface, which subsequently dissociates in the atomic form:

$$\mathbf{H_2\,(gas) \leftrightarrow H_{2\,ads} \leftrightarrow 2\,H_{ads} \leftrightarrow 2\,H_{abs}}$$

with the concentration H_{abs} following the well-known Sievert's law [11]:

$$\mathbf{C_H = 0.00185\,(P)^{0,5}\exp\left(-\frac{3400}{T}\right)}$$

C_H = concentration of hydrogen atoms into the metal

P = H_2 pressure in the environment

T = temperature

The key of the process is high chemical affinity between hydrogen and metal, H-Me; since the reaction doesn't involve electron exchange, hydrogen solubility is given by metal crystalline structure and atomic packing. Adsorbing process is promoted at low temperature. Nevertheless, activation energy barrier for the adsorption requires high temperature, so the reaction can happen only in a suitable range of temperature.

2.1.2 Electrochemical adsorption

Corrosion phenomena on the metallic surface implies anodic oxidation of metal and cathodic reduction. In acidic solutions, without other oxidant agents, like oxygen, the reduction of hydrogen ion represents the most common cathodic reaction.

The most agreed mechanism regarding hydrogen evolution consists of:

1st) initial reduction step, which leads to the chemisorption of the hydrogen on the surface [12],[13]:

$$\mathbf{H^{+}\ (sol) + e^{-} \leftrightarrow H_{ads}\ (Me)}\quad (\textit{Volmer's reaction})$$

2nd a) chemical or electrochemical recombination of adsorbed hydrogen to molecular hydrogen:

$$\mathbf{H_{ads}\ (Me) + H^{+}\ (sol) + e^{-} \leftrightarrow H_2\ (gas)}\ (\textit{electrochemical or Heyrovsky's reaction})$$

$$\mathbf{H_{ads}\ (Me) + H_{ads}\ (Me) \leftrightarrow H_2\ (gas)}\ (\textit{chemical or Tafel's reaction})$$

Heyrovsky's reaction shows great variations with metal potential, while Tafel's reaction is kinetically influenced with low surface coverage and it has threshold reaction rate.

2nd b) adsorbed hydrogen may also penetrate into the metal:

$$\mathbf{H_{ads} \leftrightarrow H_{abs}}$$

Particular environmental aspects stabilize adsorbed hydrogen atoms, thus they promote their absorption into the metal lattice.

Figure 2.1 shows all the possible steps in the hydrogen reduction process [14], where the conditions of interest are usually the discharge step (*4*), the recombination passage (*5*), and desorption, or entry, step (*6*).

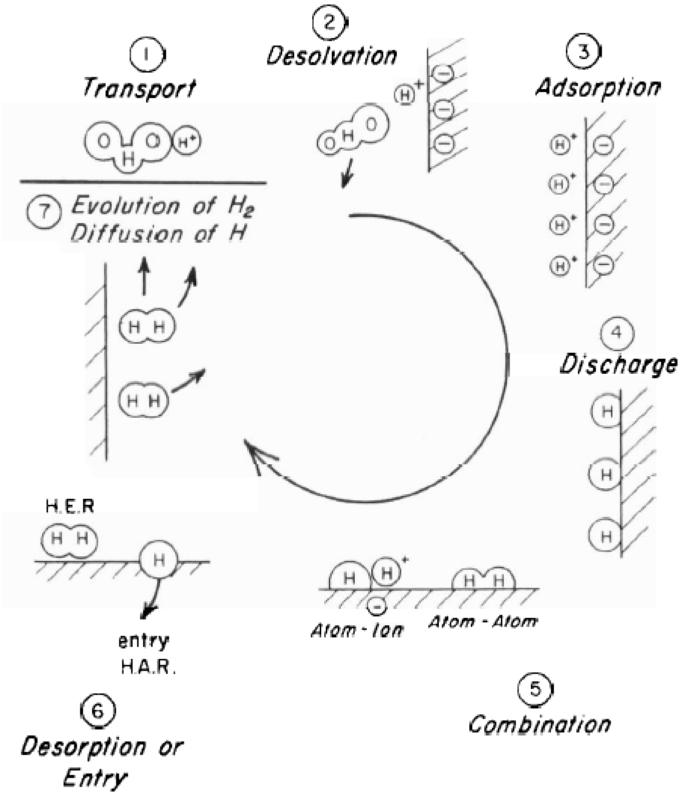

Figure 2.1 - Processes of hydrogen evolution and absorption [14].

McBreen and Genshaw [14] calculated the various rate expressions for the reaction paths.

2.2 Models of hydrogen entry

Two models for explaining hydrogen entry into the metal have been proposed.

The former, by Bockris and Thacker [14], considers that the hydrogen enters the same elementary form as it exists on the surface (atomic state).

In the latter model hydrogen enters directly from a discharged proton (hydrogen ion) and does not pass through the intermediate adsorbed phase. These models are schematically shown in Figure 2.2.

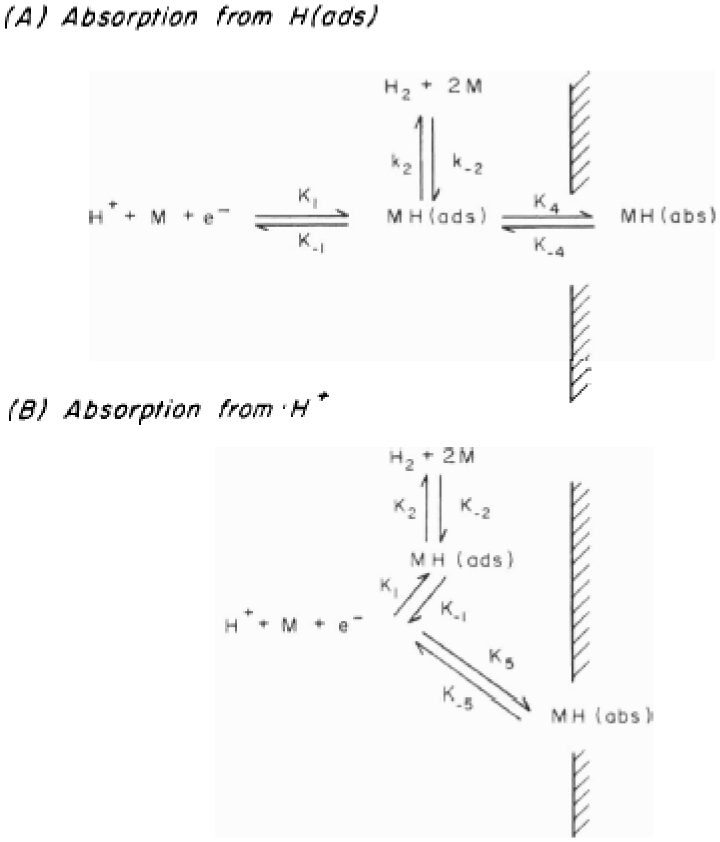

Figure 2.2 - Models for hydrogen entry into metals. (A) Absorption from atomic hydrogen, (B) absorption from protons [14].

In the Bockris-Thacker model the absorption step and chemical desorption (recombination) step are competing. In the second model, the hydrogen ion is discharged and passes immediately into the metal with no intermediate reactions involved, so the competing steps are absorption and electrochemical reduction.

Horiuti and Toya [14] have described two models (Figure 2.3) of hydrogen chemisorption that relate to the two models seen above. In the so-called r-type adsorption, similar to Bockris-Thacker model, the hydrogen adsorbed atoms are outside the electronic cloud but immediately atop a corresponding metal atom. The bonding is largely covalent with the hydrogen being the slightly negative member of the dipole. In the s-type absorption, similar to proton adsorption model, the hydrogen adatom is partly inside the electronic cloud of the metal. The hydrogen behaves more like a proton dissolved in the surface layer (within the electronic cloud of the metal) and the bonding is more ionic with positive charged hydrogen. This situation represents a higher energy state than r-type adsorption, but lattice defects and other surface imperfections significantly reduce the energy and promote s-type adsorption. From experimental measurements McCright [14], found that r-type adsorption dominates at low hydrogen coverages, s-type at high coverages.

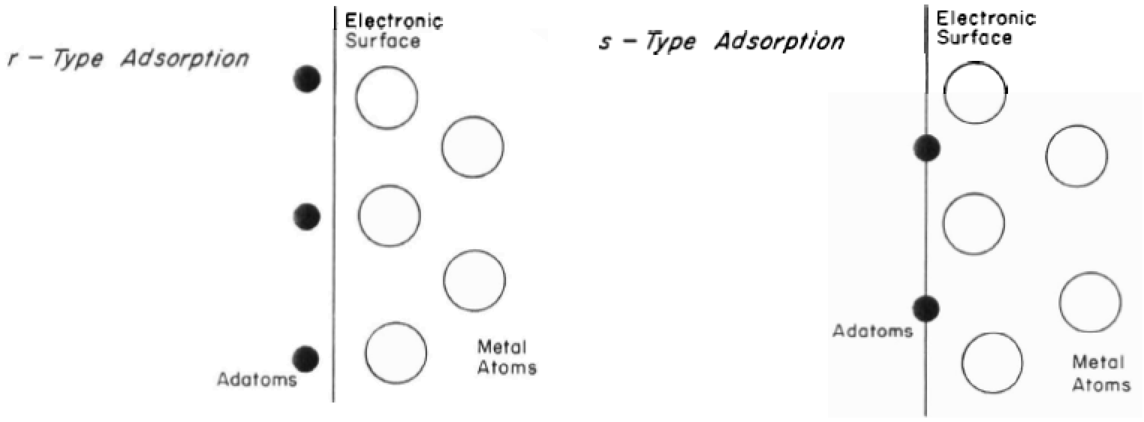

Figure 2.3 - Models for chemisorbed hydrogen.

2.3 Role of environmental variables

The rate of hydrogen absorption reaction strictly depends on the chemical potential of the adsorbed and absorbed phases, and in particular the concentration of adsorbed hydrogen.

From an experimental point of view the extent of the hydrogen absorption reaction is controlled by:

- the pH and composition of the solution
- the temperature
- the presence of certain species called "promoters" that catalytically favour hydrogen absorption
- the potential of the metal and hence the current density
- the presence of stress

Metallurgical variables will be considered in another chapter.

2.3.1 Effect of solution composition

At the corrosion potential the hydrogen entry kinetics increase with the solution acidity. In alkaline solutions a cathodic potential must be applied to affect hydrogen entry: indeed the corrosion potential in these solutions is above the reversible potential for hydrogen evolution. Moreover, when hydrogen adsorption rates from acid and alkaline solutions with the same current or applied overpotential are compared, the rate is much higher in the acid solution. In other words, the lower the pH is, the higher the entry rate will be.

When all other environmental conditions are the same, the anion sometimes alters the hydrogen absorption reaction. From the work of Hudson ([15], quoted in [14]), shown in Figure 2.4, the absorbed hydrogen in a low carbon steel is higher in H_2SO_4 solutions, followed by HCl, then H_3PO_4. You have to note that temperature plays an important role, increasing kinetics of absorption.

It is necessary also to consider the possibility that anions shift the potential in the noble direction, slowing down the hydrogen evolution and absorption reactions, as in the case of high concentrations of nitrate ion [15].

It is important to report that at moderately acid pH values the presence of acetate seems to improve the hydrogen entry kinetics. The permeation rate of hydrogen cathodically charged from a pH 4.5 acetate buffer is considerably higher than the one charged from a sulfate solution of comparable pH and ionic strength [16]. This last idea has been used in the experimental set up of the present thesis work and it is also reported in the NACE standard for SSCC testing [6].

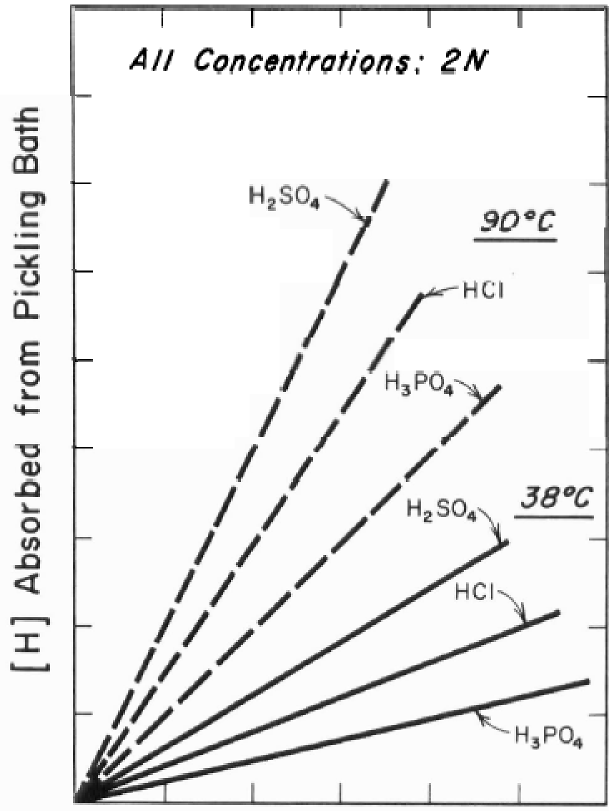

Figure 2.4 - Effect of anion on the hydrogen absorption in a low-carbon steel [14].

2.3.2 Role of hydrogen promoters

Many species have the capability of increasing the kinetics of the hydrogen entry into iron, steel and ferritic alloys. The significant feature is that some species can largely increase hydrogen entry kinetics even in very small quantities.

The names "cathodic poison" and "cathodic promoter" are applied to these species because they are said to poison the evolution reaction and therefore to promote hydrogen absorption.

Compounds and elemental form of Group V-A (phosphorus, arsenic, antimony, bismuth) and Group VI-A elements (sulfur, selenium, tellurium) are prominent among these species. Other species which increase the hydrogen permeation are halide ions in acid solution, cyanide ion in alkaline solutions, and the aromatic hydrocarbon naphthalene. Under specific circumstances salts of heavy metals such as mercury, tin, and lead have been reported as enhancing hydrogen entry.

Some properties of these species are:

- stable hydrides such as H_2S, H_2Te, H_2Se, PH_3, AsH_3;
- iodide, sulfide and cyanide ions strongly adsorb to metal surfaces;
- As, Sb, Hg, Bi, Pb and Sn have very low exchange current density for hydrogen evolution;
- cyanide, arsenic compounds, H_2S and PH_3 are extremely toxic to biological entities.

Newman and Shreir [17] proposed a relative effectiveness scale of the poisoners, irrespective of experimental conditions adopted:

S > P > Se > Te > As

which is in the order of their strengths and binding energies of the correspondent hydrides.

The two scientists also focused on the kind of compounds which can increase hydrogen entry, finding out the hydride phase is the responsible.

As the elongation is proportional to the amount of hydrogen absorbed, Smialowski et alii [14] measured the elongation of iron wires charged with hydrogen in the presence of promoters. They obtained the following intensive (elongation per atom H) effectiveness order:

S > P > AS > Se > Sb > Te > Bi

Kawashima, Hashimoto and Shimodaira [13] focused their attention on the way hydrogen sulfide acts as a promoter: it adsorbs on the steel increasing protons reduction since it forms intermediate products as follows:

$$\mathbf{H_2S_{ads} + e^- \rightarrow H_2S^-_{ads}}$$

$$\mathbf{H_2S^-_{ads} + H^+_{ads} \rightarrow H_2S{-}H_{ads}}$$

$$\mathbf{H_2S{-}H_{ads} \rightarrow H_2S_{ads} + H_{ads}}$$

H_2S modifies the usual way to obtain H_{ads} (Volmer's, Heyrovsky's or Tafel's reactions) catalyzing hydrogen reduction and originating intermediate specie Fe—H_2S—H^+.

2.3.2 Role of potential

The potential of a surface greatly influences the hydrogen evolution and absorption reactions and affects surface coverage.

From a thermodynamic point of view, the activity or fugacity of hydrogen on the solution side of the interface establishes H_{abs} concentration; however, Nernst equation should not be used for the calculation, because it concerns only thermodynamic equilibrium where oxidation and reduction rates are the same; differently, in the present situation kinetics of the reaction influences potentials (overpotentials).

Specifically, with the following reaction:

$$\mathbf{H^+ + e^- \rightarrow \frac{1}{2} H_2\ (gas)}$$

its equilibrium potential (E_{eq}), evaluated with Nernst equation, is:

$$E_{eq} = E_0 + \frac{RT}{zF} \ln \frac{a_{H^+}}{(f_{H_2})^{1/2}}$$

being:

E_{eq} = equilibrium potential of the reaction

E_0 = standard potential of the reaction (vs SHE), 298 K and unitary activity for liquid and solid species and 1 atm pressure for gaseous species

F = Faraday constant

R = universal gas constant

T = temperature

f_{H_2} = gaseous hydrogen fugacity

a_{H^+} = hydrogen ion activity

gaseous hydrogen fugacity at 1 atm, modified counting H^+ present in the solution, can be expressed with the following equation:

$$f_{H_2} = \exp(-2\eta \frac{F}{RT})$$

with:

η = electrode overpotential (negative quantity)

Looking at the two equations, taking into account reaction of paragraph 2.1.2 and constant electrolytic pH, it is possible to see that H_2 fugacity increases with overpotential.

Also an increase of the temperature leads to growth of fugacity, but this increase should be very high, out of hydrogen embrittlement susceptibility range of temperature (see the Paragraph 1.2).

3) MATHEMATICAL MODELS

3.1 Diffusion without traps

Diffusion of hydrogen atom in a ferritic (bcc) lattice occurs through interstitial sites with the octahedral sites being preferentially occupied at high temperatures and tetrahedral sites at low temperature [18], [19], [20]. In an ideal homogeneous single crystal, without any kind of defects, the depth of the potential wells and energy barriers between adjacent interstitial sites will be uniform and the flow and the distribution of hydrogen atoms in the material may be derived from the solution of Fick's first (stationary condition, Eq.1), and second law (not stationary condition, Eq.2) for monodimensionl flow:

$$j = -D\frac{\delta C}{\delta x} \tag{1}$$

$$\frac{\delta C}{\delta t} = D\frac{\delta^2 C}{\delta x^2} \tag{2}$$

j = flux of diffusible hydrogen;

D = diffusion coefficient of diffusible hydrogen;

C = concentration of diffusible hydrogen;

t = elapsed time.

The solutions of the Fick’s laws depend on the system geometry and on a set of boundary conditions. The geometrical model and the boundary conditions that simulate in the best way the Devanathan and Stachursky electrochemical method (see Chapter 5) for the measurement of the diffusion coefficient of hydrogen in metals are:

1. a membrane of finite thickness, x=L, and in-plane dimensions (y, z) much larger than L;
2. $C=C_0$ at x=0 and C=0 at x=L for any value of the time, t, i.e., the concentration of hydrogen atoms at the input side of a membrane is constant at all times (i.e. equilibrium between the surface coverage and sub-surface hydrogen atom

concentration is established instantaneously) and the concentration is zero at the output side.

Under the given boundary conditions it is possible to derive the flow of hydrogen at the exit side in function of the time in adimensional numerical form in two ways:

$$\frac{j}{j_\infty} = \frac{2}{\sqrt{(\pi\tau)}} \sum_{n=0}^{\infty} \exp\left\{ -\frac{(2n+1)^2}{4\tau} \right\} \tag{3}$$

$$\frac{j}{j_\infty} = 1 + 2\sum_{n=1}^{\infty} \left\{ (-1)^2 \exp(-n^2\pi^2\tau) \right\} \tag{4}$$

where j is the time dependent flux, j_∞ is the steady state value, τ is the dimensionless time parameter $\tau = Dt/L^2$ and L is the membrane thickness [21], [22]. Equation (3) for the normalized flux is the Laplace solution and equation (4) represents the Fourier solution. Both equations give equivalent results if enough steps in the summation are used [23]. ISO 17081 [21] suggest n =6 in order to have an accurate estimation.

As mentioned above, Eq 3 and Eq 4 are valid if the concentration of hydrogen on the entry side is constant; if the boundary condition on the input side is a constant flux then the normalized flux is given by [24]:

$$\frac{j(t)}{j_\infty} = 1 - \frac{4}{\pi} \sum_{n=0}^{\infty} \frac{(-1)^n}{(2n+1)} exp\left[-\frac{(2n+1)^2\pi^2\tau}{4} \right] \tag{5}$$

All these equations are very useful since they provide a mathematical model of the anodic flux in a Devanathan and Stachurski cell as a function of time. This relation is used to explain permeation curves, as the example in Figure 3.1:

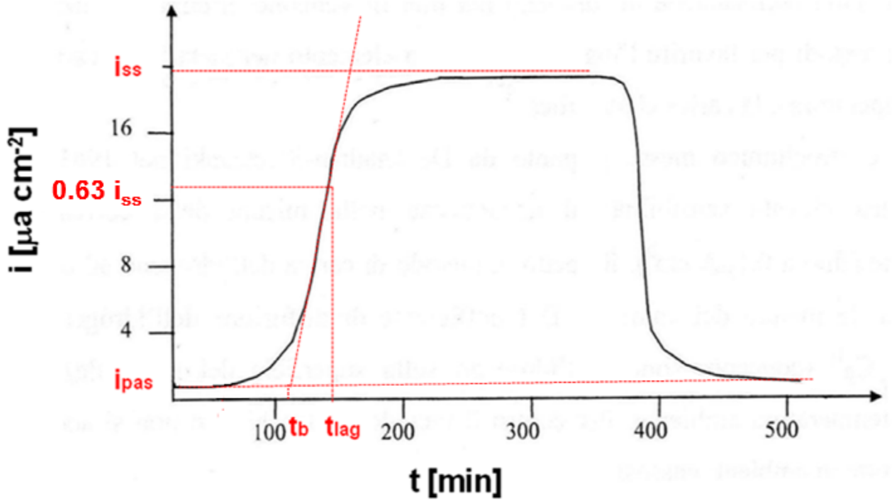

Figure 3.1 - Permeation curve of hydrogen.

In particular, a typical curve uses hydrogen oxidation current density *i* on the anode as a measure of the flux.

3.2 Calculation of diffusion coefficient

Once permeation curve as the one shown in Figure 3.1 is available, the diffusion coefficient can be calculated by using a variety of methods [21], [25]. Among the most widespread, there are:

- **The time lag** represents the specific time with a corresponding current of 0.6299 of stationary current i_{SS}:

$$t_{lag} = \frac{L^2}{6D}$$

- **The breakthrough time** represents the elapsed time extrapolating the curve with the linear portion of the rising permeation curve:

$$t_b = \frac{L^2}{15.3D}$$

Starting from these specific values, it is possible to generalize the formula as follows:

$$t = \frac{L^2}{MD}$$

Where M is a constant depending on the time t that corresponds to different values of the ratio j/j_∞.

If you determine D it is possible to calculate, for a given steady state permeation rate, the subsurface hydrogen concentration in the membrane at the entry side, e.g. quoted in [59]:

$$C_0\ (ppm) = \frac{i_\infty L}{FD} \times \frac{M_H}{\rho_{Fe}} 10^6 \tag{6}$$

Where:

i_∞ = steady state current density;

F = Faraday constant;

M_H = atomic weight of H;

ρ_{Fe} = density of iron.

3.3 Diffusion with trapping

In real materials the depth of the potential wells and the height of the energy barriers are not uniform throughout the lattice because of the existence of grain boundaries, carbide particles, inclusions, dislocations and other sites that can act as traps for hydrogen atoms due to the depth of their potential wells. Traps essentially act as sinks for hydrogen atoms during hydrogen charging of a material. Fick's second law for pure diffusion is no longer valid and a more comprehensive treatment is required.

Some models have been developed, e.g. [28] and [29], considering both diffusion and trapping. This last aspect has been treated as a reaction of specific sites with hydrogen flowing across the material. In these models traps can be reversible or irreversible, saturable or not saturable (see Chapter 4), moreover each kind of trap can have a different reaction rate constant and activation energy.

A very comprehensive treatment would embrace a complete description of all types of traps requiring a definition of the different types of sites, the number of sites per unit volume and the average time of transfer among sites for each type of site. The most comprehensive approach to this problem was developed by Leblond and Dubois [26], [27] based on a statistical approach diffusion, but the generalized equation contains too many unknown parameters for practical application. A more tractable set of equations can be obtained making some assumptions:

- the probability of capture is the same of each kind of site
- a metal contains three kinds of site: diffusion sites, reversible traps and irreversible saturable traps.
- every trap site is surrounded by normal diffusion sites (no direct path between trap sites)

These assumptions can lead to equations not analytically solvable, but numerical treatment was being pursued; a deeper analysis should go beyond this thesis purposes.

Solution of a reduced set of equations have been proposed by McNabb and Foster [28] who considered only reversible traps, by Iino [31] who considered both reversible and irreversible traps but only of one kind (only one reaction rate constant) and by Oriani [29]. In order to clarify the meaning of the terms “lattice diffusion coefficient” and “apparent diffusion coefficient”, that are very important in the interpretation of the experimental results of the present thesis, an overview of Oriani's model is exposed in the following paragraph. Hereafter the term "apparent diffusion coefficient", D_{app}, will be used rather than "effective diffusion coefficient", D_{eff} , when it is possible.

3.3.1 Oriani's model of hydrogen permeation

Oriani [29] defines two kinds of existing sites (Figure 3.2): the vast majority of sites are the ordinary or normal (interstitial) sites characterized by normal enthalpy of solution with respect to an atmosphere of gaseous hydrogen. The minor fraction of the sites is called extraordinary or trapping sites, and it provides an energetically favored environment for occupancy by the hydrogen.

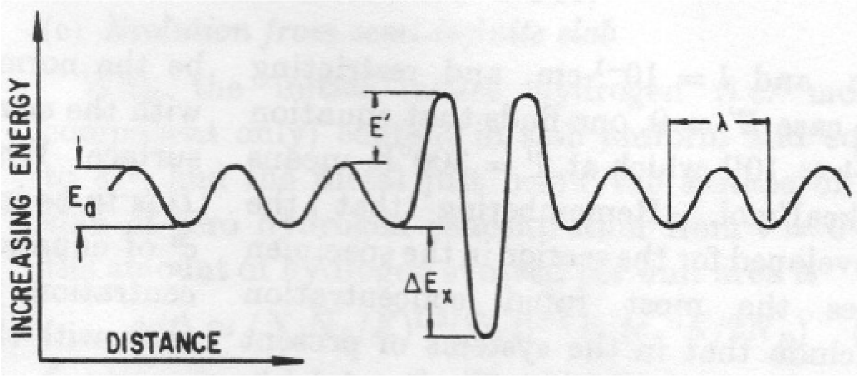

Figure 3.2 - Model for trapping site [29].

Due to the small ratio of extraordinary to the normal sites, we can assume that traps population doesn't appreciably reduce the cross-section for diffusion in the normal lattice.

$$J = -D_L \frac{dc_L}{dx} \tag{7}$$

where:

c_L = hydrogen concentration upon normal lattice sites

D_L = homogeneous lattice diffusivity

If we consider also the presence of extraordinary sites:

$$J = -D_{app} \frac{dc}{dx} \tag{8}$$

where:

c = hydrogen concentration upon normal lattice sites plus trapping sites (c_T)

D_{app} = apparent diffusivity

A fundamental assumption of Oriani is local equilibrium between the hydrogen in lattice sites and the hydrogen in trapping sites. This assumption means that the chemical potentials must be equal: $\mu_L = \mu_T$. In Oriani's model no consideration on the kinetics of hydrogen reaction with trapping sites is made so it is valid only for equilibrium conditions.

The equilibrium between the two atomic populations can be described by the equilibrium constant $K = a_T/a_L$, where a_T and a_L are the activities of the hydrogen upon the trapping and the normal sites, respectively.

Assuming no interaction between occupied sites, each of the two activities can be expressed in terms of fraction of the available sites (θ_i) : $a_i = \theta_i/(1 - \theta_i)$, which becomes $a_i = \theta_i$ if $\theta_i \rightarrow 0$. Furthermore, since we are considering very low percentage of occupied normal sites due to huge number of sites, $\theta_L << 1$, the equilibrium constant can be expressed as:

$$K = \frac{1}{\theta_L}\left(\frac{\theta_T}{1-\theta_T}\right) \tag{9}$$

Remembering that $c = c_L + c_T$ and using the equations shown, apparent diffusion coefficient can be correlated to lattice diffusion:

$$D_{app} = D_L \frac{dc_L}{dc} = \frac{D_L c_L}{c_L + c_T(1-\theta_T)} \tag{10}$$

Defining N_T and N_L as the number of trapping and lattice sites per unit volume, $c_i = N_i \theta_i$, it is possible to modify Eq 10 in order to have apparent diffusivity independent of the hydrogen concentration:

$$D_{app} = \frac{D_L}{1+KN_T/N_L} \tag{11}$$

Eq. 11 gives the possibility to easily understand how modification of one of its parameter alters the D_{app} value. For example an increase of lattice sites makes D_{app} greater, while more trapping sites or a higher equilibrium constant decrease it. However, D_{app} value is always smaller than D_L value.

3.4 Desorption Analysis

When the cathodic current is interrupted, the decay transient starts. Nanis and Namboodhiri [30] analyzed this part of permeation test. They understood that decay transient is a source of additional information regarding the diffusivity and solubility of hydrogen in the membrane. In particular, the time integral of flux at the exit side reflects the total amount of hydrogen extracted at this side. They considered two limiting current drop decay transient, the fastest and the slowest extraction. The slowest extraction is developed assuming that the entry side become impermeable to hydrogen after current interruption, which is not the case of our experimental apparatus.

The fastest extraction, with the proper initial condition to Fick's second law:

$$C = C_0\left(1 - \frac{x}{L}\right) \tag{12}$$

and the assumption that the concentration at the input side is assumed to drop instantaneously to zero upon input current interruption, gives the following solution:

$$1 - 2\sum_{n=0}^{\infty} \pi^{-\frac{1}{2}} \tau^{-\frac{1}{2}} \exp\left[\frac{(-2n+1)^2}{4\tau}\right] \tag{13}$$

The Eq. 13 is equal to *1 - Eq. 3*. This model predicts what may happen in the anodic part in the ideal diffusion of hydrogen, i.e. lattice diffusion, no traps. In the real case the decay transient is affected by trapping phenomena (reversible traps, see Chapter 4), which modify the shape of the curve.

Zakroczymski [59] slightly modified Eq. 13 in order to use it in his partial build-up and partial decay permeation curves (see paragraph 5.3). He performed the rising transient and the decay starting from a steady-state current density (after a long permeation), so the build-up and decay equations, in terms of current density, become:

Build-up:

$$\frac{i_\mathrm{p} - i_\mathrm{p}^0}{i_\mathrm{p}^\infty - i_\mathrm{p}^0} = \frac{2L}{\sqrt{\pi D t}} \sum_{n=0}^{\infty} \exp\left(-\frac{(2n+1)^2 L^2}{4Dt}\right) \qquad (14)$$

Decay:

$$\frac{i_\mathrm{p} - i_\mathrm{p}^\infty}{i_\mathrm{p}^0 - i_\mathrm{p}^\infty} = 1 - \frac{2L}{\sqrt{\pi D t}} \sum_{n=0}^{\infty} \exp\left(-\frac{(2n+1)^2 L^2}{4Dt}\right) \qquad (15)$$

where i_p is the measured rate at time t, i_p^0 the initial steady-state permeation rate (t=0), i_p^∞ is the new steady-state permeation rate (t go to ∞). Later in the thesis (Chapter 5) the reasons to make this kind of permeation, and its effect on the hydrogen diffusion, will be explained.

4) MICROSTRUCTURAL EFFECTS ON DIFFUSION AND TRAPPING

4.1 Traps definitions and classifications

Oriani in [34] defined traps as any structural imperfection or impurity atom with which dissolved hydrogen interacts attractively causing the hydrogen atom to spend more time in its vicinity than at a normal lattice site, chiefly because the activation energy for escape from a tight-binding site will be increased approximately by the binding energy.

It is impossible to find a univocally accepted way to classify different traps. A list of the most relevant classifications is reported below.

As a first attempt to organize traps in different classes, Pressourye's definition [32], [33] may be employed: a reversible trap is one at which hydrogen has a short residence time at the temperature of interest with an equivalent low interaction energy. On the other hand, for the same conditions, an irreversible trap is one with a negligible probabilities of releasing hydrogen. Reversible traps include grain boundaries, dislocations and microvoids [40]. Irreversible traps include non-metallic inclusion (e.g. Al_2O_3 complex(Fe,Mn)S or double oxide $FeO.Al_2O_3$ inclusions and Si-ferritic carbide [40]) and precipitates (e.g. precipitates of Ti(C,N), Nb and V such as TiC, TiN, $Ti_4C_2S_2$ and VC [40], [41], [47]).

A further classification of the different trap sites based on the binding energy of the trap with hydrogen in a body centered cubic α-Fe lattice shows three main categories of traps [35]:

- very weak traps (binding energy ≈ 20 kJ/mol): dislocations and fine precipitates in the matrix;
- intermediate traps (binding energy ≈ 50 kJ/mol): martensite laths and prior austenite grain boundaries;
- strong traps (binding energy ≈ 100 - 120 kJ/mol): non metallic inclusions, spherical precipitates, interfaces or martensite laths and/or prior austenite grain boundaries with retained austenite, fine precipitates or impurity segregation; hydrogen trapped in these sites is released only at high temperatures.

Frappart et alii [36], in a martensitic steel, listed four different scales of potential trap sites (Figure 4.1):

- the macroscopic scale (prior austenite grains, grain boundaries);
- the lath scale (interface density, lath size);
- the precipitates scale (precipitate density, coherent/incoherent precipitate, strain field);
- the dislocations scale (dislocation density, hydrostatic pressure).

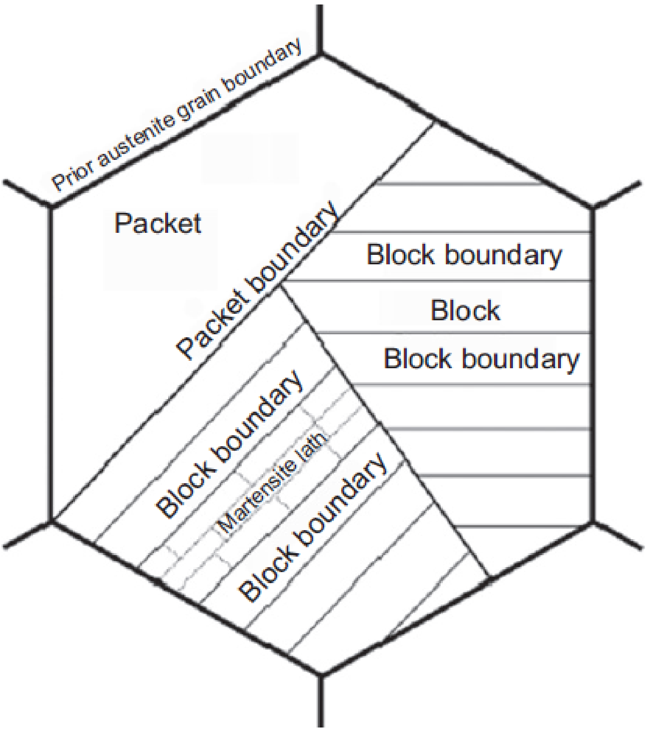

Figure 4.1 - Microstructural characterization of martensitic steel [36].

Figure 4.2 illustrates the trapping energy for each of these trapping sites, ΔE_{TL}, found in literature [36], expressed in eV. The relation between ΔE_{TL} and ΔE_L, the activation energy for moving from a lattice site an adjacent one, is schematically shown in Figure 4.3.

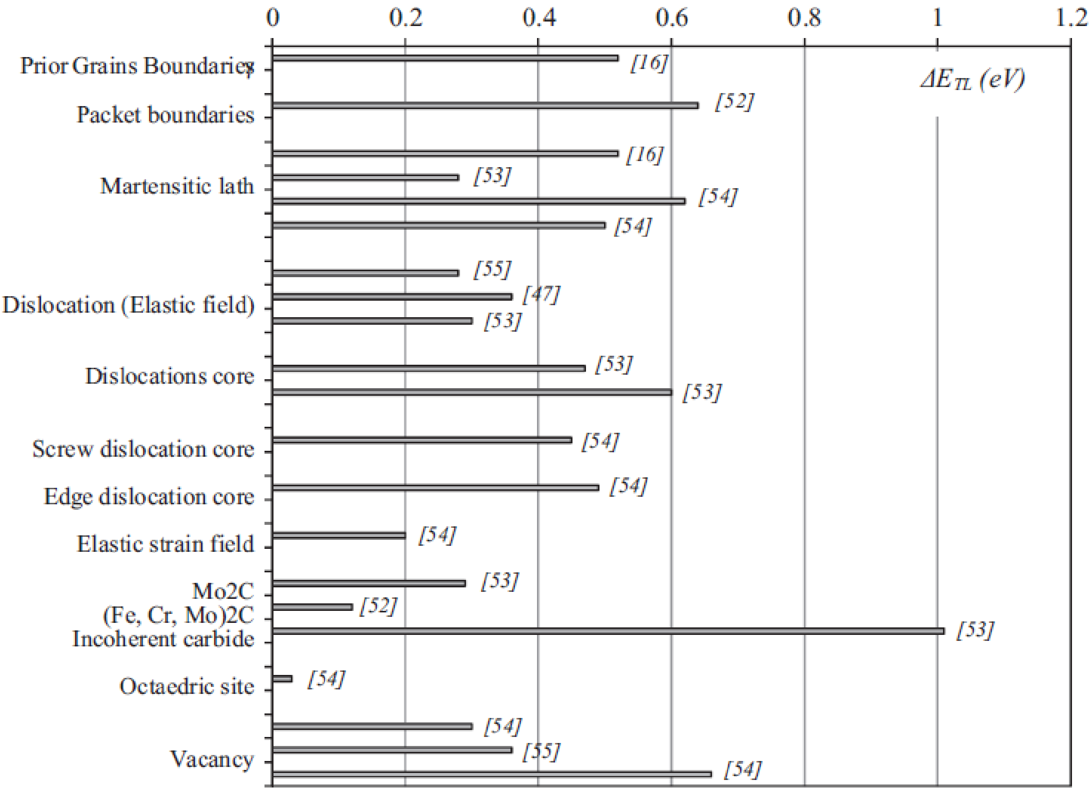

Figure 4.2 - Trap binding energy for a martensitic microstructure [36].

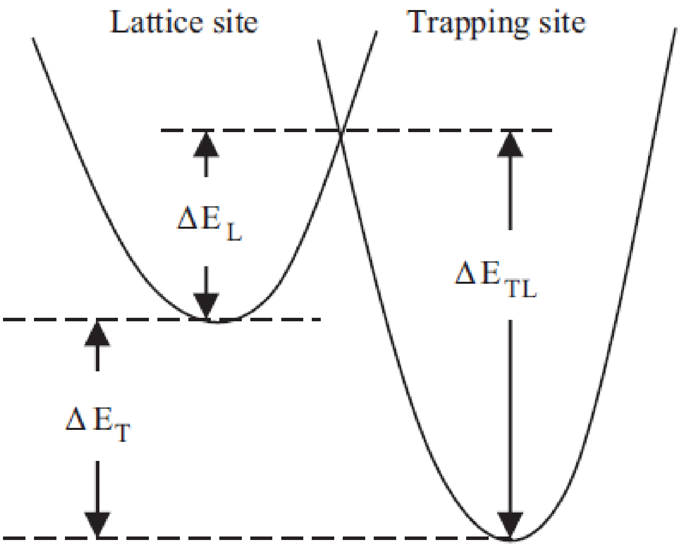

Figure 4.3 - Schematic view of energy relations in hydrogen-metal system [36].

A distinction between saturable and nonsaturable traps has also been made [20]:

- in a saturable trap it is possible to accommodate only a finite number of atoms, due to its physical nature (e.g. grain boundaries and dislocations);

- in a nonsaturable trap it is possible to accommodate infinite number of atoms (e.g. voids).

According to Krom and Bakker [20], the two main trapping effects are to increase the apparent hydrogen solubility and to decrease the apparent diffusivity. The authors justified these two trends explaining that when steel is in physico-chemical equilibrium respect to a fixed external chemical potential of hydrogen, it will absorb hydrogen to the solubility limit of the lattice, while a further quantity of hydrogen will occupy the traps. Equilibrium is established when the chemical potential of the hydrogen distribution in lattice and trap side and the external chemical potential become equal. Thus, the apparent solubility (total hydrogen concentration) may be significantly higher than the lattice solubility. A trapped hydrogen atom must acquire a substantially larger energy than the lattice migration energy to escape the trap. Consequently, in the presence of trapping, the apparent diffusivity will be lower than the lattice diffusivity.

4.2 Microstructures and hydrogen diffusion

In this paragraph, the influence of different microstructures on hydrogen diffusion is evaluated with literature review. At the beginning, the most interesting results are listed by authors and explained, at the end the most relevant paper results are summarized in a table reported in ANNEX.

These results come from the permeation techniques explained in Chapter 5, which is strongly correlated to the present one because the former is necessary to understand the latter and vice versa. In particular, see Devanathan and Stachurski's permeation method in order to properly understand these results. Nevertheless, the main parameters related to permeation phenomenon are briefly recalled below.

4.2.1 Luu and Wu

Luu and Wu [37] carried out electrochemical permeation measurements on annealed mild steel (C=0.05%) and on a S45C medium carbon steel (C=0.45%) in four microstructures in order to improve the knowledge of hydrogen transport in steels presenting different composition and microstructure.

After an initial charging run, in the second permeation transient they measured three parameters, i.e. the permeation rate, defined by:

$$J_\infty = \frac{i_p^\infty L}{nF}$$

diffusion:

$$D_{eff} = \frac{L^2}{6t_L}$$

and hydrogen concentration:

$$C_{app} = \frac{J_\infty L}{D_{app}}$$

where i_p^∞ is the steady-state permeation current density, n is the number of electrons transferred, F is the Faraday's constant, L is the specimen thickness, J_∞ is the steady-state flux, t_L is the time lag, D_{app} is the apparent diffusion coefficient and C_{app} is the apparent solubility.

Their results are reported in Table 4.1.

Table 4.1 - Permeation rate, diffusivity and solubility for the sample with constant charging current of 10 mA cm^{-2} [37].

Alloy	**$J_\infty L_{app}$ (mol H m^{-1} s^{-1})**	**D_{app} (m^2/s)**	**C_{app} (mol H m^{-3})**
Annealed mild steel	4.67×10^{-10}	1.05×10^{-9}	0.44
Annealed S45C	3.49×10^{-10}	2.96×10^{-10}	1.18
Normalized S45C	3.58×10^{-10}	2.78×10^{-10}	1.29
Spheroidized S45C	3.93×10^{-10}	3.50×10^{-10}	1.13
Quenched S45C	1.82×10^{-10}	3.70×10^{-11}	4.92

In the same heat treatment condition, the D coefficient is greater in mild steel than in S45C. For the other microstructure of 0.45 C steel, D values slightly decrease from spheroidized to normalized and annealed sample (almost equals), while the quenched sample is one order of magnitude lower. The apparent hydrogen concentration is maximum in martensitic microstructure, it is about three time lower in spheroidized, in normalized and in annealed S45C and it is minimum in annealed mild steel.

The decrease in permeation rate and effective diffusivity in the steel with higher carbon content is explained in terms of Fe_3C acting as an obstacle to steady-state and unsteady-state transport. Moreover the effective diffusivity decreases as the carbide distribution becomes more finely divided. The lowest permeation rate and diffusivity for medium carbon martensitic structure are due to the amount of induced imperfections in supersaturated bct structure after quenching, which delay the hydrogen diffusion and act as obstacles to the hydrogen flux.

These authors used hydrogen microprint technique to study hydrogen distribution in the material microstructure and possible diffusion paths. These results suggest that the main diffusion paths of hydrogen are grains, carbide-ferrite interfaces in pearlitic and spheroidized steels, and lath interfaces in martensitic steel. Accelerated diffusion along grain boundaries was not observed in carbon steel. This last aspect justifies the mathematical assumption not to consider direct paths among extraordinary sites.

Hydrogen trapping sites are carbide-ferrite interfaces in pearlitic and spheroidized steels, and a lath interfaces and dislocations in martensitic steel.

4.2.2 Park et al.

Park et alii [39] focused their efforts to understand the effect of microstructure on hydrogen diffusion in common linepipe steel equivalent to API 5L X65 grade [62]. In order to achieve this goal, they performed four different thermo-mechanical treatments on a microalloyed C-Mn steel (C=0.05%) as shown in Figure 4.4, they characterized the microstructure and evaluated hydrogen diffusion behaviour by the electrochemical method.

These authors make some relevant remarks regarding the efforts and the experimental cautions required to obtain reliable and reproducible results.

The results are listed in Table 4.2.

Table 4.2 - Hydrogen permeation data [39].

Specimen	Microstructure	M/A fraction	$J_{ss}L$ (mol H m^{-1} s^{-1})	D_{app} (m^2 s^{-1})
A1	F/DP	1.28	$1.33\text{x}10^{-8}$	$9.27\text{x}10^{-10}$
A2	F/AF	5.73	$8.47\text{x}10^{-9}$	$4.05\text{x}10^{-10}$
A3	F/DP	0.88	$1.29\text{x}10^{-8}$	$9.38\text{x}10^{-10}$
A4	F/B	4.45	$1.20\text{x}10^{-8}$	$4.44\text{x}10^{-10}$

F, ferrite; DP, degenerated pearlite; AF, acicular ferrite; B, bainite; M/A, martensitic/austenitic.

The D values (presumably evaluated in first permeation tests, the most influenced by trapping phenomenon) show F/DP values almost equal to 10^{-9}. F/AF and F/B diffusion coefficient values are about half of the F/DP ones. $J_{SS}L$ values are very far from Luu and Wu values.

The authors commented the results ascribing all the difference among different microstructures to trapping, i.e. the lower the values of D_{app} and $J_{ss}L$ are, the more the hydrogen trapping occurs. Then, on the basis of their results, they state that acicular ferrite and bainite act as reversible trapping sites, with trapping efficiency increasing in the order: degenerate pearlite, bainite and acicular ferrite.

In their paper they also reported cathodic potential evolution during time (Figure 4.5), which decreases sharply at the beginning (about 20 minutes), but then it seems to stabilized to -690 mV vs. SHE. However the potential change varies about 20 mV.

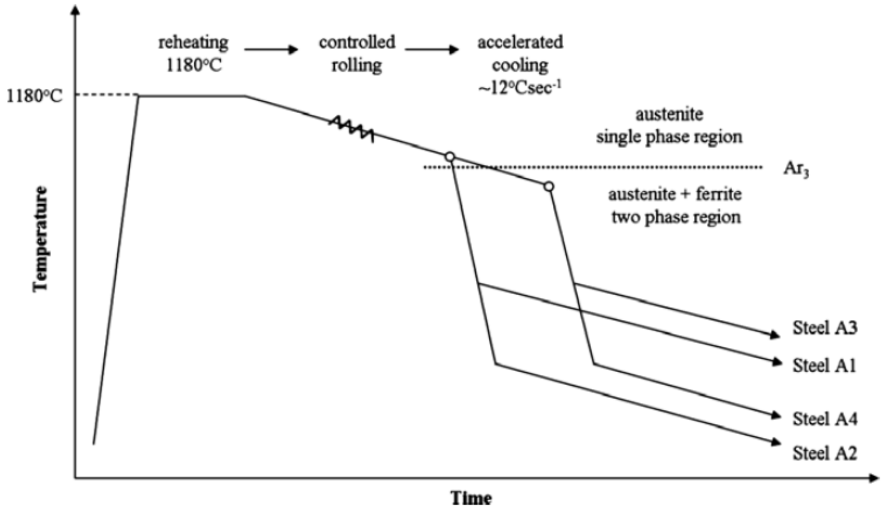

Figure 4.4 - A schematic graph of heat treatments performed on samples [39].

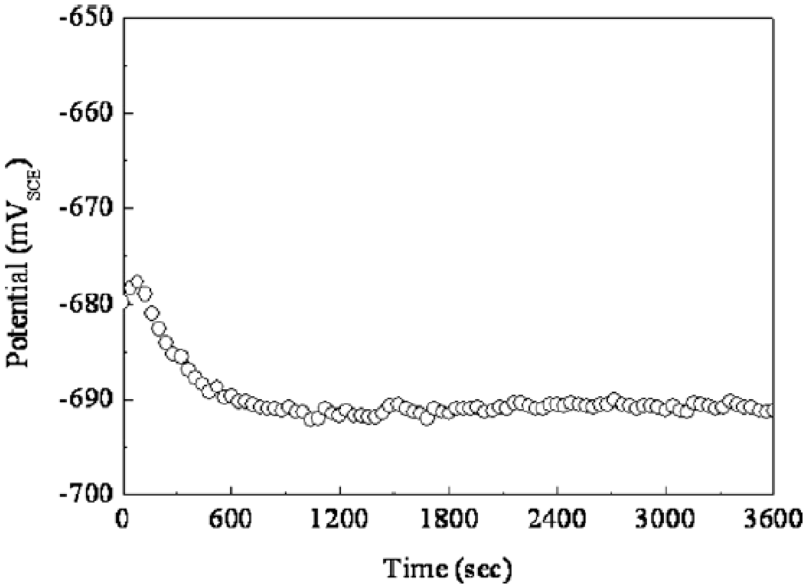

Figure 4.5 - Change in potential of the cathodic cell with time during the permeation test [39].

4.2.3 Réquiz et al.

Réquiz et alii [38] studied the effect of plastic deformation (not reported here) and heat treatments on hydrogen permeation of common carbon steel pipe, API 5L X52, 1 mm thickness. The results of permeation techniques, D_{app}, are shown in Table 4.3.

The D values found are very low compared to the previous works, with maximum values for as received and quenched microstructures (very similar) a minimum result for the normalized sample and a middle value, near to minimum, for annealed. This table also reports the dislocation density analysis result made by TEM because the authors associated the permeation density values with this dislocation parameter and thanks to it hydrogen diffusion is favoured in quenched material array dislocations.

This result shows a reverse trend compared to other works and they gave an odd justification of it. Indeed all the D_{app} measured are in the same order of magnitude (maximum- minimum ratio of about three), a very low difference if we consider the intrinsic low reproducibility of measurement method.

Table 4.3 - Dislocation density and apparent diffusion coefficient (time lag) [38].

Condition	**Dislocation density**	**D_{lag} (m^2/s)**
As received	$7x10^8$	$3.02x10^{-11}$
Normalized	$6x10^8$	$9.84x10^{-11}$
Annealed	$3x10^8$	$8.96x10^{-11}$
Quenched	$2x10^{11}$	$3.76x10^{-11}$

4.2.4 Haq et al.

Haq et al. [40] investigated the effect of microstructure and composition on hydrogen permeation in pipeline steels. They made an interesting summarizing work of several previous experimental researches done on pipeline steels (API 5L from X52 to X100), which is reported in Table 4.4. Some comments can be done on it: there is not any correlation between the steel grades and permeation parameters. Moreover D values varies in a three orders of magnitude range for steels with very similar composition (they are all C-Mn microalloyed steels).

Table 4.4 - Summary of permeation parameters for pipeline steel in literature [40].

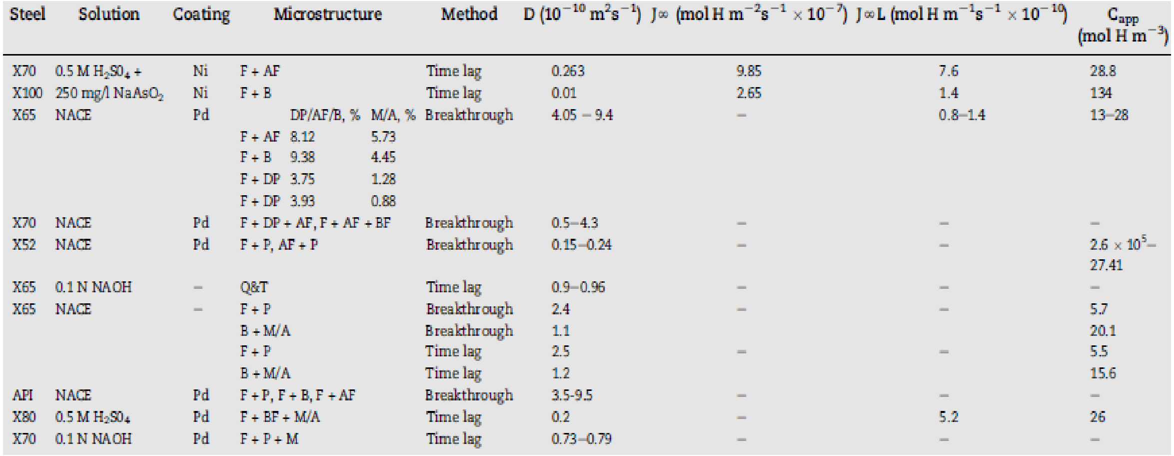

Steel	Solution	Coating	Microstructure	Method	D (10^{-10} m^2s^{-1})	J∞ (mol H $m^{-2}s^{-1} \times 10^{-7}$)	J∞L (mol H $m^{-1}s^{-1} \times 10^{-10}$)	C_{app} (mol H m^{-3})
X70	0.5 M H_2S0_4 +	Ni	F + AF	Time lag	0.263	9.85	7.6	28.8
X100	250 mg/l $NaAsO_2$	Ni	F + B	Time lag	0.01	2.65	1.4	134
X65	NACE	Pd	DP/AF/B, % M/A, %	Breakthrough	4.05 – 9.4	–	0.8–1.4	13–28
			F + AF 8.12 5.73					
			F + B 9.38 4.45					
			F + DP 3.75 1.28					
			F + DP 3.93 0.88					
X70	NACE	Pd	F + DP + AF, F + AF + BF	Breakthrough	0.5–4.3	–	–	–
X52	NACE	Pd	F + P, AF + P	Breakthrough	0.15–0.24	–	–	2.6×10^5– 27.41
X65	0.1 N NAOH	–	Q&T	Time lag	0.9–0.96	–	–	–
X65	NACE	–	F + P	Breakthrough	2.4	–	–	5.7
			B + M/A	Breakthrough	1.1			20.1
			F + P	Time lag	2.5	–	–	5.5
			B + M/A	Time lag	1.2			15.6
API	NACE	Pd	F + P, F + B, F + AF	Breakthrough	3.5-9.5	–	–	–
X80	0.5 M H_2S0_4	Pd	F + BF + M/A	Time lag	0.2	–	5.2	26
X70	0.1 N NAOH	Pd	F + P + M	Time lag	0.73–0.79	–	–	–

In the experimental part of [40], they worked on X70 pipeline steels, performing microstructural characterization and electrochemical technique (first and second transient). In particular, they prepared X70 samples with different Mn content (standard X70, Mn=1.14%wt and MX70 grade, Mn=0.5%wt) and from different regions of the original steel bar (edge and centerline). Some samples are obtained from transfer bar, others from hot rolled strip. Their results are shown in Table 4.5.

Table 4.5 - Microstructural and permeation results [40].

Specimen	**Microstructure**	**Average hardness**	**$J_{SS}L$ (mol H m^{-1} s^{-1} x 10^{-10})**	**D_{lag} (10^{-10} m^2/s) First**	**D_{lag} (10^{-10} m^2/s) Second**	**C_{app} (mol H m^{-3})**
X70 Edge	F + P	198 ± 7	1.66 ± 0.25	1.97 ± 0.09	1.77 ± 0.06	0.84
X70 Centreline	F (more uniform , bigger grains than Edge) + P	187 ± 8	1.65 ± 0.23	2.25 ± 0.19	2.06 ± 0.17	0.74
MX70 Edge	F + P	187 ± 6	1.95 ± 0.25	1.70 ± 0.04	1.57 ± 0.03	1.2
MX70 Centreline	F (more uniform , bigger grains than Edge) + P	186 ± 3	1.55 ± 0.35	1.71 ± 0.04	1.52 ± 0.03	0.90
X70 TB Edge	F + B	170 ± 6	1.67 ± 0.16	2.10 ± 0.19	1.33 ± 0.31	0.80
X70 TB Centreline	F + Granular B	189 ± 3	2.34 ± 0.20	3.05 ± 0.17	2.15 ± 0.30	0.77
X70 Normalized TB	F + P	142 ± 9	2.42 ± 0.03	4.01 ± 0.02	3.82 ± 0.13	0.60

F, ferrite; P, pearlite; AF, acicular ferrite; B, bainite;

They concluded that the high or low values of diffusivity are strictly related to the effect of fineness, precipitates and dislocation density, that is to say for example, the medium strip showed the lowest diffusivities due to the combined effect of a fine grain size and a high density of (Ti,Nb)C,N precipitates. On the contrary the normalized bar showed the highest diffusivity due to its large ferrite grains and a very low dislocation density. However, as in the case of Réquiz [38] described above, the different diffusivity has very similar values, which do not represent the real big microstructural variation properly.

The authors observed that the first transient current, after it had reached its maximum, it continuously decreased. Moreover the second transient didn't reach the same permeation current as the first steady state values (Figure 4.6). They ascribed this behaviour to the absence of Pd coating on the anodic side which allows the formation of an oxide layer, provoking a barrier effect, as Manolatos found [42].

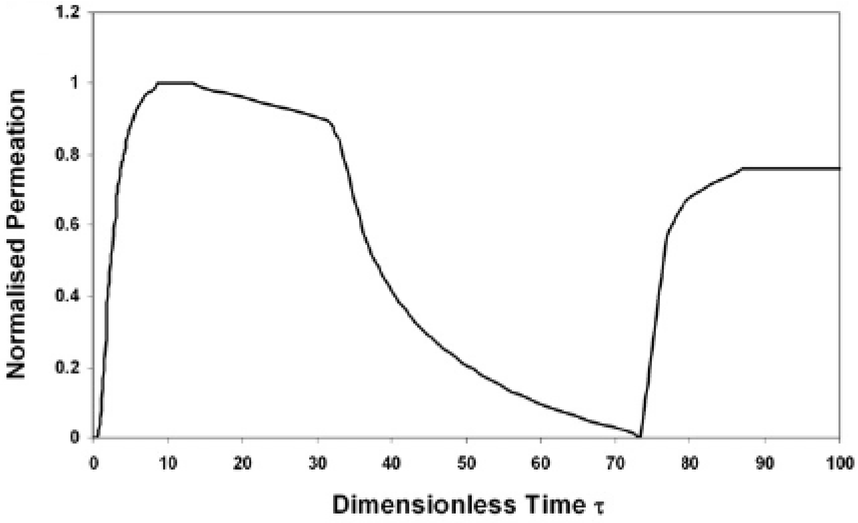

Figure 4.6 - First and second polarization transient [40].

4.2.5 Norena and Bruzzoni

Norena and Bruzzoni [49] performed hydrogen permeation tests (four temperatures for each kind of sample) on P91 steel with five different microstructures. P91 steel is a modified 9 Cr–1 Mo steel which contains Nb and V as microalloying elements. Samples of this steel were heat treated as shown in Table 4.6.

Table 4.6 - Thermal treatments performed on the P91 steel [49].

Designation	**Description**	**Expected micfrostructure**
AR (as received)	Austenized at 1040 °C, air cooling, tempered at 780 °C	Tempered martensite
AC (air cooled)	AR + austenitizing at 1050 °C, air cooling	As quenched martensite
T300	AC + tempered at 300 °C 1h	Tempered martensite
T500	AC + tempered at 500 °C 1h	Tempered martensite
FC (furnace cooled)	AR + annealed at 970 °C 40 min + annealed at 775 °C 4 h + furnace cooled	Ferrite + carbides

Gas phase charging and electrochemical detection were used, the following table summarizes the results. The diffusion coefficient has been estimated with characteristic tangent time t_{tan} and lag time t_{lag} for both build up and decay transient. The Authors state that: “..for a given metallurgical condition and temperature, the values of the diffusion coefficient depend on the method of determination. The lowest value is always the one obtained from the tangent time of the permeation rising transient. The highest value is that from the tangent time of the decay transient”. The ratio between these two values ranges between 1.14 to 5.4 (mean value 3.4).

Table 4.7 - Apparent hydrogen diffusion coefficient [10^{-8} cm^2 s^{-1}] of the P91 steel subjected to gas phase charging (p = 1 bar) [49].

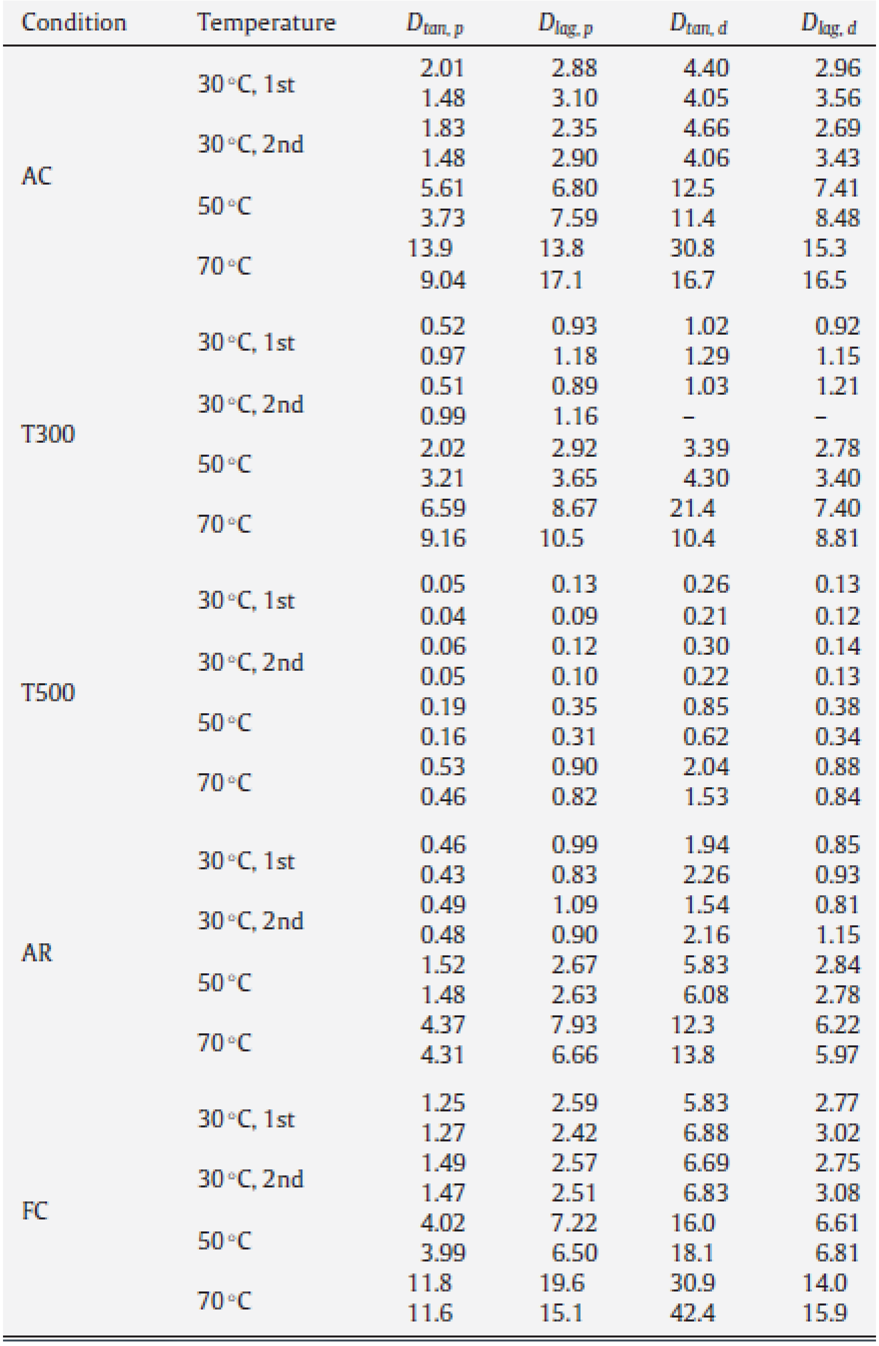

Condition	Temperature	$D_{tan,p}$	$D_{lag,p}$	$D_{tan,d}$	$D_{lag,d}$
AC	30 °C, 1st	2.01	2.88	4.40	2.96
		1.48	3.10	4.05	3.56
	30 °C, 2nd	1.83	2.35	4.66	2.69
		1.48	2.90	4.06	3.43
	50 °C	5.61	6.80	12.5	7.41
		3.73	7.59	11.4	8.48
	70 °C	13.9	13.8	30.8	15.3
		9.04	17.1	16.7	16.5
T300	30 °C, 1st	0.52	0.93	1.02	0.92
		0.97	1.18	1.29	1.15
	30 °C, 2nd	0.51	0.89	1.03	1.21
		0.99	1.16	–	–
	50 °C	2.02	2.92	3.39	2.78
		3.21	3.65	4.30	3.40
	70 °C	6.59	8.67	21.4	7.40
		9.16	10.5	10.4	8.81
T500	30 °C, 1st	0.05	0.13	0.26	0.13
		0.04	0.09	0.21	0.12
	30 °C, 2nd	0.06	0.12	0.30	0.14
		0.05	0.10	0.22	0.13
	50 °C	0.19	0.35	0.85	0.38
		0.16	0.31	0.62	0.34
	70 °C	0.53	0.90	2.04	0.88
		0.46	0.82	1.53	0.84
AR	30 °C, 1st	0.46	0.99	1.94	0.85
		0.43	0.83	2.26	0.93
	30 °C, 2nd	0.49	1.09	1.54	0.81
		0.48	0.90	2.16	1.15
	50 °C	1.52	2.67	5.83	2.84
		1.48	2.63	6.08	2.78
	70 °C	4.37	7.93	12.3	6.22
		4.31	6.66	13.8	5.97
FC	30 °C, 1st	1.25	2.59	5.83	2.77
		1.27	2.42	6.88	3.02
	30 °C, 2nd	1.49	2.57	6.69	2.75
		1.47	2.51	6.83	3.08
	50 °C	4.02	7.22	16.0	6.61
		3.99	6.50	18.1	6.81
	70 °C	11.8	19.6	30.9	14.0
		11.6	15.1	42.4	15.9

The authors measured the diffusion coefficient at three different temperatures: 30, 50 and 70 °C and observed that the hydrogen steady state flow increases as the test temperature increases and the time needed to develop the permeation transient decreases as the temperature increases (Figure 4.7). Moreover they found an Arrhenius type dependence of the permeation coefficient ($\Phi = \Phi_0 \exp(- E_\Phi / RT)$) on the temperature with an activation energy of 34-38 kJ/mol.

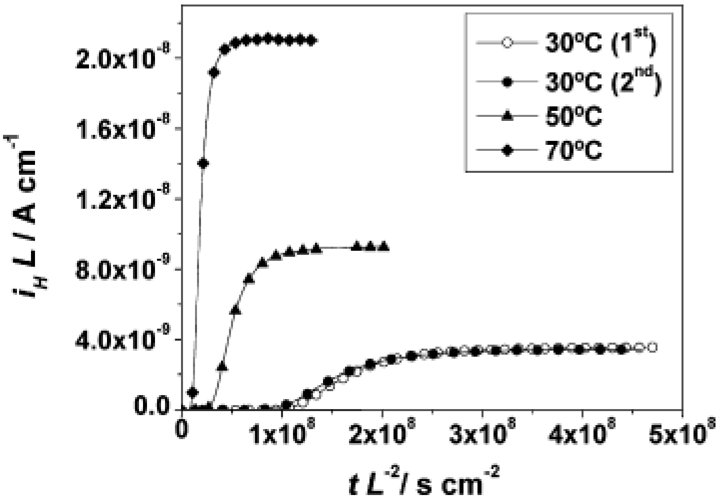

Figure 4.7 - Hydrogen permeation rising transient (T500 condition) [49].

From Table 4.7, it is possible to see that, fixing microstructure and temperature, the values of diffusion coefficient always depend on the method of determination. About the microstructure, they found that the highest values of the diffusion coefficient are observed in the AC and FC conditions. They noted that these microstructures (quenched martensite and annealed ferrite respectively) are very different concerning microhardness and XRD peak (see Figure 4.8). The same is observed also with T300 and AR conditions, which have almost the same D value in spite of markedly different tempering conditions. It is clear that there is no correlation between the hardness and the diffusion coefficient, as Figure 4.8 illustrates. The lowest diffusion coefficient is verified for T500 condition with a value about 20 times lower than FC condition. Diffusion coefficients for different microstructures do not follow the order of the usual dislocation density which is presents in a given microstructure, so the authors suggest that the fine precipitated carbides present play the main role in hydrogen trapping, while the dislocations have a secondary effect.

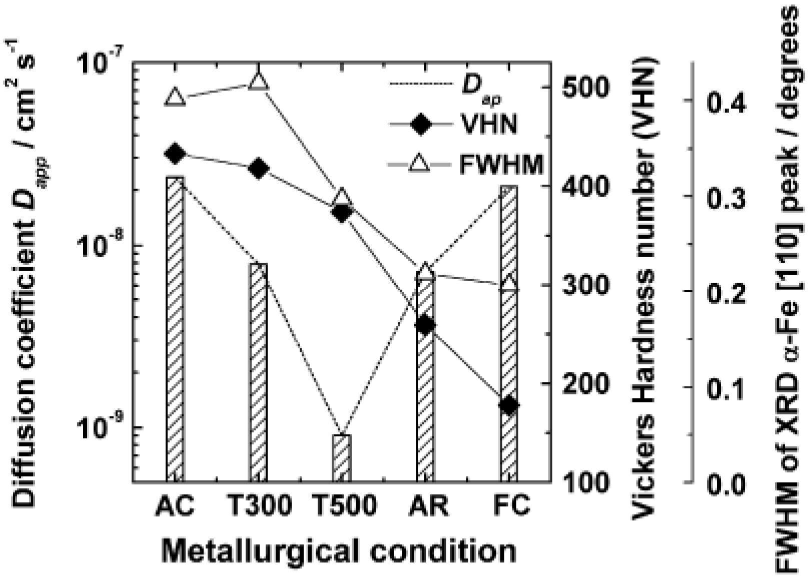

Figure 4.8 - Relationship between hydrogen diffusion coefficient, Vickers hardness and FWHM of the α-Fe [100] peak for different metallurgical conditions [49].

4.2.6 Other results

Other relevant outturns are summarized below and put in a resuming table in ANNEX with other related information such as the employed solutions, exit side coating, and electrochemical parameters.

Ly et al. [42] analyzed very high strength steels with hydrogen permeation, due to their susceptibility to hydrogen embrittlement. They found, like other scientists did, that the finer the microstructure is, the lower the diffusivity is, or better, looking at the considered steels, the higher mechanical properties are, the higher the fraction of volume of austenite is, the lower diffusivity is. Furthermore, they observed that diffusivity is systematically higher when calculated from decay. They attributed this behaviour to trapping and surface problems during build-up transient, which shows a lower value. They also noted surface condition evolution at the entry side, probably due to surface degradation (oxide barrier) or hydrogen evolution.

Dong et al. [44], [45] estimated the diffusion of hydrogen and density of traps in X70 and X100 steels, focusing on the healing treatment of cracks induced by hydrogen charging of X70 and the HIC behaviour of X100.

Ramunni et al. [46] studied the nature of three morphologies (pro-eutectoid ferrite + fine pearlite, spheroidized structure and aged structure) of the cementite as trapping sites at 27°C in SAE 1008 type, low carbon steel. The results showed that hydrogen is reversibly trapped in each case and also that the kinetics of H permeation in low carbon steel is considerably altered by the morphology of the cementite, presence of fine cementite in the aged ferrite increases solubility and reduces H diffusivity in the studied steel. When arranged in layers as in the pearlite, it increases the diffusion coefficient and reduces solubility. On the other hand, the spheroidized structure presents intermediate values in comparison with the previous values. Binding energies in the interval of 10–50 kJ/mol H are obtained, corresponding to the weak and strong interaction of H with the trapping sites.

The results reached in the Parvathavarthini's paper [35], concern the analysis of hydrogen diffusion in F22 ferritic steel with water quenching, air cooling or furnace cooling heat treatments. They can be summarized as follows: the apparent diffusivity shows an ascending trend with increasing degree of tempering due to annihilation of lattice imperfections, reduction in grain boundary area and reduction Cr and Mo solute content during tempering.

In order to give completeness to my research, in Figure 4.9 the result of comprehensive review made by Woodtli and Kieselbach is reported [48].

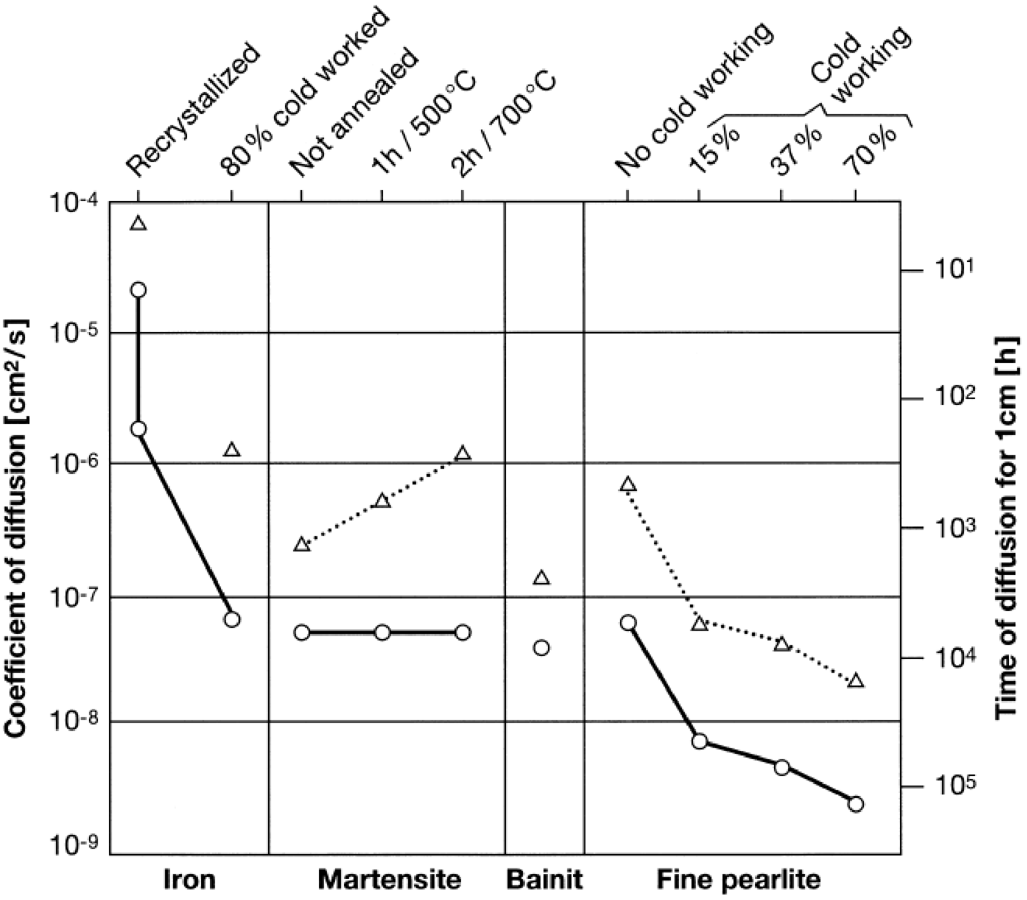

Figure 4.9 - Hydrogen diffusion coefficient in differently structured steels built up during hydrogen loading (solid line) and effusion (dotted line) [48].

In conclusion, the diffusion coefficients measured with Devanathan and Stachurski's based method on the complete permeation curve is very dispersed and not much reproducible.

This poor reproducibility is evident also into a single set of tests. The resulting diffusion coefficient is influenced, as efficaciously resumed by Haq [40], by solution used in the test, the presence of promoter and their concentration, the method used to calculate D, the presence of Pd coating, the charging condition, etcetera. So this value is not only due to physical diffusion and trapping phenomena, but it is also conditioned by anodic and cathodic surface phenomena.

The literature review does not give any generalizable trend, every conclusion seems to be ad hoc build based on specific results, without any general beforehand predictive model.

5) ANALYSIS OF PERMEATION TECHNIQUES

5.1 Devanathan and Stachurski's permeation technique

In 1962, Devanathan and Stachurski described an electrochemical technique for the accurate measurement of the instantaneous rate of hydrogen permeation through metallic membranes [25]. This membrane is placed in the middle of two halves cells, as shown in Figure 5.1 with all the details.

This kind of experiment can be performed properly if the adsorbed atomic hydrogen on cathodic side (the entry side) is maintained at certain fixed level, while on the anodic side (the exit side) it is always zero. The two scientists obtained these conditions through cathodic polarization of the entry side and anodic polarization of exit side of a Pd membrane by the use of potentiostatic circuits. On the surface in contact with cathodic side, hydrogen is reduced from ion form H^+ to atomic form H, it is adsorbed on the surface and then it diffuses through the sample. When hydrogen reaches the other surface, in contact with anodic side, it is oxidized to the H^+ form. The current in the anodic potentiostatic circuit, which maintains zero coverage on the exit side, is a direct measure of the instantaneous permeation rate of hydrogen, due to the Faraday laws:

$$\Delta W = \frac{MW}{z\,F} \cdot I \cdot t \qquad (1)$$

where ΔW is the mass of a produced specie (hydrogen ion in this case) during the electrochemical reaction, MW is the molecular weight of hydrogen atom, z is the valence of electrochemical reaction (equal to one in the present situation), F is the Faraday constant, 96.485 C, t is the time and I is the anodic current required to oxidize all the atomic hydrogen on the exit size. Therefore it is possible to record the instantaneous rate of hydrogen permeation continuously and with very high sensitivity.

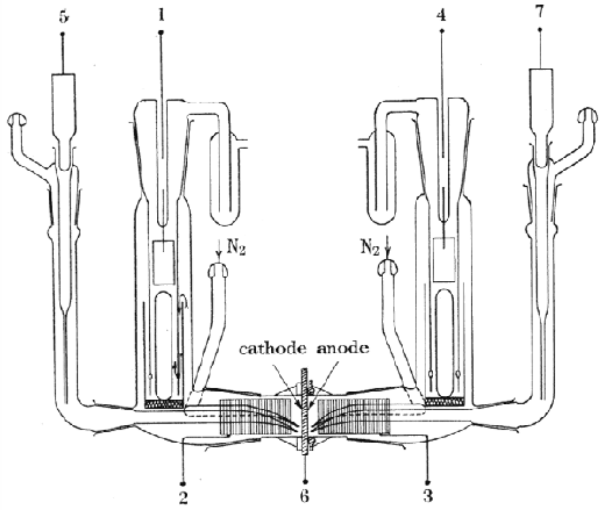

1 - Pt counter electrode in the cathodic side;

2 - cathodic side;

3 - anodic side;

4 - Pt counter electrode in the anodic side;

5 - reference electrode in the cathodic side

6 - sample membrane;

7 - reference electrode in the anodic side.

Figure 5.1 - Devanathan & Stachurski cell [25].

5.2 Developments in permeation techniques

From Devanathan and Stachurski's experiments lots of authors performed permeation measurements modifying the original set up in order to improve the quality of the result or to adapt the experiment to their specific purpose, i.e. different materials and different cathodic solutions. A great attention will be devoted to two specific operative techniques, ISO 17081 [21] standard and Zakroczymski's procedure [58], [59], because of their big relevance overall, and in particular for my thesis work.

5.2.1 Metal polarization selection

In order to maintain the same hydrogen activity on the entry side during all the experiment different it is possible to adopt different procedures. The cathodic side of the metallic membrane can be polarized in galvanostatic conditions, i.e. a constant current is imposed on its surface and the resulting electrode potential is monitored during all the experiment to check the stability of surface electrochemical conditions. Other Authors leave the cathodic side in free corrosion condition [23] and also in this case the electrode potential can be monitored. Lastly it is possible to adopt a potentiostatic control of the cathodic side measuring the current [38].

In the anodic side of the cell, it is necessary to guarantee the quantitative oxidation of the hydrogen atoms escaping from the membrane on this side without the disturbance induced by other possible electrochemical reactions, e.g., oxidation of the membrane metal or of other species contained in the anodic solution. When iron or steel alloys are used a passivating solution is usually adopted and a constant potential is imposed to the electrode with a suitable value to create and maintain a passive film on the anodic metal surface and to oxidize H to H^+. Passive film guarantees that only a very low corrosion current, i.e. passivation current, i_p, exists, but it does not disturb the measures of oxidation current which is at least two orders of magnitude higher.

5.2.2 Electrolytes selection

Devanathan and Stachurski [25] filled both cathodic and anodic compartments with 0,1 N of sodium hydroxide solution. In general anodic compartment solution is chosen to aid passive film formation of the membrane surface, so it is essential to use basic pH. NaOH is still the first choice, with a molarity from 0.1 to 0.2 mol L^{-1}.

On the other ends cathodic electrolyte may vary as follows. It may be be the same of anodic compartment as [25], [46], [59], it is sometimes formed by acetic solutions [55], solution with NaCl as [22], [55], [51], or solution with cathodic poison as [22], [55], [35], [44], [45]. It is also worth mentioning the possibility to use gaseous environments. This choice is usually done looking for the best mix to simulate the real sour condition, or searching the easiest way to create permeation condition. Moreover the flux condition is not fixed, so that it may be stagnant or not.

5.2.3 Thickness of the sample

Two aspects should be considered when we decide the thickness of sample:

- the diffusion of hydrogen must be controlled by transport though the bulk of the material, not by surface processes. Therefore the sample thickness must be higher than a critical minimum value [21].

- The greater the thickness is, the longer the test is, the harder is to keep constant conditions.

So the choice should be a compromise between these aspects.

Related to the right thickness choice, also the radius of membrane exposed to the solution should be considered; indeed only a sufficiently large ratio, radius over thickness, ensures one-dimension diffusion of hydrogen atom.

5.2.4 Use of palladium coating

The permeation method so far exposed is based on the assumption that every hydrogen atom which diffuses through the sample is instantaneously oxidized at the anodic side according to the reaction:

$$H \rightarrow H^{+} + e^{-}$$

in this way the anodic current, thanks to Faraday law, is a reliable measure of the hydrogen flow across the metal membrane. In particular the formation of molecular hydrogen on the anodic surface according the equation:

$$H + H \rightarrow H_2$$

Must be avoided.

Manolatos et alii [42] assert that the imposition of anodic potential is not always a sufficient condition to ensure a complete oxidation of hydrogen atom, due to the passive layer formed on the surface. They found that on a palladium surface, the oxidation reaction of hydrogen occurs in a faster and more complete way than on an iron surface as it is shown in Figure 5.2 for Armco iron.

Actually the anodic surface layer (passive layer or Pd coating) can have two effects: it is a barrier to hydrogen diffusion and is an electro-catalyst for hydrogen oxidation.

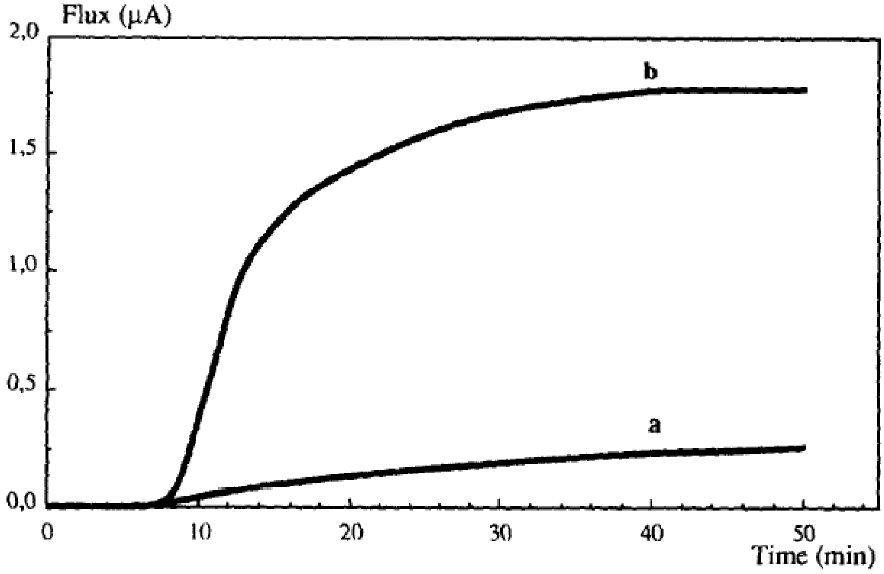

Figure 5.2 - Permeation curves (a) without Pd, (b) with Pd [42].

5.3 ISO 17081

Devanathan and Stachurski's electrochemical method was standardized in 2004 as ISO standard 17081 [21]. In particular:

- this standard specifies a laboratory method for the measurement of hydrogen permeation and for the determination of hydrogen atoms uptaken and transported in metals and alloys;
- it gives a method to determine effective diffusivity of hydrogen atom and to distinguish reversible and irreversible trapping;
- it gives requirements for the preparation of specimens, control and monitoring of the environmental variables, test procedures and analysis of results.

Below the main inputs of the ISO 17081 will be exposed and analyzed.

ISO standard gives some suggestions regarding the composition of the cathodic solution but it lets free to choose the solution, charging method (galvanostatic control, potentiostatic control, etc..) and to use or not palladium coating, but it demands to satisfy the conditions to have proper oxidation and reduction of hydrogen seen above, as the bulk transport-limited kinetics for oxidation of hydrogen atoms.

An example of a permeation cell can be seen in Figure 5.3. It consists in a two-compartmental environmental cell (charging and oxidation parts), constructed from inert materials, with reference and auxiliary electrodes.

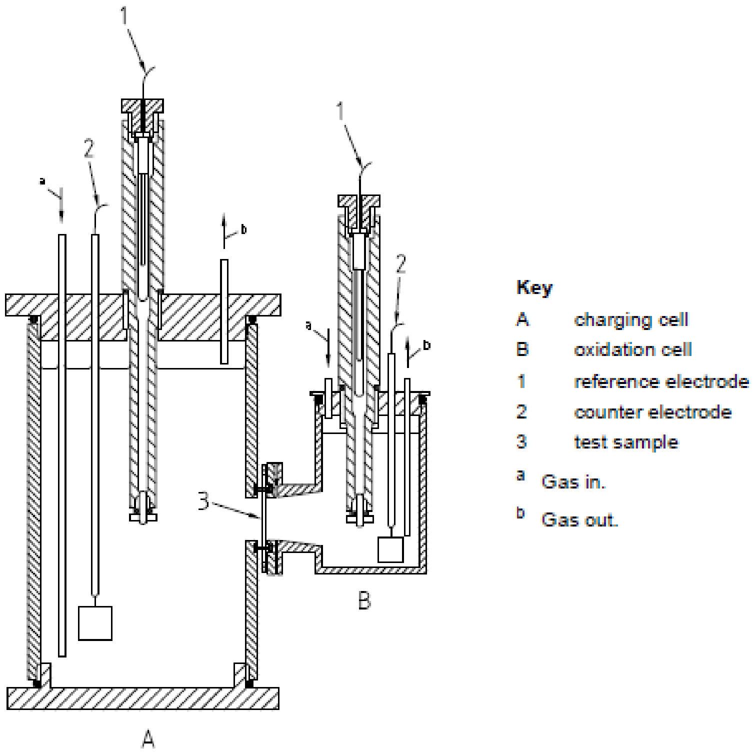

Figure 5.3 - Hydrogen permeation cell [21].

The test procedure can be summarized as follows:

- prepare the sample to the required surface finish, prepare the solutions, verify the reference electrodes and assemble the cell;
- add the solution to oxidation cell, deaerate it and switch on the anodic potentiostat;
- when anodic current has reached low and stable values, add the selected solution to the charging cell and commence galvanostatic charging or potentiostatic charging;
- monitor the total oxidation current (comprising background current and atomic hydrogen oxidation current) until steady state is achieved;
- in order to distinguish the effects of irreversible and reversible trapping on hydrogen transport, reduce the charging current to zero. Give sufficient time for hydrogen atoms in interstitial lattice sites and reversible trap sites may exit. Then repeat the charging procedure.

The last consideration gives a method to separate reversible and irreversible trapping phenomena, according to Turnbull studies [22], [23], indeed during the first charging hydrogen diffuses through the lattice and occupies both reversible and irreversible trap. When we discharge the sample (switching off the current and waiting for the desorption), hydrogen which is trapped in reversible traps comes out while hydrogen in the irreversible traps has not enough energy to escape. So when the second charge is performed, hydrogen can only occupy reversible traps, diffusing at a different apparent rate respect to the first permeation run.

Once the test is over, the result is analyzed. The following equation is available to calculate the sub-surface concentration of hydrogen in the lattice sites at the charging surface, from the steady-state permeation current:

$$J_{SS} = \frac{I_{SS}/A}{F} = \frac{D_L C_0}{L} \tag{2}$$

where

J_{SS} = atomic hydrogen permeation flux at steady-state as measured on the anodic side of the sample;

C_0 = sub-surface concentration of atomic hydrogen in interstitial lattice sites on the cathodic side of the sample;

A = exposed area of sample in the anodic cell;

F = Faraday constant;

D_L = lattice diffusion coefficient of atomic hydrogen;

L = thickness of the sample.

When only reversible trapping is important and the permeation transient for this case can be represented by Fick's second law, the sub-surface concentration of hydrogen atoms in lattice and reversible trap sites can be calculated from the following equation:

$$J_{SS} = \frac{D_{EFF} C_{0R}}{L} \tag{3}$$

where

D_{EFF} = effective diffusion coefficient of atomic hydrogen based on elapsed time corresponding to $J(t)/Jss = 0.63$;

C_{0R} = summation of the sub-surface concentration of hydrogen in interstitial lattice sites and reversible trap sites on the charging side of the sample.

The following equation is used to calculate the effective diffusion coefficient based on the elapsed time for *J(t)/Jss* = 0.63:

$$D_{EFF} = \frac{6L^2}{t_{lag}} \tag{4}$$

or it is possible using the next one:

$$D_{EFF} = \frac{15.3L^2}{t_b} \tag{5}$$

Standard underlines that results of Eq. 4 and 5 should be in agreement if Fick's second law is applicable.

To verify the applicability of Fick's second law concerning the permeation transient, plot the permeation transient in the form of normalized flux against the logarithm of normalized time $\tau = D_L t/L^2$, as shown in Figure 5.4, and compare the experimental transient with the one derived from Fick's second law.

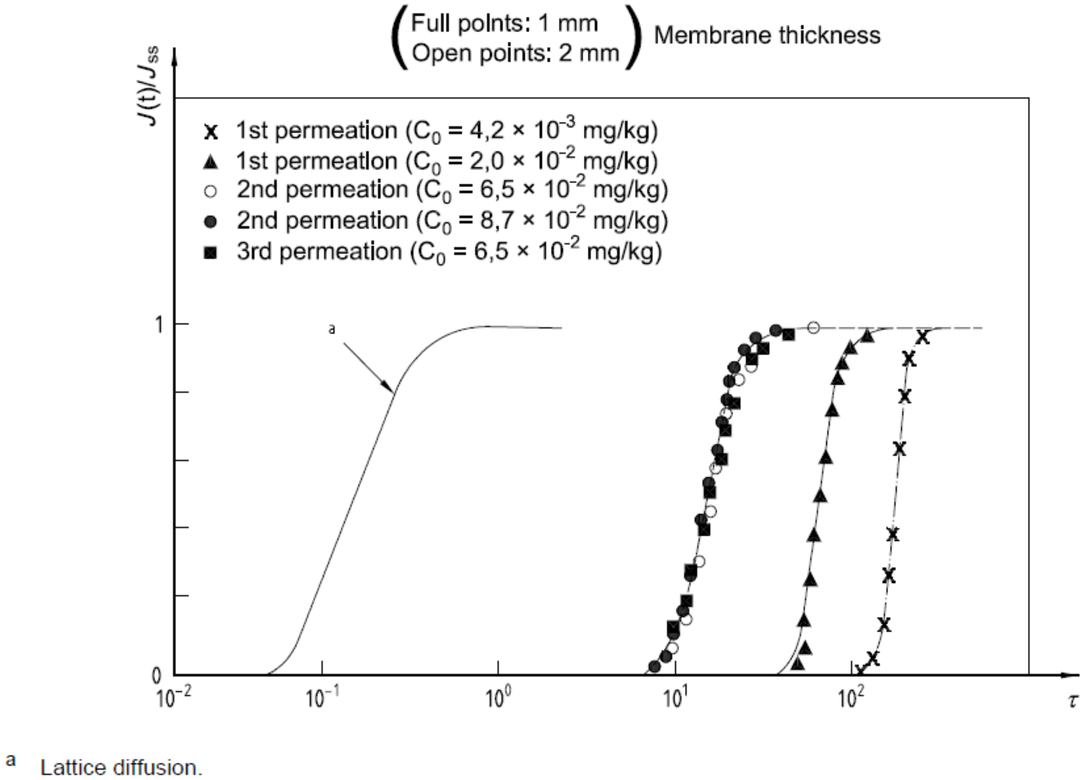

Figure 5.4 - Rising permeation transients [21].

According to ISO Standard, if the normalized permeation transient is steeper than predicted by Fick's second law, this indicates that trap occupancy is significant, while a permeation transient which is less steep than predicted by Fick's second law is often an indication of unsteady surface conditions.

When peaks in the transients are observed, this implies the value of the effective diffusivity is also varying with time and analysis is uncertain, but Eq 4 may be used as an empirical estimate for $J(t)/Jss = 0.63$.

The extent of reversible and irreversible trapping can be evaluated comparing the first and second permeation transients as in Figure 5.4. If the first permeation transient takes longer than the second permeation transient, i.e. the normalized permeation curves are displaced to longer times, it can be deduced that irreversible traps exist and affect permeation. Moreover, in the absence of voids formation, second and subsequent transients shall concur, provided their values are similar.

ISO standard points out that problematic issues might arise in specific situations, leading to warp results or invalidation of the experiments. The two most important are [21], [57], [58], [59]:

- trapping;
- electrochemical surface alteration.

The first problem concerns the presence of traps, with reactions like Me + H → MeH which act concurrently to the base lattice motion of hydrogen. So both reversible and irreversible traps subtract hydrogen to the lattice diffusion and physically obstruct hydrogen atom transfer. These effects should be evaluated since every "real" metal specimen contains traps and even second transients display unsaturated reversible traps and saturated traps as obstacles.

The second problem involves cathodic surface changes of the sample due to its electrochemical polarization. In particular, it concerns the assumption that hydrogen activity on the entry side is constant during the test time. On the contrary, the electrochemical conditions at the cathodic surface of the specimens cannot be considered constant in many different conditions but it varies with time [52], [53], [54], [55], [56].

5.4 Zakroczymski's procedure

In order to eliminate the undesirable effects of surface processes alteration and trapping described in the last paragraph, Zakroczymski [58], [59] elaborated a different approach to the measurement of the diffusion coefficient by means of the permeation electrochemical technique. The key of this approach is to arrange the suitable experimental conditions under which the role of these disturbing effects is negligible and the measured permeation rate is controlled by the rate of hydrogen diffusion. A typical experimental procedure is made as follows [59]:

1. Into a Devanathan and Stachurski's cell, a metal membrane (Armco iron in Zakroczymski's test) is charged at its cathodic side with hydrogen (Figure 5.5) and it is anodically polarized at its exit side, which is covered by palladium. When maximum current value is reached, cathodic charge must be continued for a time long enough to achieve steady-state physico-chemical cathodic condition and equilibrium of both reversible and irreversible trapping reactions [60]. In Zakroczymski’s test this phase lasted about 100 hours.

2. Once steady-state conditions are achieved, limited variations of cathodic current are fixed and partial decay followed by build-up transients are performed changing the cathodic current as shown in Figure 5.6. These steps allow to measure permeation transients without perturbing significantly electrodic and trapping equilibria. The permeation and desorption transients can be expressed by the equations 14 and 15 included in Paragraph 3.4.

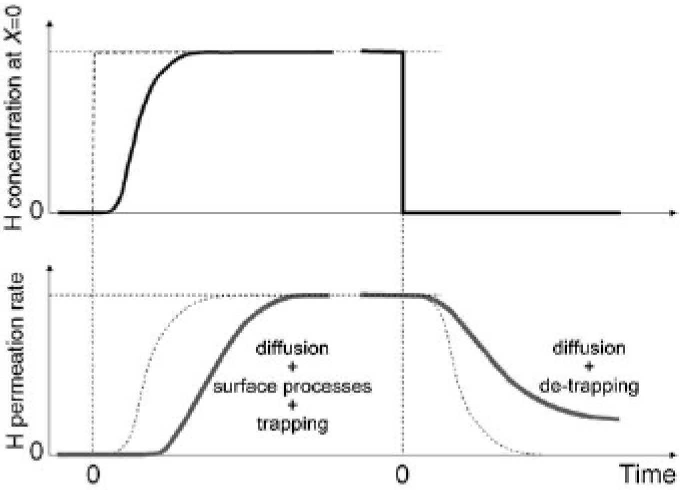

Figure 5.5 - Charging transient and its respective complete desorption [59].

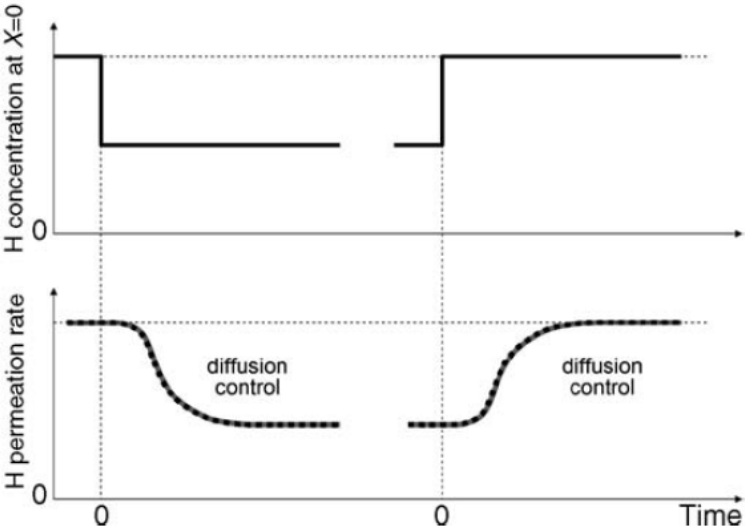

Figure 5.6 - Partial decay and build-up [59].

So, the solution proposed by Zakroczymski to eliminate the problematic issues underlined by ISO can be summarized as follow: the electrochemical surface effects are eliminated by a sufficient long and uninterrupted cathodic polarization [60], the trapping effects are minimized by successive transients with partial increasing or decreasing cathodic polarization.

The elimination of trapping and surface effects allows to measure the real diffusivity of hydrogen, with a lattice diffusion coefficient D_L, in Armco iron during partial transient. It means that the permeation curve follows very well Fick's law (Figure 5.7), it is not necessary to introduce more complicated equations with ad hoc parameters. On the other hand, first transients and complete desorption cannot be described in the same way due to trapping and surface effects, so the resulting diffusion coefficient is not representative of lattice properties.

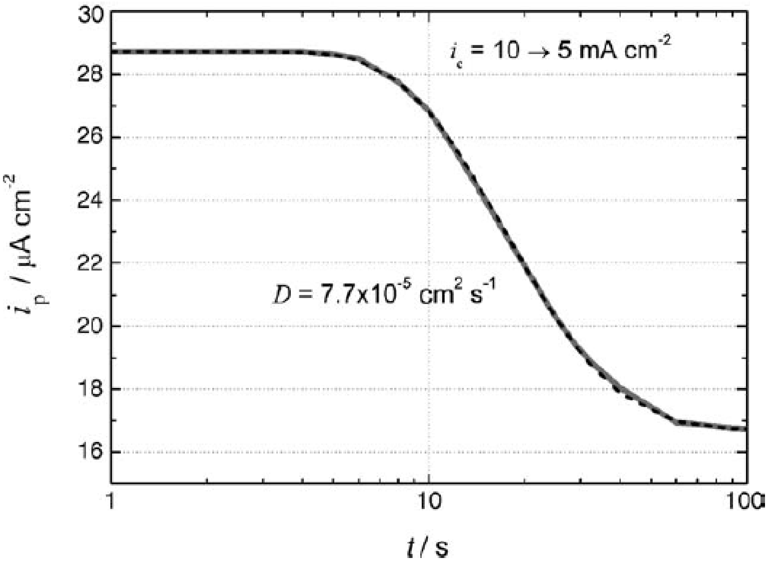

Figure 5.7 - Partial permeation decay transient. Solid line represents experimental transient, dashed line is used for theoretical curve [59].

Another important contribution of Zakroczymski method is the analysis of complete desorption.

When the hydrogen charging is stopped, hydrogen leaves the membrane both from the entry and from the exit side, but if different solutions are used on the cathodic and on the anodic side of a Devanathan and Stachurski's cell and in particular when the cathodic solution is not passivating it is not possible to measure hydrogen desorbed from both sides. Zakroczymski used soda solution for cathodic cell too so when cathodic charging is switched off the entry side can be immediately polarized at the same potential of anodic side and hydrogen oxidation currents of both surfaces are measured to calculate the desorption rate of hydrogen. Obviously anodic current of the entry side must be corrected by the passivation current of the material.

In this way it is possible to measure all hydrogen escaping from the membrane and to calculate how much is flowing out from the lattice and how much from the reversible traps in the following way: the Figure 5.8 shows an example of hydrogen desorption rate at the membrane exit side, i_H. This desorption rate is the sum of desorption of the diffusible and the trapped hydrogen, with the area under the i_H curve corresponding to the total amount of hydrogen per unit area, q_H. We know the lattice diffusion coefficient D_L form the previous partial transient work, so we can plot the theoretical curve with this value of D_L , obtaining i_{Hd},, the desorption rate curve for the diffusible hydrogen. The area under this curve is the quantity of diffusible hydrogen q_{Hd}. Now, subtracting the second area to the first, it is possible to estimate the amount of hydrogen originated from traps q_{Ht}.

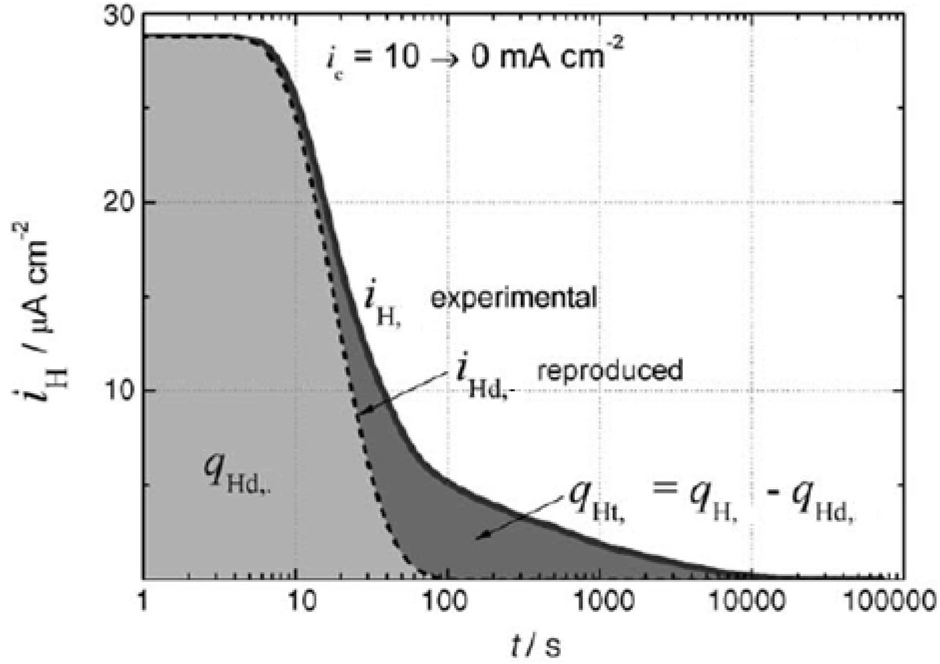

Figure 5.8 - Complete desorption analysis (adapted from [59]).

6) METALLURGICAL CHARACTERIZATION AND EXPERIMENTAL PROCEDURE

6.1 Micro-Alloyed steel API 5L X65 grade

Permeation tests have been carried out on micro-alloyed steel samples, API 5L X65 grade, which have been obtained from quenched and tempered seamless line-pipe with dimensions 323 mm OD x 46mm WT [3], [4], [8]. X65 is a C-Mn steel, it is micro-alloyed with Nb and V but it has also a small amount of Cr, Mo and Ni to improve hardenability and Ca for the inclusion shape control. In Table 6.1 the chemical composition of this material is reported which conforms to API 5L Specification requirements [62]. The material is sour service use, so that it underwent through all the required qualifications.

Table 6.1 - Chemical composition of API 5L X65 used (wt%).

Steel	C	Mn	S	Mo	Cr	Ni	Nb	V	Ti
X65	0.11	1.18	0.007	0.15	0.17	0.42	0.023	<0.06	<0.01

In Table 6.2 tensile test results at room temperature of X65 in as received condition, i.e. Q&T as stated above, are reported. The samples in this metallurgical condition will be indicated henceforth with the label X (e.g. X1, X2, etc..) or simply X65.

Table 6.2 - Mechanical properties of as received X65 steel.

Steel	X65
Yield strength (MPa)	511 ± 6.7
Ultimate tensile strength (MPa)	609 ± 5.7
Young's modulus (GPa)	206 ± 6.0
Elongation (%)	21 ± 6.5

In order to evaluate microstructural effect on material diffusion properties, some samples were fully quenched, i.e. they were put in a furnace at 930°C for 30 minutes, in order to austenitize them completely, and afterwards they were water quenched (Figure 6.1). Quenched X65 samples will be indicated henceforth with the label XQ (e.g. XQ1, XQ2, etc..).

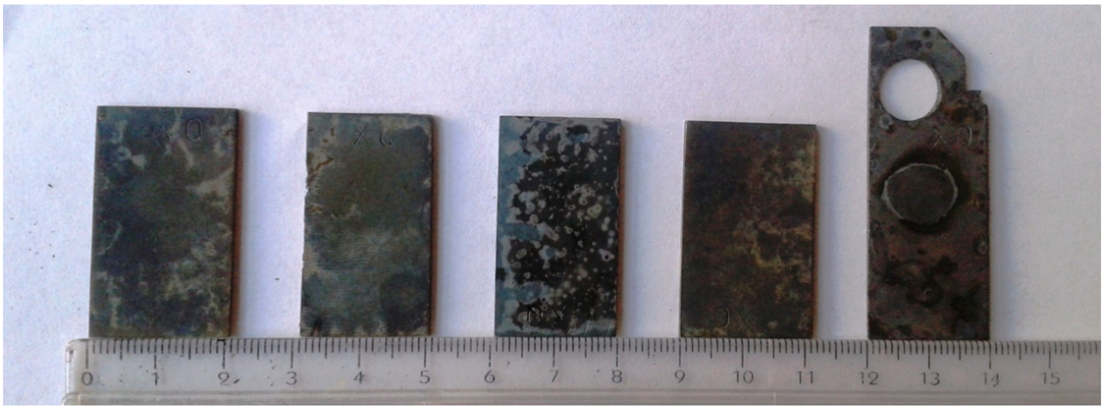

Figure 6.1 - XQ samples.

Other samples were put into the furnace at room temperature, the temperature was increased till 930°C, then the temperature was kept constant for 30 minutes. At the end the furnace was switched off, so the samples cooled down very slowly to the room temperature. The heating and cooling rate of the furnace are illustrated in Figure 6.2. These samples were subjected to annealing heat treatment, so they will be indicated henceforth with the label XA.

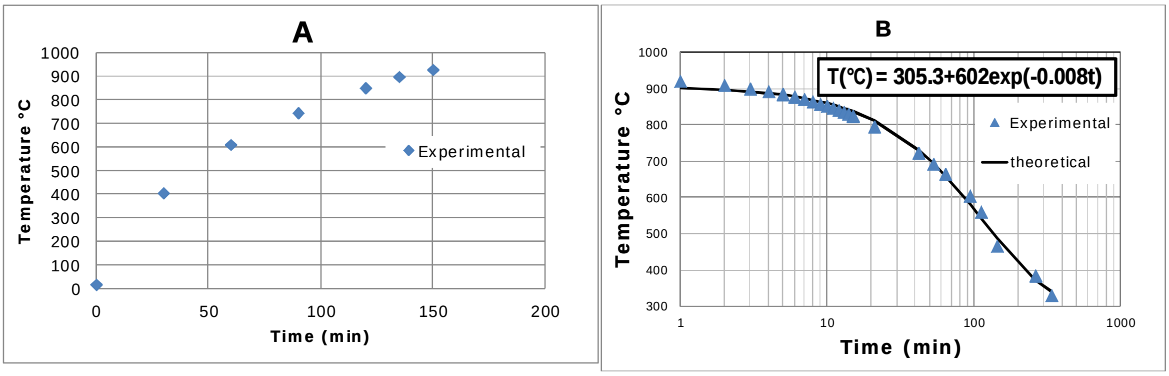

Figure 6.2 - XA heating rate (A) and cooling down (B).

6.1.1 Metallurgical characterization of X65 different microstructures.

The microstructure of as received X65 steels consists in equiaxed and acicular ferrite with finely dispersed carbides (Figure 6.3, all the sample are prepared for micrographic examination with Nital 1 etching), it is rather homogeneous, no significant variances are visible among different alignments (internal, centre, external) or for different orientations (longitudinal, transversal). In Figure 6.4 a representative SEM image of this microstructure is reported. Inclusion shape is round (type D globular inclusions), as it is expected for a sour service material treated with calcium. The microhardness value is 206.3 ± 7.9 HV, while the grain size area is 39.4 ± 1.4 μm^2. Also the inclusion content has been estimated as percentage of the area of a sample occupied by inclusion, divided by the total area. The mean value for as received samples is 0.1% with a standard deviation of 0.04%.

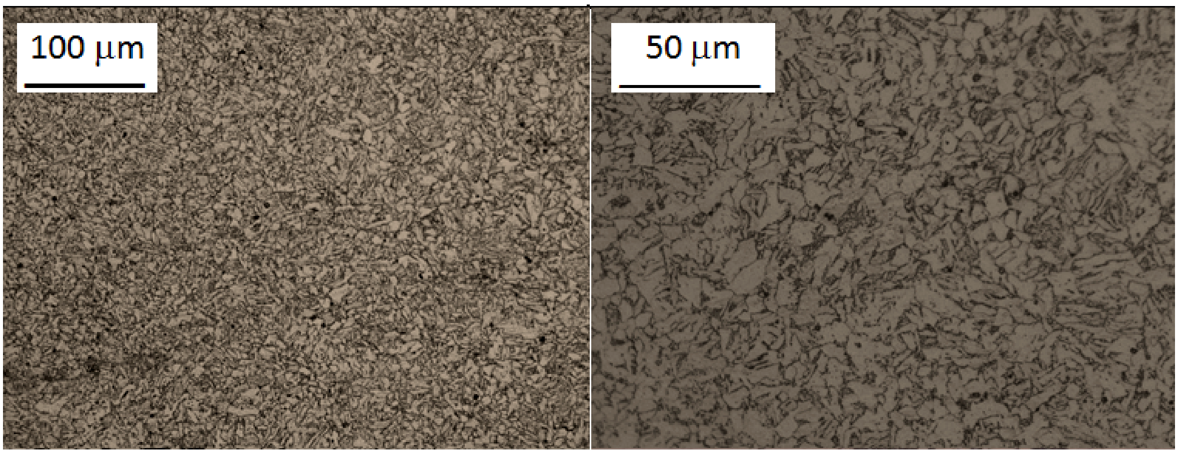

Figure 6.3 - As received X65 sample images by light microscope.

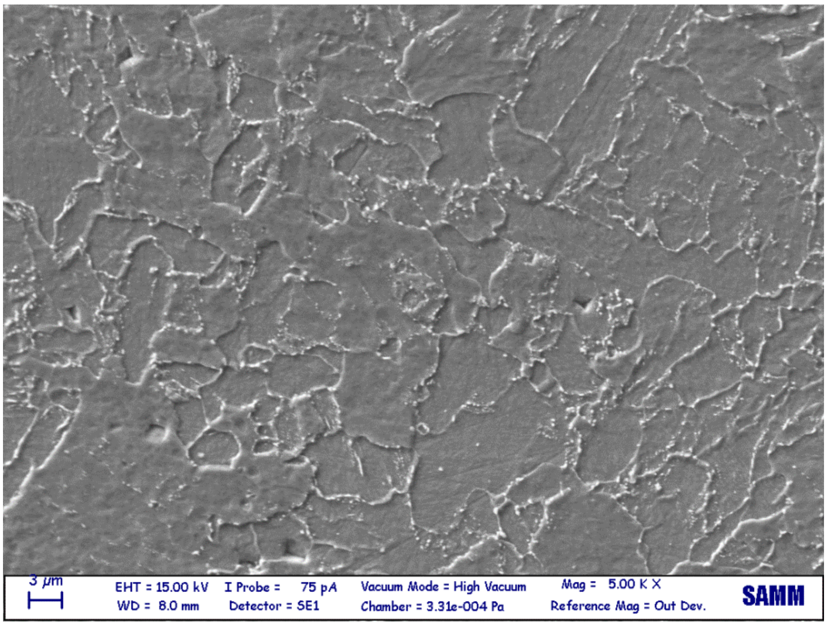

Figure 6.4 - As received X65 sample image by SEM.

The microstructure of XA, shown in Figure 6.5, consists in ferrite grains of not homogeneous dimensions and islands of pearlite. In Figure 6.6 a representative SEM image of this microstructure is reported. Note the clear visible fine pearlitic structure. The microhardness value is 149.8 ± 19.2 HV and the grain size area is 110.9 ± 24.6 μm^2. The mean value of percentage of inclusion for as received samples is 0.1% with a standard deviation of 0.02%.

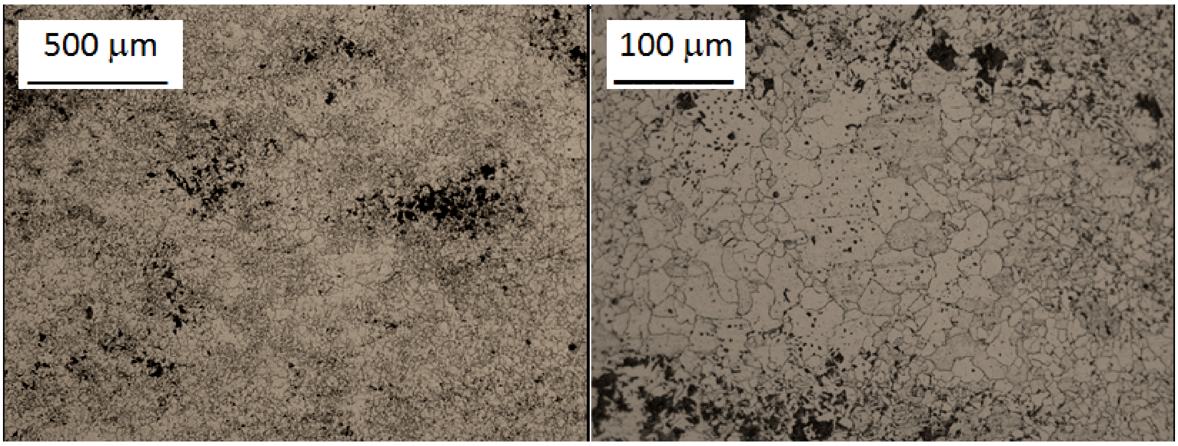

Figure 6.5 - XA sample images by light microscope.

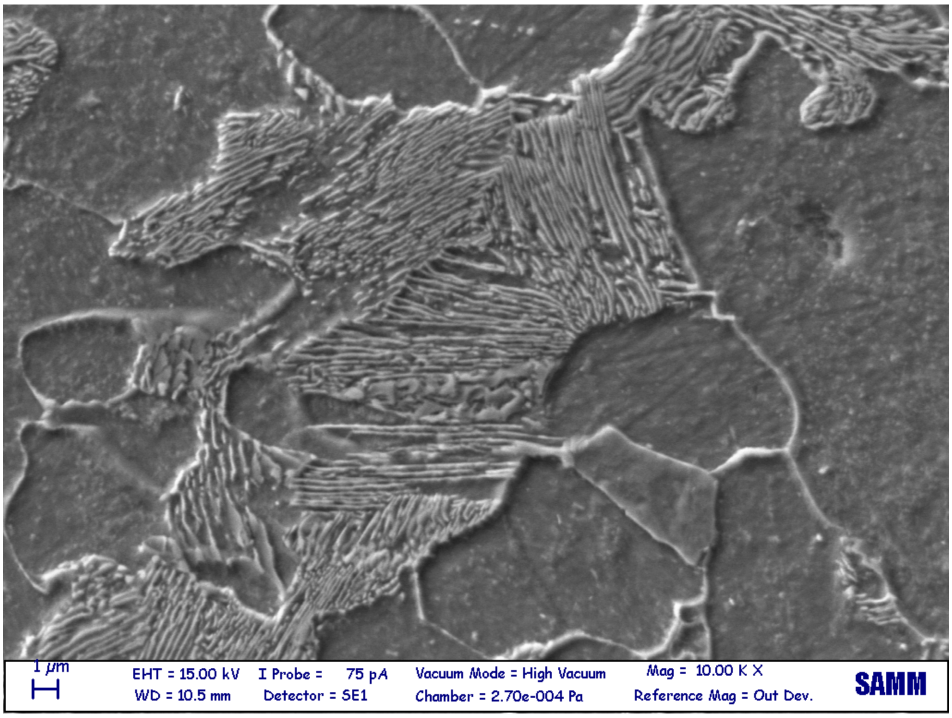

Figure 6.6 - XA sample image by SEM.

The microstructure of XQ, as shown in Figure 6.7, is almost completely martensitic with a microhardness rather homogeneous, equal to 433 ± 33.7 HV, which is compatible with the observed microstructure. In the Figure 6.8 SEM image of this microstructure is reported. The mean inclusion density value for quenched samples is 0.1%, with a standard deviation of 0.05%. The density of inclusion is almost the same for all the microstructures, as we expected because heat treatment should not alter this constituent.

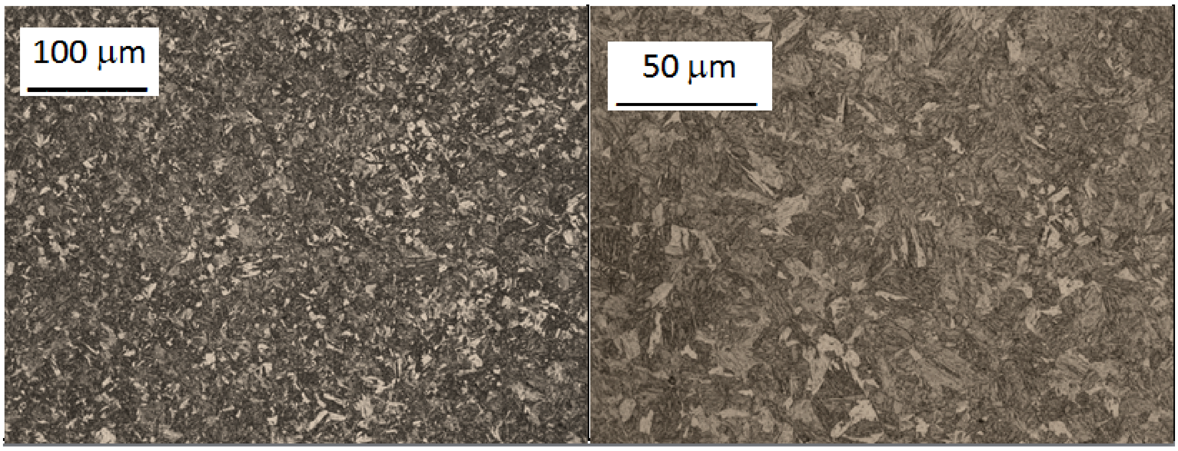

Figure 6.7 - XQ sample images by light microscope.

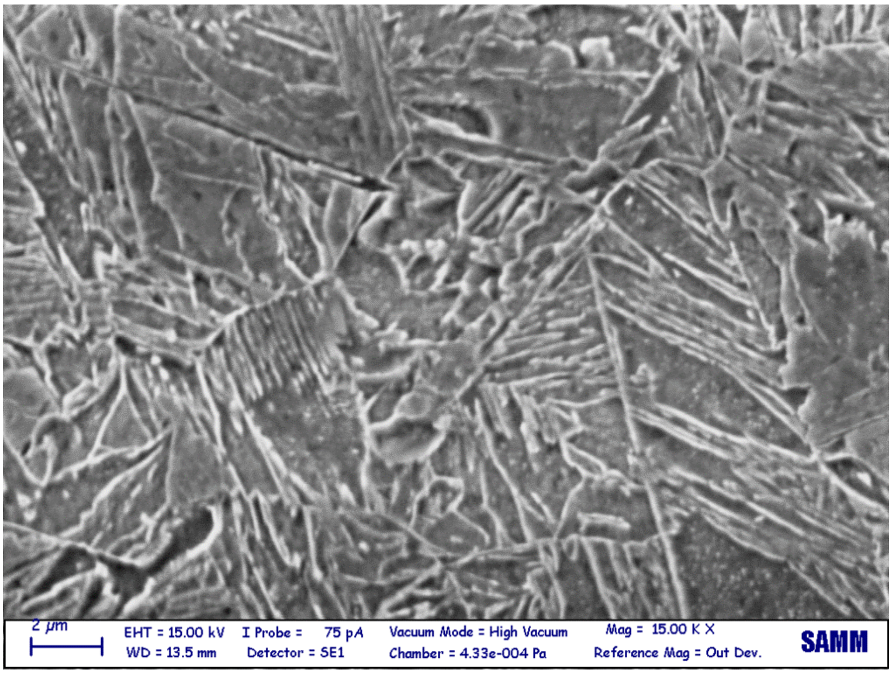

Figure 6.8 - XQ sample image by SEM.

6.1.2 Preparation of the samples for the permeation test.

The permeation test samples are membranes with dimensions ≈ 20•40 mm^2 and 1.3 mm ± 0.15 mm thick, they were obtained cutting a piece of pipe perpendicular respect to his radius in order to simulate hydrogen radial diffusion. The surfaces are then prepared in the following way:

1. Mechanical preparation of both surfaces with emery papers of decreasing abrasive particle dimensions till 1200 grit (SiC as abrasive medium, water as cooling medium);
2. brazing of copper electrical connection;

3. cleaning of the sample with ethyl alcohol;
4. masking the surface with kapton® tape, with a free square area ≈ 2.2 cm^2 in the anodic part;
5. pickling in 37% HCl till uniform and copious hydrogen evolution develops (few seconds);
6. application of palladium coating (≈0.1μm homogeneous and adherent layer) by palladium solution, 28.5% NH_4OH + 5 g L^{-1} $PdCl_2$ and cathodic current of 2mA (E vs Ag/AgCl = - 1.00 V) for 5 minutes;
7. cleaning with distilled water and ethyl alcohol;
8. removal of masking tape and cleaning with trichlorethylene;
9. Mechanical preparation of cathodic surface with 1200 grit emery paper and final cleaning with ethyl alcohol.
10. Prepassivation (cathodic and anodic area): in a baker, anodic polarization of the sample with +200 mV vs. Ag/AgCl in 0.2 mol L^{-1} NaOH solution has been performed till the current density reached values lower than 0.1 μA cm^{-2} (about 1-2 hours). The anodic area devoted to this treatment must be larger than the part involved to the following hydrogen oxidation in order to protect the parts from crevice corrosion, which may develop in correspondence to possible palladium film porosity. This phenomenon caused the interruption of some tests.

The sample appearance after these preparation steps is shown in Figure 6.9.

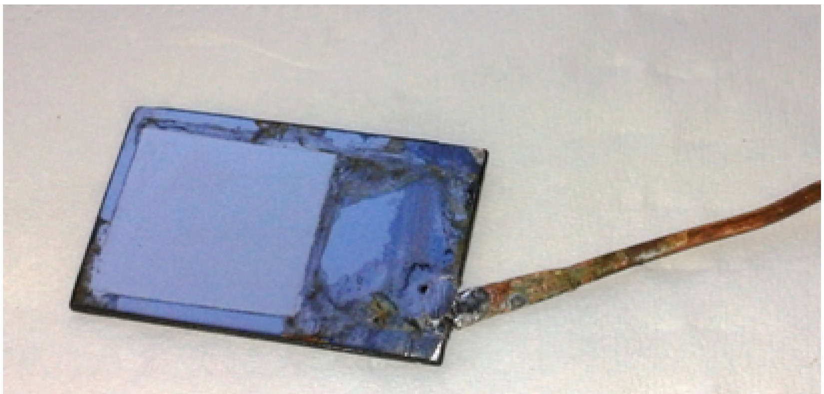

Figure 6.9 - Sample ready to permeation test. Note the mirror like palladium surface in the middle of anodic surface.

6.2 Experimental apparatus

Permeation experiments were carried out on a modified Devanathan and Stachurski's cell [25], according to ISO 17081 [21], as it is illustrated in Figure 6.10. The apparatus was composed by two glass compartments, junction caps, made by polycarbonate and polyvinyl chloride, were used between the two compartments which held the samples, and Viton® O-rings were applied for sealing. The sample exposed area to the cathodic solution (entry side of hydrogen) was 1.54 cm^2, the ratio between anodic and cathodic area was 0.9, as the standard recommends [21].

Cathodic and anodic solutions were kept constant at 20 ± 2°C by means of a thermostat linked to two jackets which surrounded the compartments.

A complete description of the design of the apparatus is reported in [61].

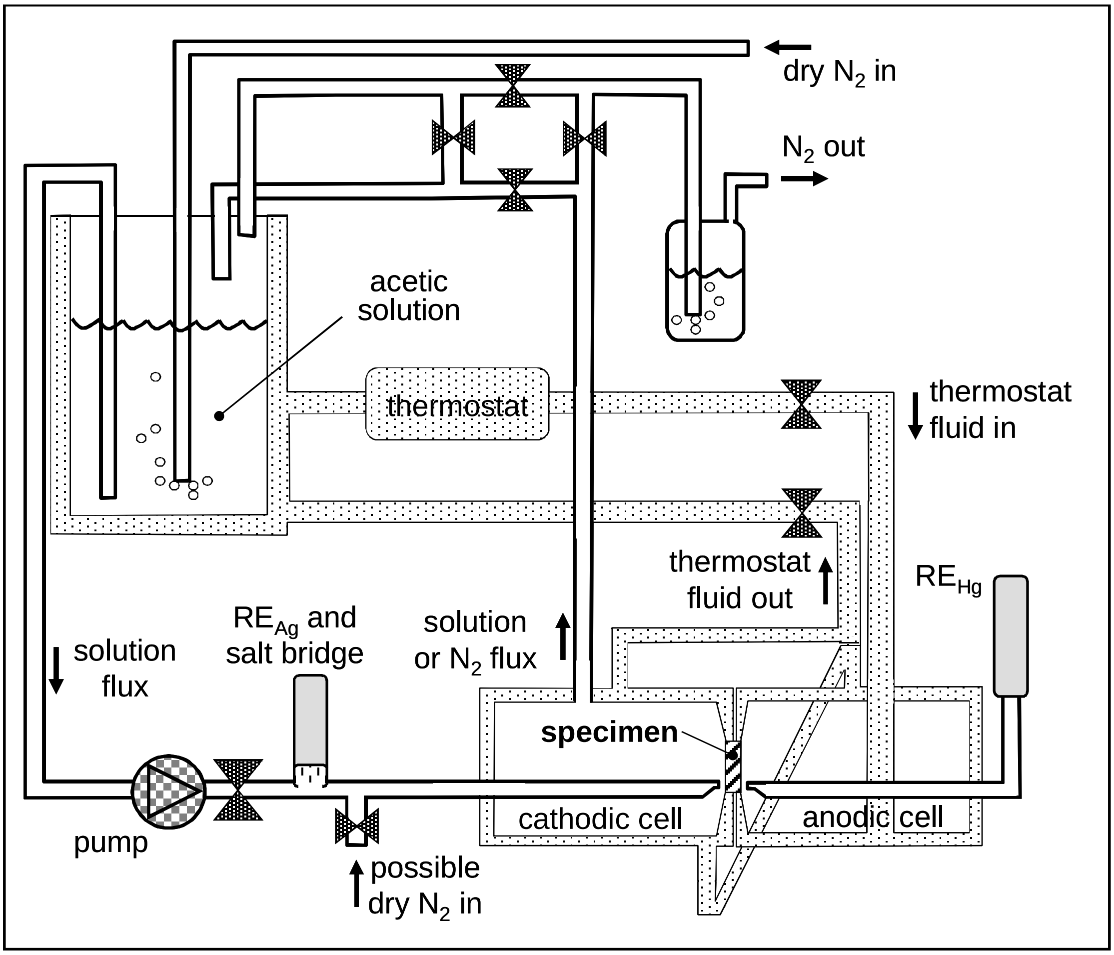

Figure 6.10 - Process flow diagram of the whole experimental apparatus.

6.2.1 Cathodic side

The cathodic solution used in all the experiments was 0.4 mol L^{-1} of acetic acid (CH_3COOH) plus 0.2 mol L^{-1} of sodium acetate (CH_3COONa), pH=4.2. The use of a peristaltic pump (flow rate=8.5 L h^{-1}) minimizes the alkalinity accumulation on the surface and guarantees a continuous flux of the solution on it with a velocity at the end of the capillary tube ≈ 1m s^{-1}. In order to have a sufficient solution turnover , the pump takes the acetic solution from a 5 L reservoir. It is worth mentioning that the pump was enclosed in a Faraday's cage, due to the system sensitivity to the electric alterations.

In order to eliminate the detrimental effects of oxygen like the reduction of O_2, this solution was purged by dry nitrogen into the reservoir.

The reference electrode used in this part of the cell was double junction Ag/AgCl/3 mol L^{-1} KCl// (E≈0.200 V vs. SHE at 20°C), the counter electrode was a platinum wire with a surface of about 1.5 cm^2. The capillary tube used to input the solution against the surface had also the function of Haber-Luggin capillary (see the Figure 6.8).

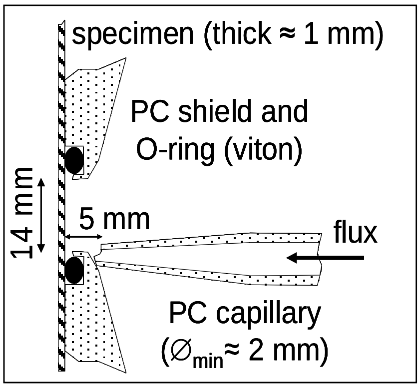

Figure 6.11 - Luggin capillary tube scheme used for the cathodic solution input and for the measurement of the potential.

6.2.2 Anodic side

Anodic cell was filled with ≈250 cm^3 of 0.2 mol L^{-1} stagnant NaOH solution; this solution was not de-aerated.

A double junction Hg/HgO/2.5% KOH// (= 0.446 mol L^{-1}) was used, its potential was -0.08 V vs. Ag/AgCl/3 mol L^{-1} KCl. The counter electrode was the same of cathodic cell.

6.3 Permeation procedure

Experimental tests in the present work have been performed in the following way:

1. Passivation: the sample has been assembled in the cell, the anodic compartment has been filled with NaOH solution, anodic polarization of 0.1 V vs. Ag/AgCl has been performed and the passivity current has been measured till current density became

lower than 0.1 μA cm^{-2}. During passivation of the anodic surface, the cathodic compartment was maintained under dry nitrogen flow.

2. Charge: while the anodic current density was continuously measured, the other compartment has been filled with acetic solution and the cathodic side of the sample was polarized (galvanostatic) at constant current density of -0.5 mA cm^{-2}. This testing phase lasts about 100 hours.
3. Partial charge: after phase 2, cathodic current density has been increased from -0.5 mA cm^{-2} to -1 mA cm^{-2} and then kept constant till the anodic current reached quasi-stationarity situation. This part lasts less than 2 hours.
4. Partial discharge: once quasi-stationary anodic current density had been reached, the cathodic current density was decreased from -1 mA cm^{-2} to -0.5 mA cm^{-2}. This phase lasts till a new steady state has been reached (less than 2 hours).
5. Discharge: after phase 5, cathodic polarization has been interrupted. The anodic current density has been continuously measured till passivity current achievement (>0.1 μA cm^{-2}). This part lasts some tens of hours.
6. Second cathodic polarization: the same procedure has been then performed on the same sample, from point 2 to point 5.

It is worth to underline that these measurements are very sensitive to even low chemical or physical variation of the cathode, so every single part of the experimental procedure has been optimized in order to avoid perturbation in the anodic current density due to cathodic routine operation during the test, such as cathodic compartment emptying or cathodic surface drying.

During the different phases listed above, the phenomenon we want to observe may have very different characteristic process times (orders of magnitude). So data recording has been optimized for every phase of the test, as summarized below:

- During prepassivation (1) the sample is outside the cell and it is important only when the anodic current value goes constantly below 0.1 μA cm^{-2}, so the latter was observed by the analogical display of potentiostat.
- During passivation (2) and charge (3), current density recording rate was 1 datum/minute.
- During partial charge (4) and partial discharge (5), 1 datum/second.
- During discharge (6), recording rate was 1 datum/second for about half an hour, then 1 datum/minute till the end of the test.

Also the values of cathodic potential have been recorded with the same rate.

The data acquisition system is composed by a digital multichannel data logger IMPVIEW 3595-4B by Solartron, which simultaneously measures the potential difference between cathodically polarized surface and Ag/AgCl reference electrode and anodic current. The anodic current is obtained thanks to 10,1 kΩ shunt resistance, which is put in series between Pt counter electrode and potentiostat.

7) THE RESULTS OF PERMEATION TESTS

7.1 Overview of polarization test

Permeation tests have been carried out with the method exposed in the Paragraph 6.3. These tests were performed on three annealed samples (XA3, XA4 and XA5), two as received samples (X1 and X2) and three quenched samples (XQ1, XQ2 and XQ3).

A typical test result is reported in Figure 7.1 for X2 sample in “as received” metallurgical microstructure. In particular, the anodic current density (μA/cm²) vs. time (h) graph illustrates the first and second permeations with respective charge transients, partial transients and complete decays. Note that a complete test lasts 200-250 hours (230 hours in the reported example). This graph immediately gives the idea of the time involved in each phase, from the fast partial transients, 1-2 hours, to the long charges, 50-100 hours. In the Figure 7.2 and Figure 7.3 the first complete transient (charge, or polarization 1, partial transient 1 and discharge, or decay 1) and the first partial charge/partial discharge of the same test are drawn, respectively.

In this chapter, anodic current density value is actually the measured total anodic current density minus the passivity current density ($i_p < 100$ nA cm^{-2}) reached during passivation. In the following parts of this chapter the results will be often expressed as i/i_{max} vs. time/L^2 graphs, which means that the current density is divided by the maximum current density reached during its respective permeation history (dimensionless parameter) and the time is divided by the square of the thickness of the sample (not dimensionless parameter). This elaboration was done in order to eliminate the dependence of experimental data on maximum peaks and sample thicknesses.

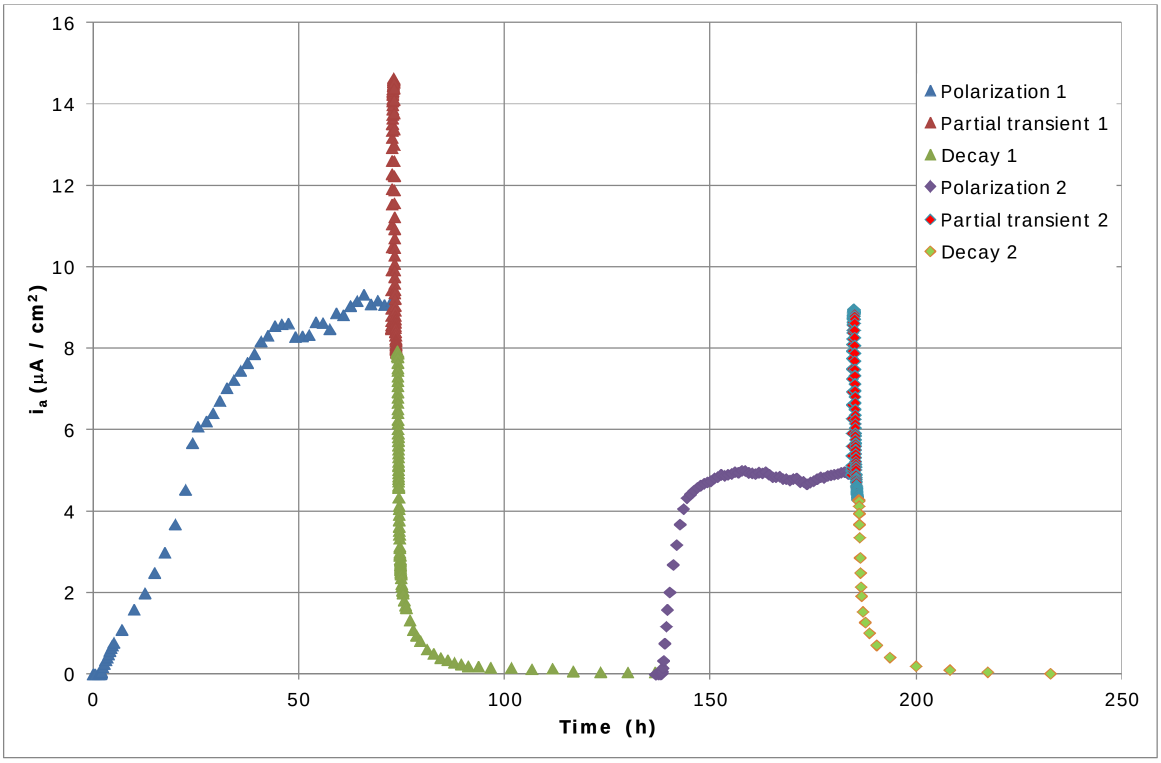

Figure 7.1 - Complete permeation test (as received sample, X2).

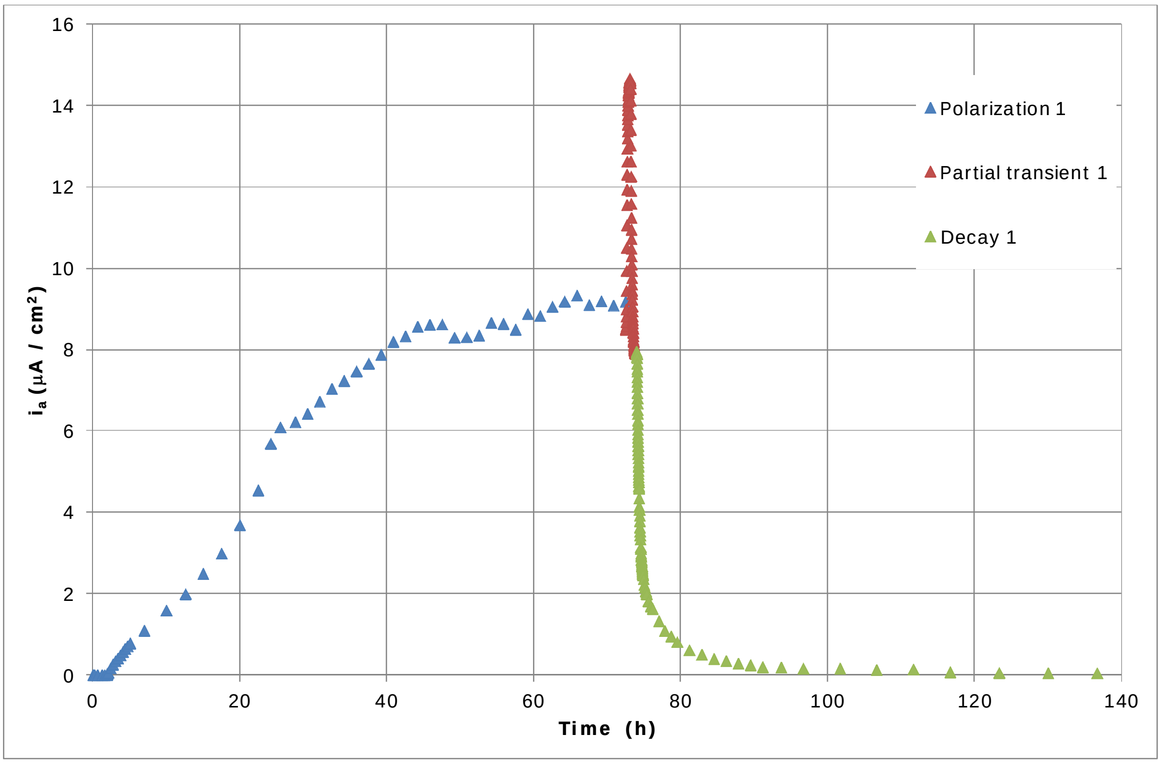

Figure 7.2 - Particular of permeation test: first complete transient (as received sample, X2).

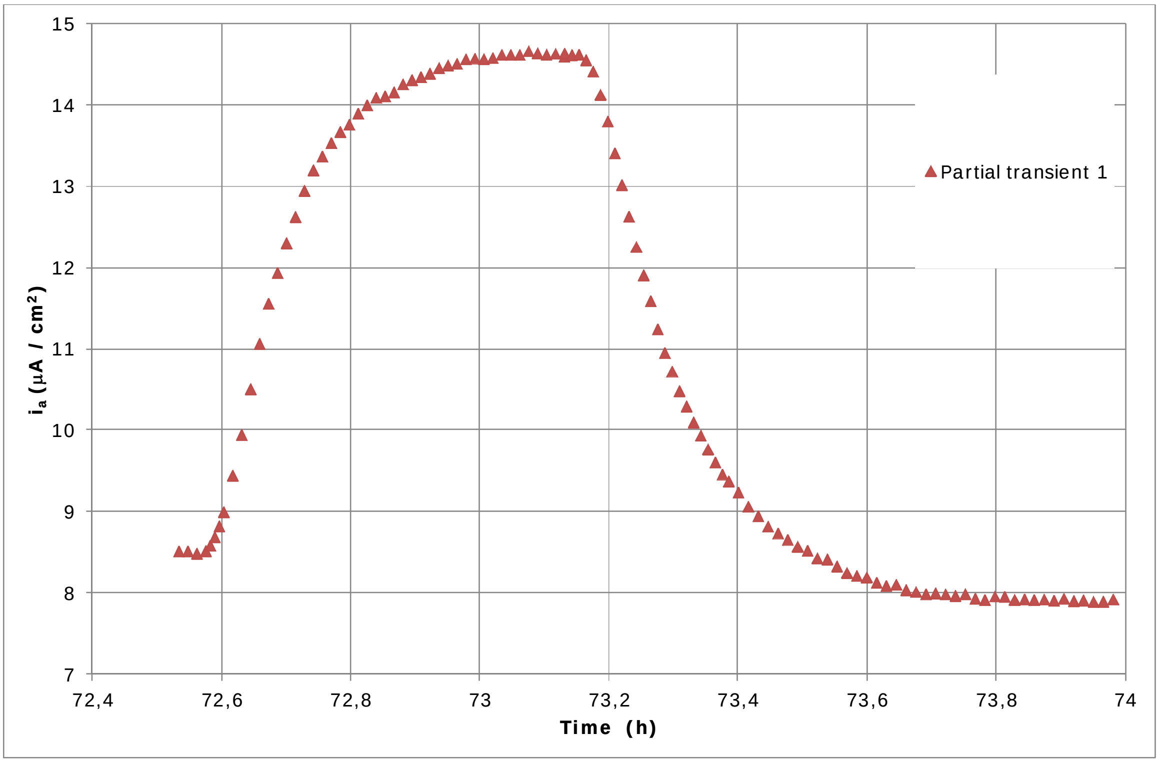

Figure 7.3 - Particular of permeation test: first partial build-up and partial decay (as received sample, X2).

7.2 Charge and discharge

In the following paragraphs the attention is focused on the output of a permeation test as ISO Standard 17081 [21] suggests, i.e. analysis of charge and discharge.

7.2.1 Charge curves analysis

In this paragraph the charge, or polarization, curves (cathodic current density, i_c, variation from 0 to -0.5 mA cm-2) and their representative parameter, i.e. apparent diffusion coefficient D_{app}, are analyzed.

In Figure 7.4, permeation curves during first and second charge are reported for XA (annealed) samples, as an example of this kind of curves. In the graph two extreme theoretical curves (D_{max} and D_{min}), are present, too, which include almost all the experimental data. These latest curves are drawn solving the Fick's second law with these boundary conditions: the initial hydrogen concentration is zero in all the membrane at t=0, for t > 0 cathodic surface concentration is constant while anodic surface concentration is zero (the calculations have been done with Laplace and Fourier equations, as described in the third chapter). Both theoretical curves are calculated with constant diffusion coefficient

(D_{max}= 1.5·10^{-11} m^2 s^{-1} D_{min}=2.5·10^{-12} m^2 s^{-1}, D_{max}/D_{min}=6). In this kind of representation, a lower D value shifts the corresponding curve to the right (longer time) compared to a bigger D value curve.

The graph shows that the first permeation curve of a sample is slightly slower than the second. This is in agreement with Turnbull [22], [23] results for martensitic steel. The author explains this behaviour with the reversible and irreversible trapping model, fully described in Paragraph 6.2.

For the two other microstructures, reported in Figure 7.5 (as received) and Figure 7.6 (quenched), the two extreme theoretical curves and their ratios are:

- as received: D_{max}= 1.7·10^{-11} m^2 s^{-1} D_{min}=3.2·10^{-12} m^2 s^{-1}, D_{max}/D_{min}>5;
- quenched: D_{max}= 2·10^{-11} m^2 s^{-1} D_{min}=7·10^{-12} m^2 s^{-1}, D_{max}/D_{min}>2.5;

These values are at least one order of magnitude lower than lattice diffusion coefficient reported in literature (see the Chapter 4).

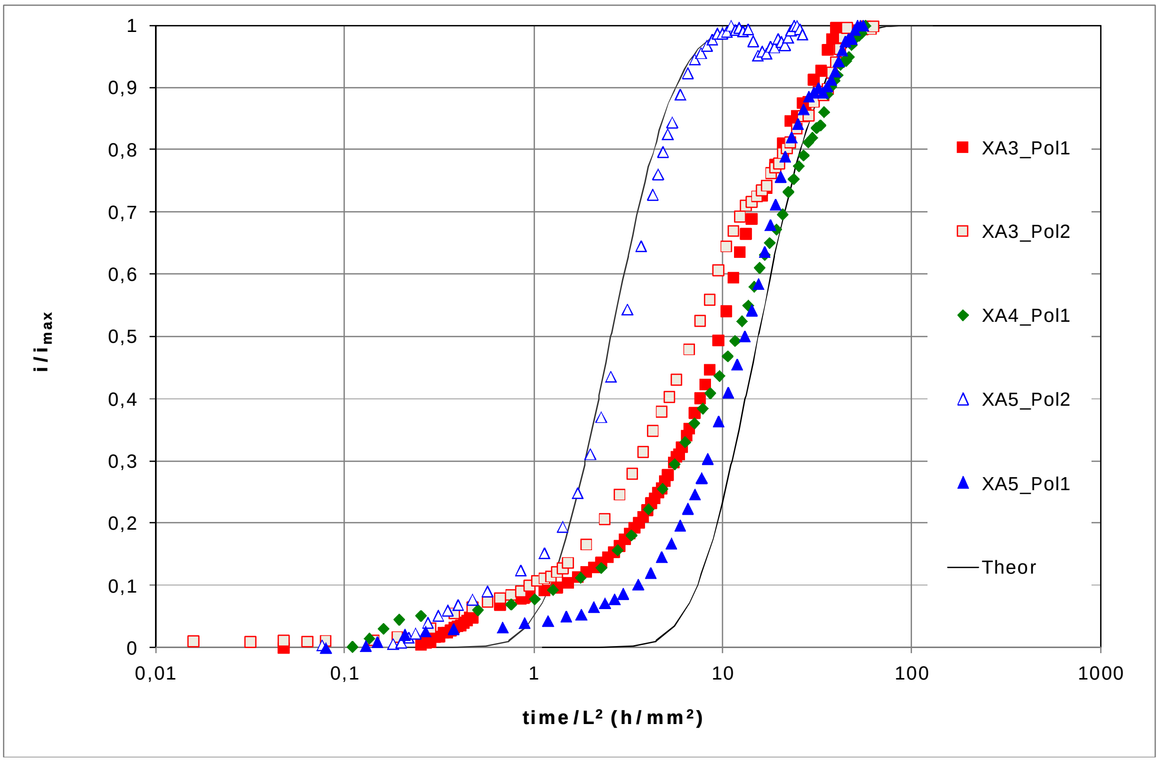

Figure 7.4 - Normalized first and second charge curves behaviour for XA samples.

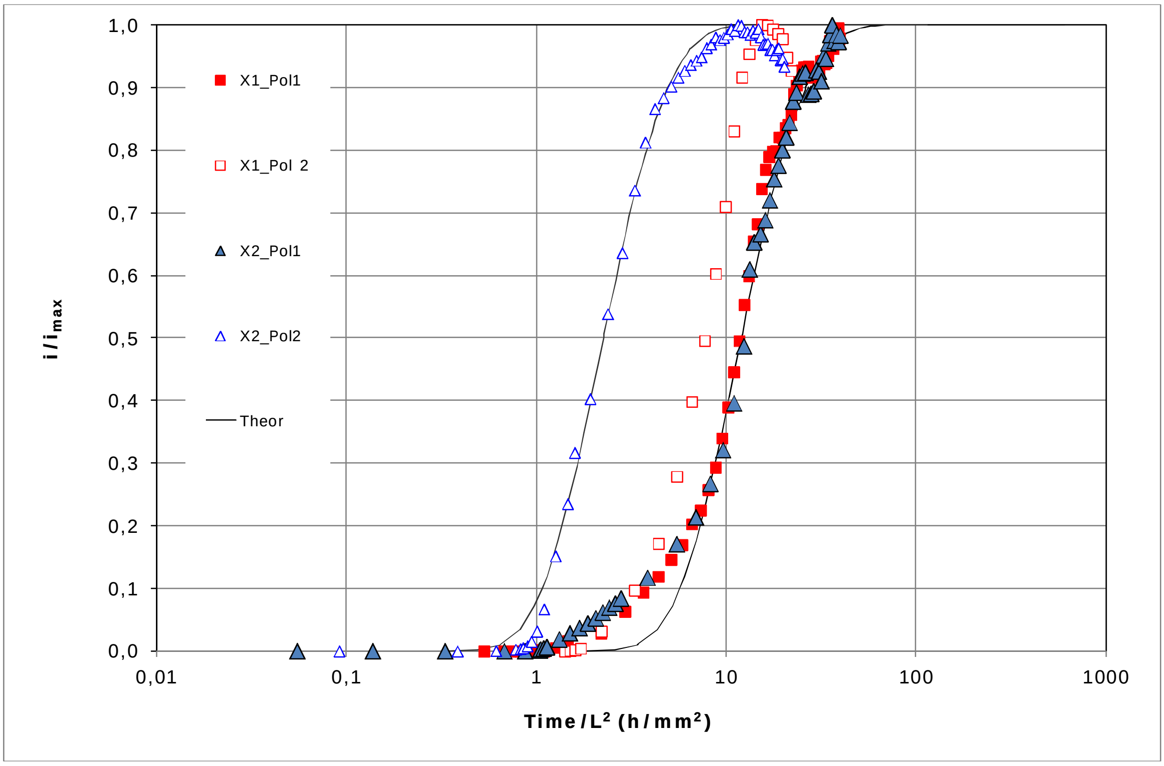

Figure 7.5 - Normalized first and second charge curves behaviour for X samples.

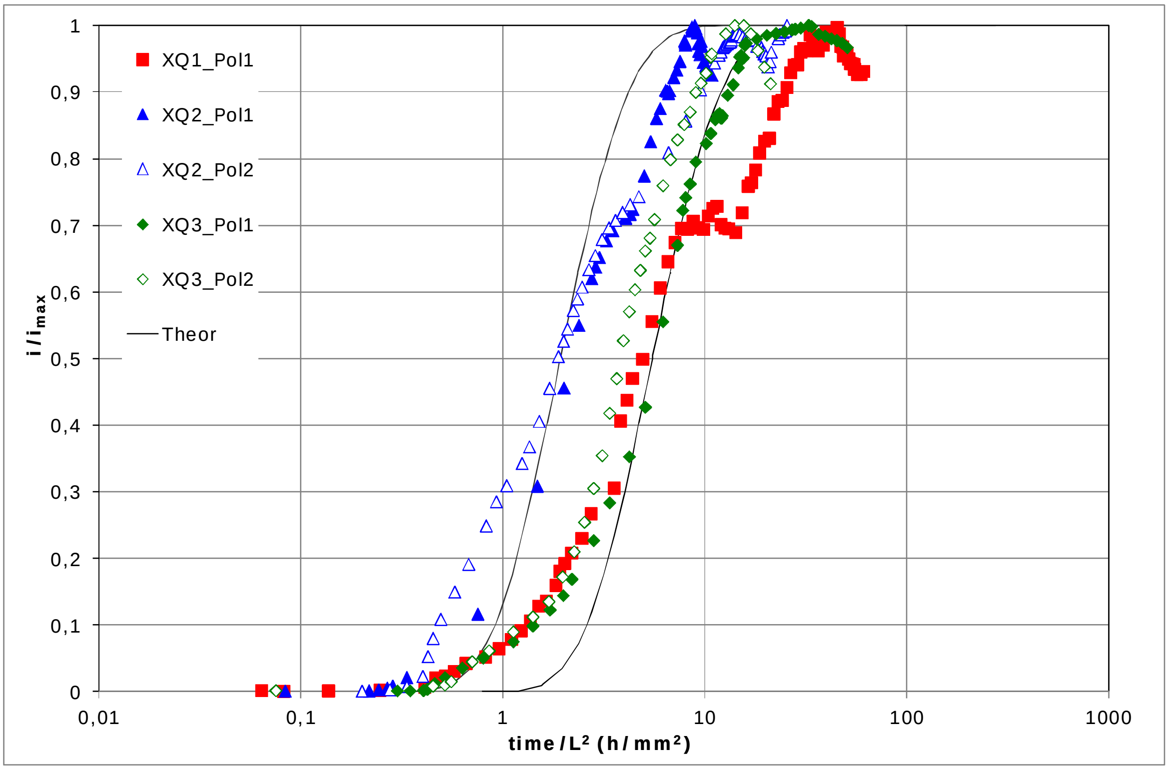

Figure 7.6 - Normalized first and second charge curves behaviour for XQ samples.

The experimental curves in Figure 7.4 do not fit any theoretical curves well. This aspect is evident in the Figure 7.7, where the proper D value in one point of the experimental curve, e.g. best fit between experimental and theoretical curve for i/i_{max} equal to 0.1 (D_{app} 10%), is different from the best fit for i/i_{max} equal to 0.6 (D_{app} 60%). This difference, $D_{1\%}/D_{60\%} > 26$, is very high and suggests that a unique D_{app} does not exist. Other authors obtained similar results [38], [40].

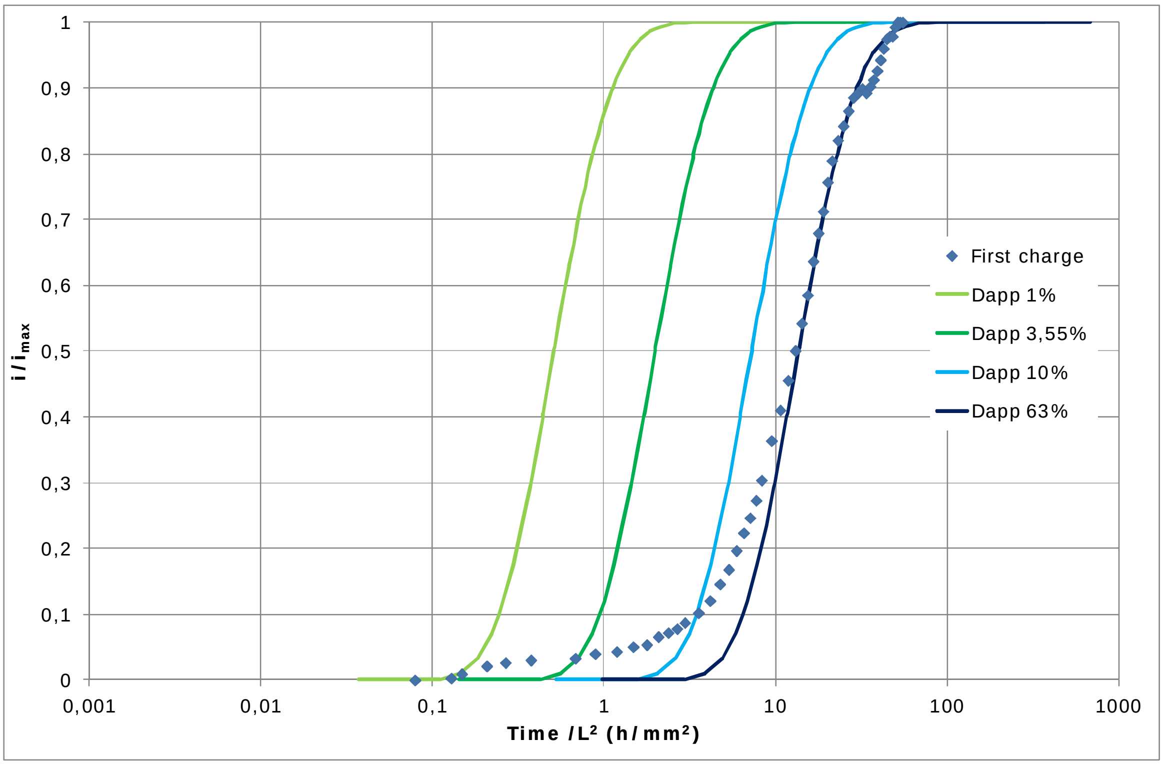

Figure 7.7 - Representation of different best fitting theoretical curves of an experimental curve (XA5-polarization 1).

The histogram reported in Figure 7.8 includes all the D_{app} values for the tested annealed samples, while in Figure 7.9 and Figure 7.10 are reported the results for as received and quenched sample, respectively. It confirms the previous consideration concerning the dispersion of the D_{app} value for the single sample, but it also gives other information: there is almost always a decreasing trend in the apparent diffusion coefficient, with the highest values for $D_{1\%}$ and the lowest values for $D_{60\%}$, which suggests that some processes participate to slow down the hydrogen permeation rate during the tests. This trend has been observed almost every time even for the other microstructures. It may be due to cathodic surface changing condition during time or to reversible and irreversible trapping.

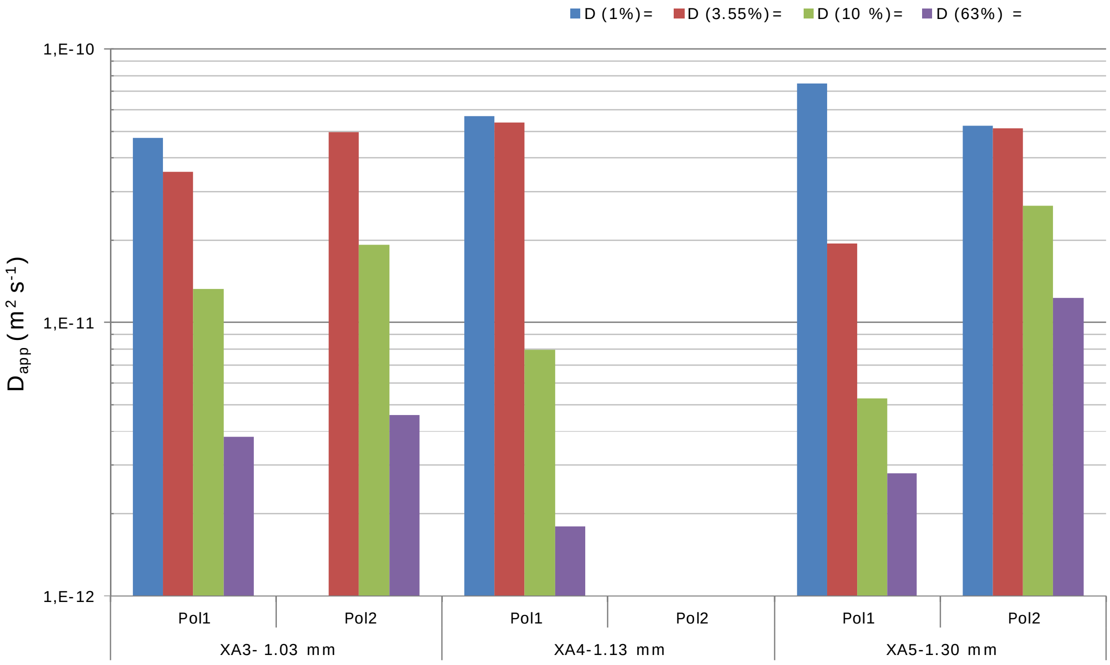

Figure 7.8 - Various D_{app} values histogram of XA samples during first and second charge.

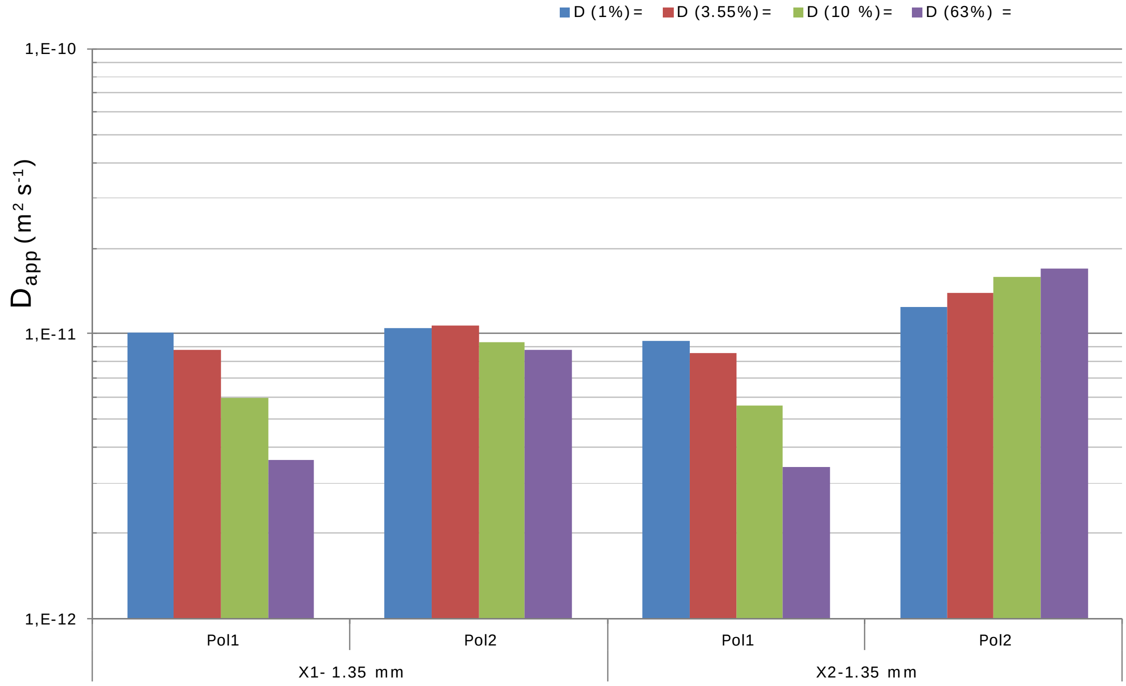

Figure 7.9 - Various D_{app} values histogram of X samples during first and second charge.

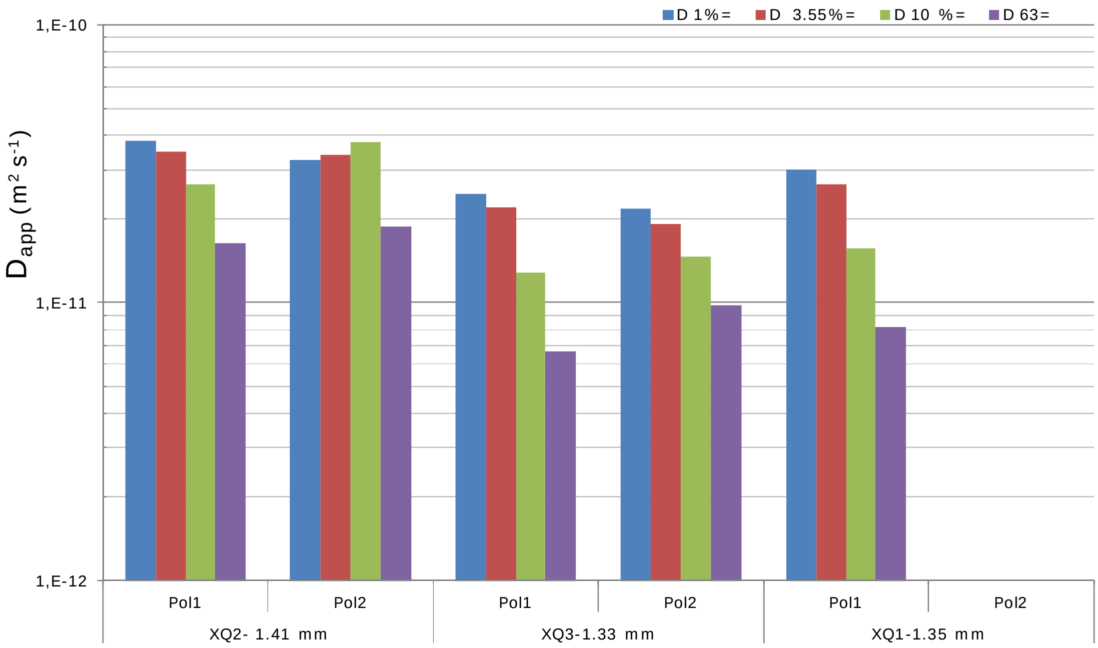

Figure 7.10 - Various D_{app} values histogram of XQ samples during first and second charge.

7.2.2 Discharge curves analysis

The discharge phase, or desorption, of the adsorbed hydrogen into the membrane (switch-off of the cathodic galvanostat, i.e. i_c variation from -0.5 mA cm^{-2} to 0) of the same annealed tests seen in Paragraph 7.2.1 are shown in Figure 7.11. The same graph for the other two microstructures is in Figure 7.12 and Figure 7.13. As in the charge, the whole curves do not fit the theoretical Fick's law but now it is possible to observe a new aspect. According to Zakroczymski [58], [59] (Paragraph 5.4) and Frappart [36], in the initial part of the curve (roughly in the range $1 \geq i/i_{max} > 0.9$) desorption of the diffusible hydrogen prevails while the hydrogen derived from traps become perceptible after some seconds. After few minutes diffusible hydrogen is almost over and the anodic current measures the rate of hydrogen release from reversible traps. The difference between the experimental desorption curve and the theoretical one drawn in order to fit the first part gives a measure of the reversible trapped hydrogen released from the anodic surface.

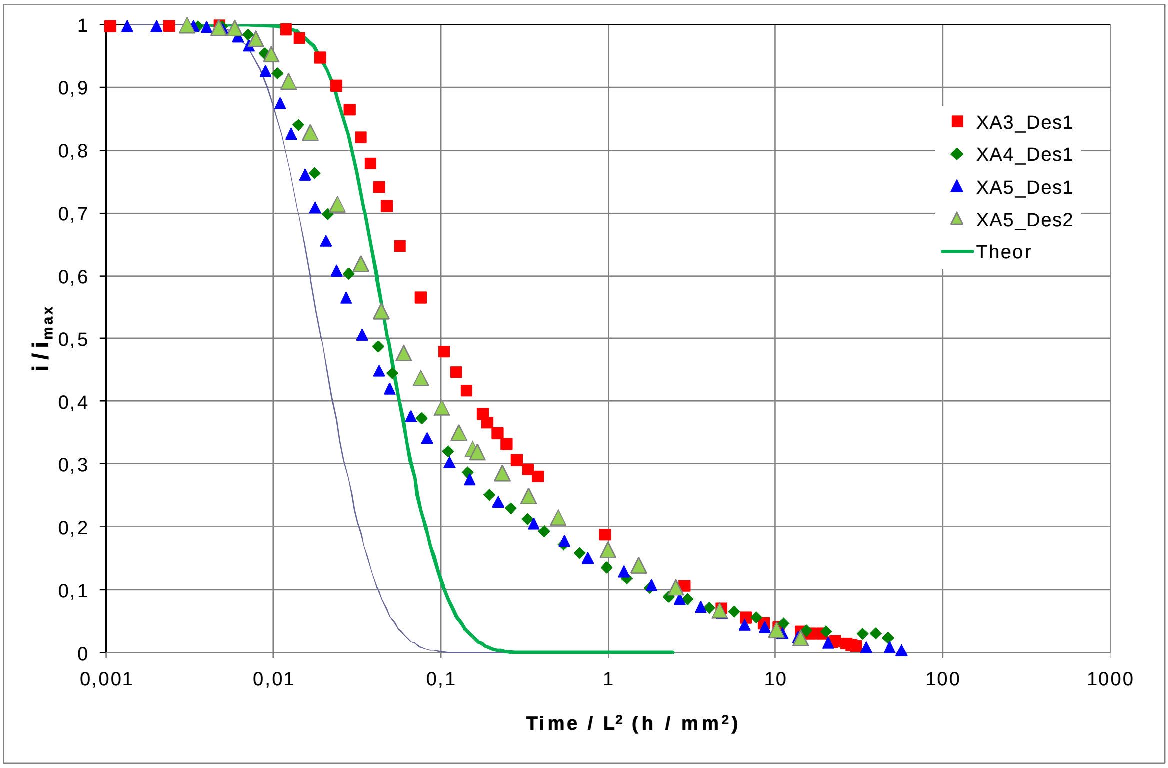

Figure 7.11 - Normalized first and second discharge curves behaviour for XA samples.

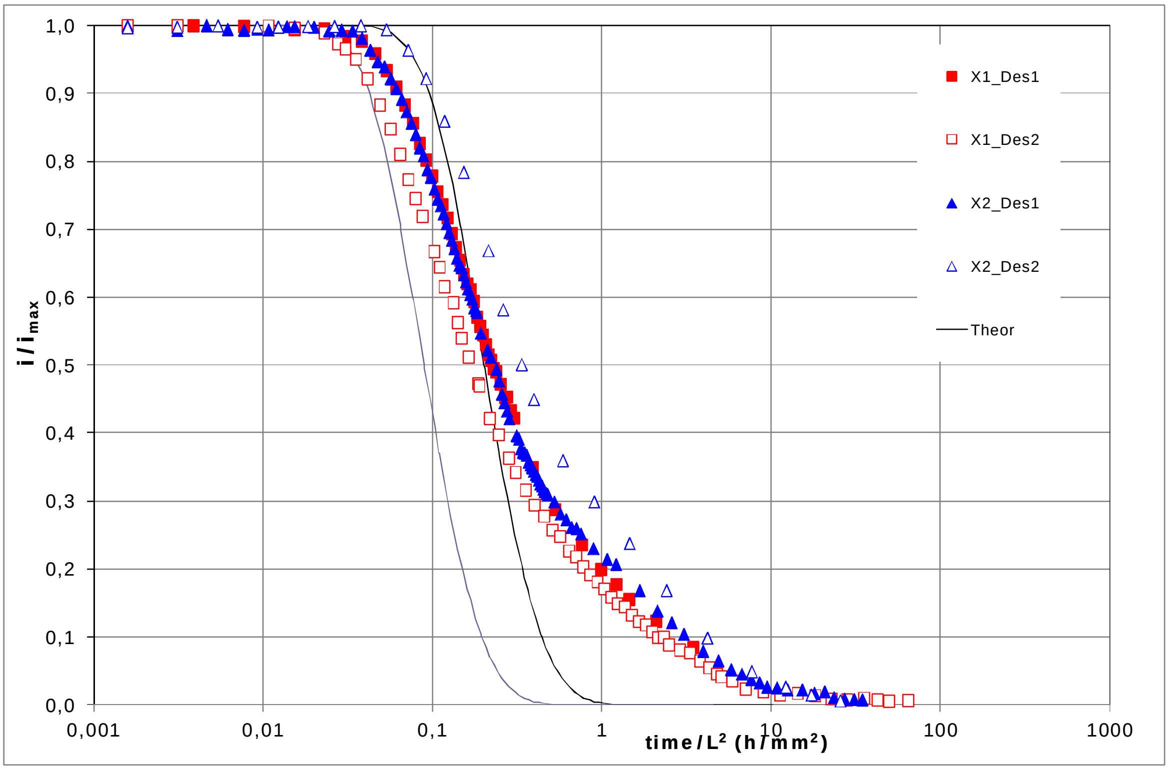

Figure 7.12 - Normalized first and second discharge curves behaviour for X samples.

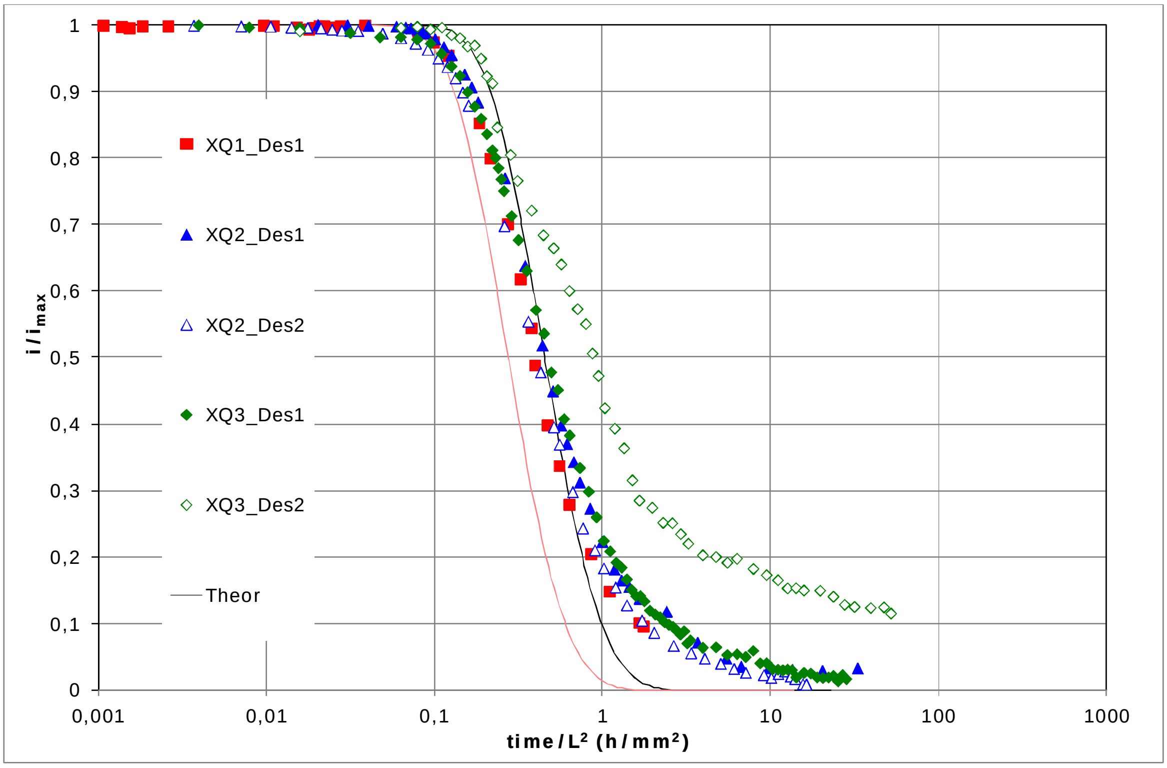

Figure 7.13 - Normalized first and second discharge curves behaviour for XQ samples.

7.2.3 Charge-discharge comparison

In order to compare the charge experimental curves with the discharge ones, Figure 7.14 sums up the data of Figure 7.4 and Figure 7.11. It is clear how charge and discharge are different. The curves of the same polarization for the same sample, e.g. first polarization and first desorption of XA3, never cross at i/i_{max}=0.5, as theoretically predicted by Fick’s laws, but on the contrary they usually meet around 0.15 (yellow circle) and they are not symmetrical. The comparing graphs for the as received and quenched tests are reported in Figure 7.15 and Figure 7.16.

In Figure 7.19, Figure 7.20 and Figure 7.21 included in Paragraph 7.3, the same kind of graphs will be replicated for partial charge-discharge, so it will be possible to compare the graphs and appreciate the relevance of each one.

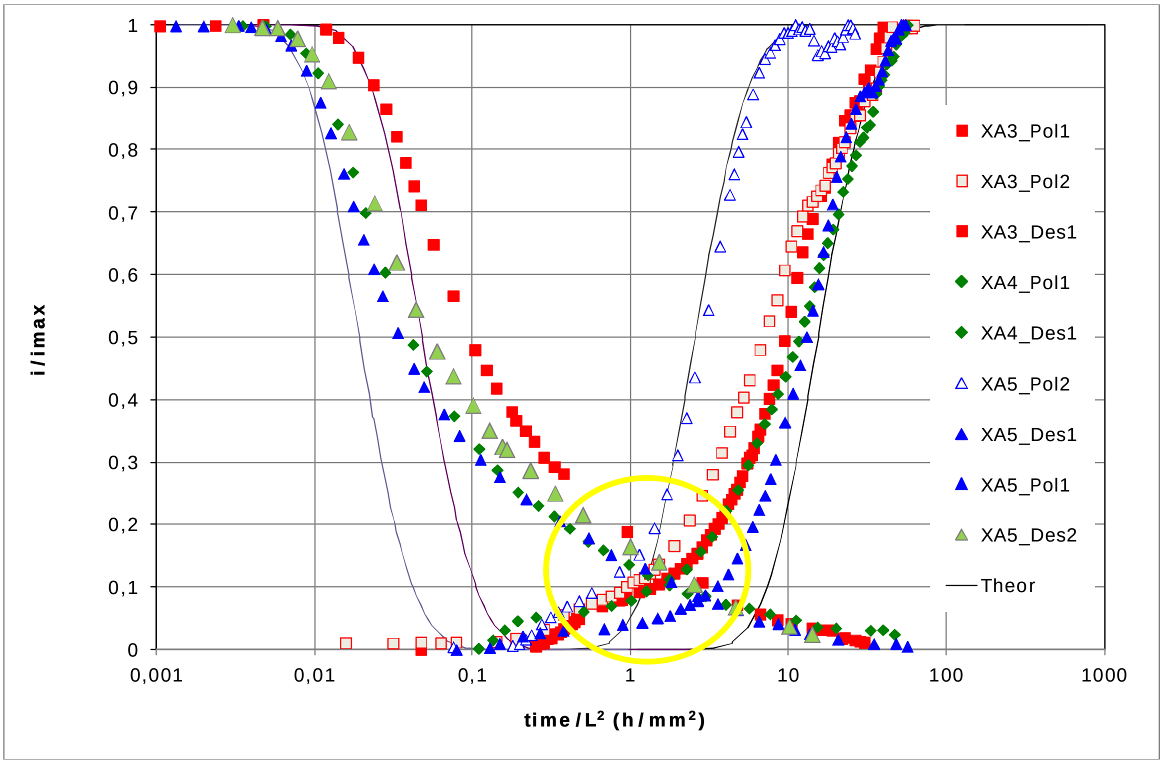

Figure 7.14 - Normalized first and second charge-discharge curves behaviour for XA samples.

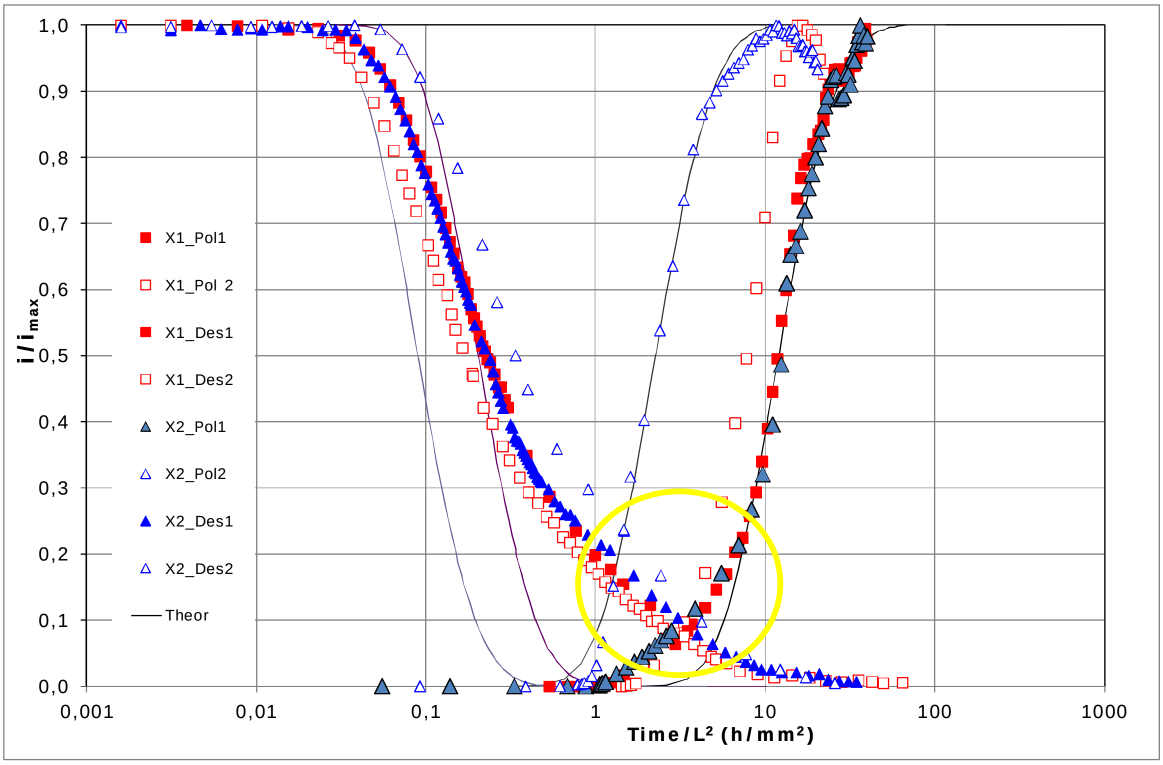

Figure 7.15 - Normalized first and second charge-discharge curves behaviour for X samples.

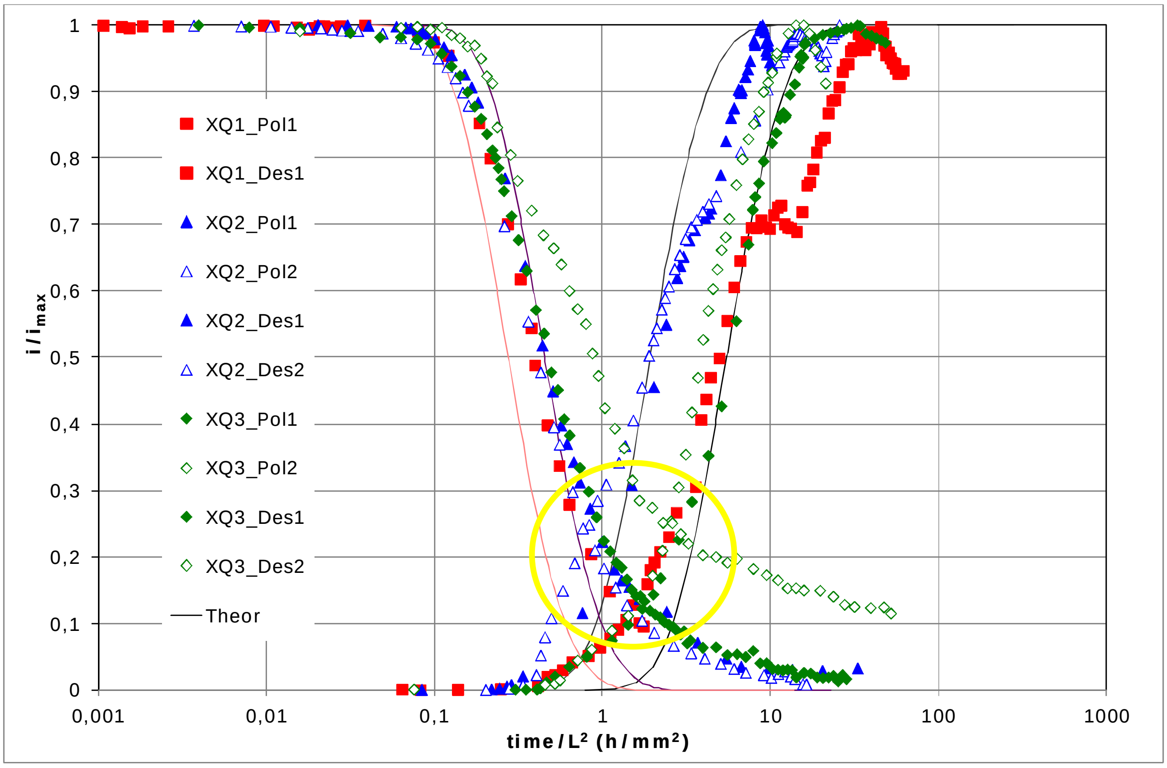

Figure 7.16 - Normalized first and second charge-discharge curves behaviour for XQ samples.

As the last consideration about these aspects, in Figure 7.17 the difference between the theoretical charge curve with D_L value (the same of the theoretical decay curve found in 1-0.9 best fit zone of the experimental decay) and the experimental charge curve for XA5 sample is shown. These two curves are separated by more than two orders of magnitude, which gives an idea about how the physical phenomena which act behind this behaviour are different. D_L values for each complete discharge made during this project have been grouped. The minimum and maximum values of D_L obtained by this method, for each microstructure, are reported in Figure 7.23 and *Des Min* and *Des Max*, respectively, compared with partial charge and partial discharge procedure results.

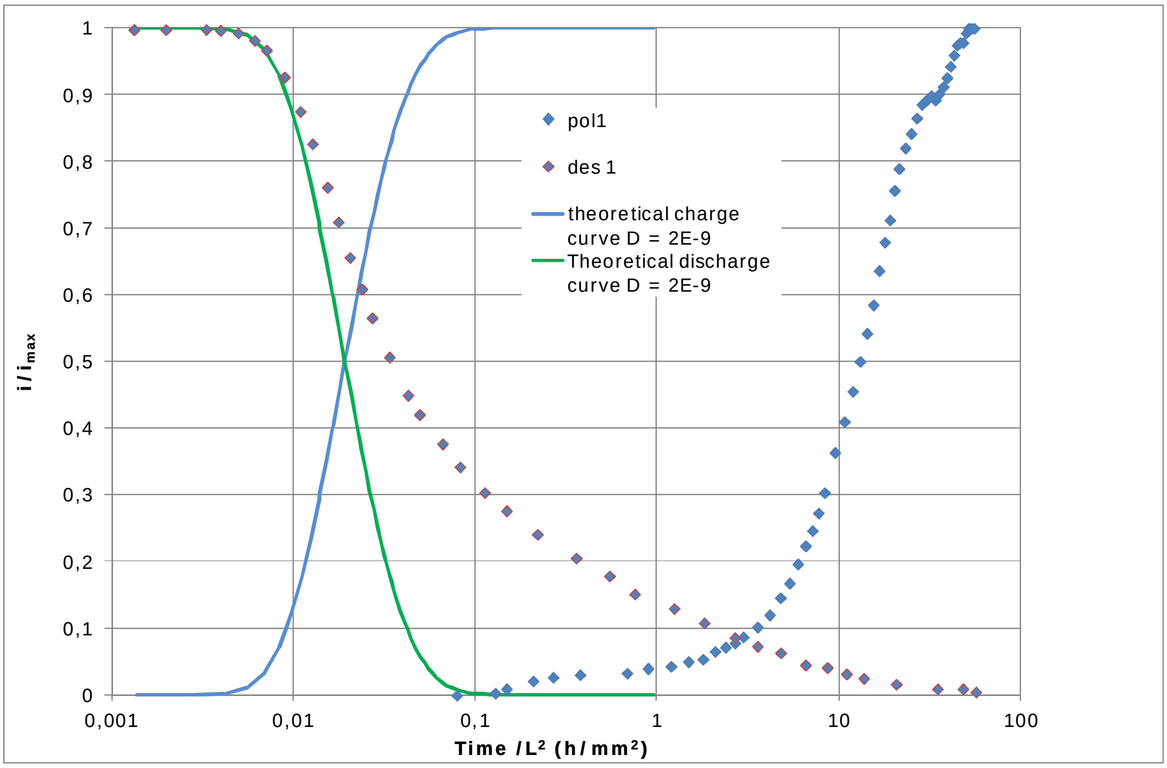

Figure 7.17 - Differences between theoretical curves with D_L diffusion coefficient form desorption and experimental charge-discharge.

7.2.4 Cathodic potentials during charge

In Figure 7.18 all the cathodic potentials measured during the first and second charge, or polarization, are reported. This graph shows that after switching on the galvanostat, the potential starts decreasing. Only after tens of hours the cathodic potentials become stable. This trend was observed by other authors [39], [49], [56]. The stability of potential is very important for permeation test because it is the indicator of electrochemical condition of the cathodic surface, which must be stable in order to get reliable results. Another remarkable fact is that even if the single potential curve reaches the stability, there is not a common stable potential value among different tests (or among different microstructures). Indeed the values are dispersed in ≈0.2 V band (black lines).

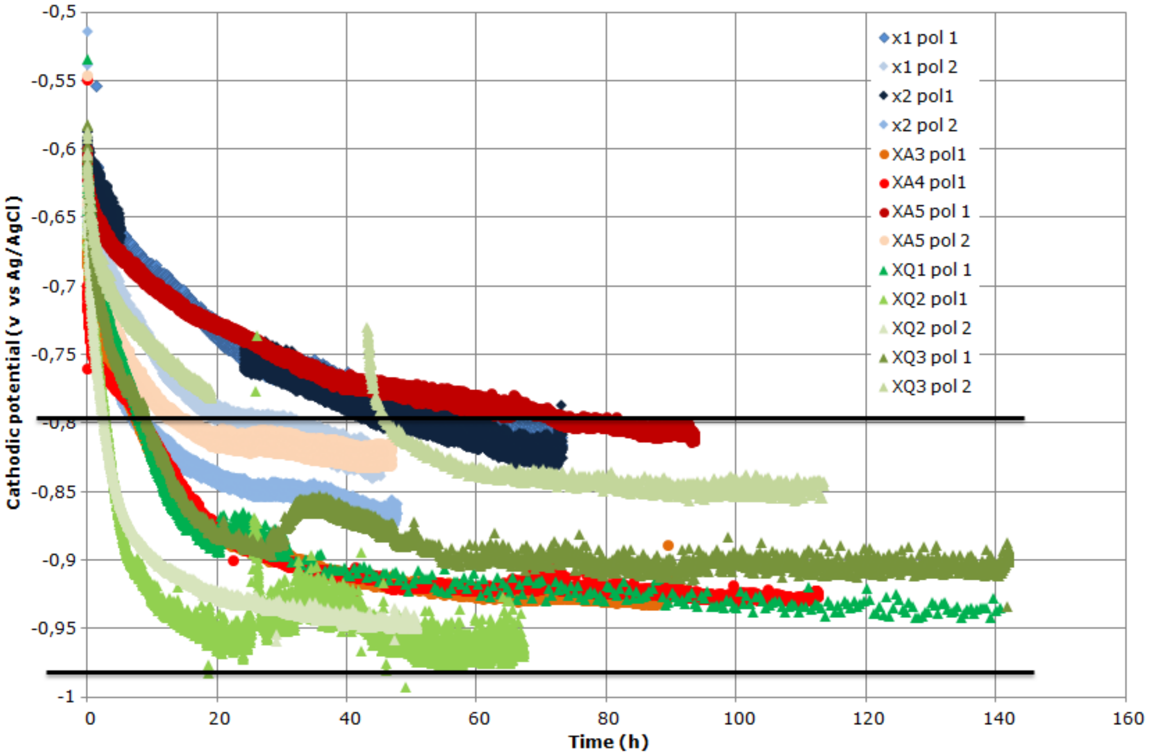

Figure 7.18 - Cathodic potentials for all the samples (relative to 1st and 2nd charge) with black lines to mark the range.

7.3 Partial charge and partial discharge

In order to get over the problems in measuring a correct and reproducible diffusion coefficient, as explained in the previous paragraphs, the Zakroczymski's hydrogen permeation procedure [58], [59], [60] has been adopted, i.e. partial charge and partial discharge analysis (see Paragraph 5.3) has been applied after a long enough stabilization time.

In Figure 7.19 are reported the results of the partial charge (i_c from -0.5 to -1 mA cm^{-2}) and the partial discharge (i_c from -1 to -0.5 mA cm^{-2}) tests on as received samples, i.e. X1 and X2, are reported. These tests are plotted with the usual time / L^2 on x-axis and $\Delta i/\Delta i_{max}$ on y-axis, with Δi equal to anodic current density minus quasi stationary anodic current density values reached during the previous charge. Some relevant considerations can be done by examining this figure:

- every partial charge and discharge curve follows the theoretical curves very well as far as their entire length;
- in each sample (both polarizations), the two experimental curves cross almost perfectly at the theoretical value $\Delta i/\Delta i_{max}$=0.5. Consequently the diffusion

coefficient of every couple of curves is about the same, which means that there is a high intrinsic reproducibility on the same specimen;

- diffusion coefficient values among different specimens are between $D_{min}= 3.5\cdot10^{-10}$ $m^2\ s^{-1}$ and $D_{max}= 6.3\cdot10^{-10}$ $m^2\ s^{-1}$ ($D_{max}/D_{min}<2$), so they show reduced dispersion.

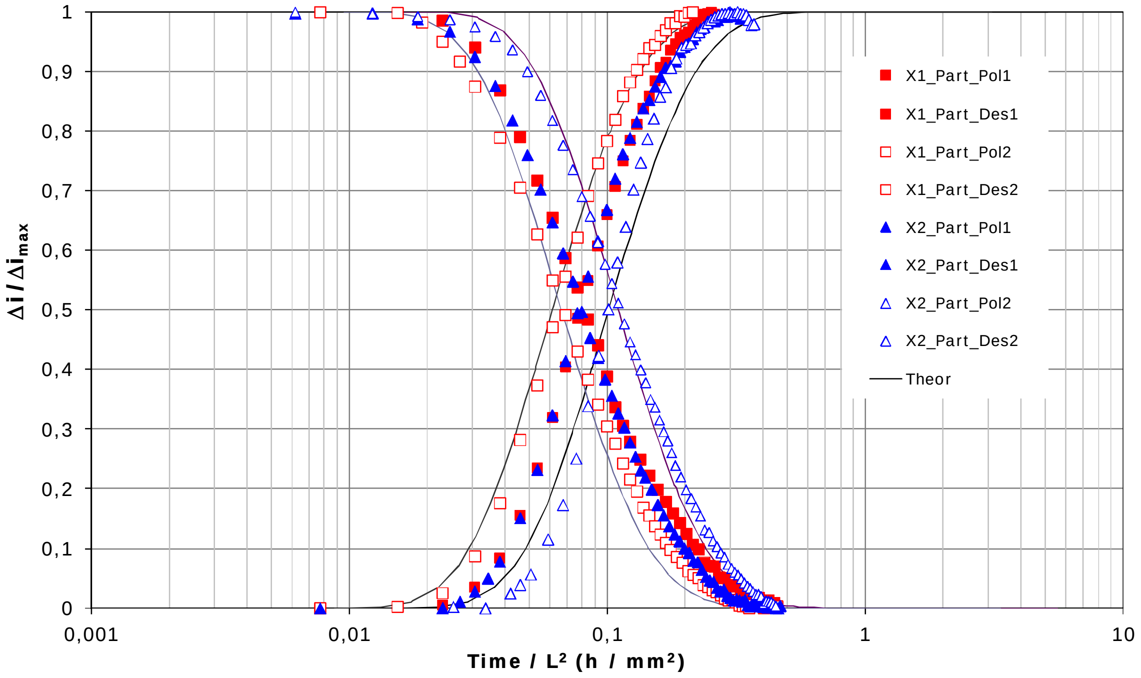

Figure 7.19 - First and second partial charging-partial discharging curves for X1 and X2 samples.

The same considerations are fully valid for annealed and quenched tests (Figure 7.20 and Figure 7.21) and the D values ranges for these two microstructures are:

- annealed: $D_{max}= 3.3\cdot10^{-9}$ $m^2\ s^{-1}$ $D_{min}=1.2\cdot10^{-9}$ $m^2\ s^{-1}$, $D_{max}/D_{min}<3$

- quenched: $D_{max}= 1.8\cdot10^{-10}$ $m^2\ s^{-1}$ $D_{min}=1.1\cdot10^{-10}$ $m^2\ s^{-1}$, $D_{max}/D_{min}<2$

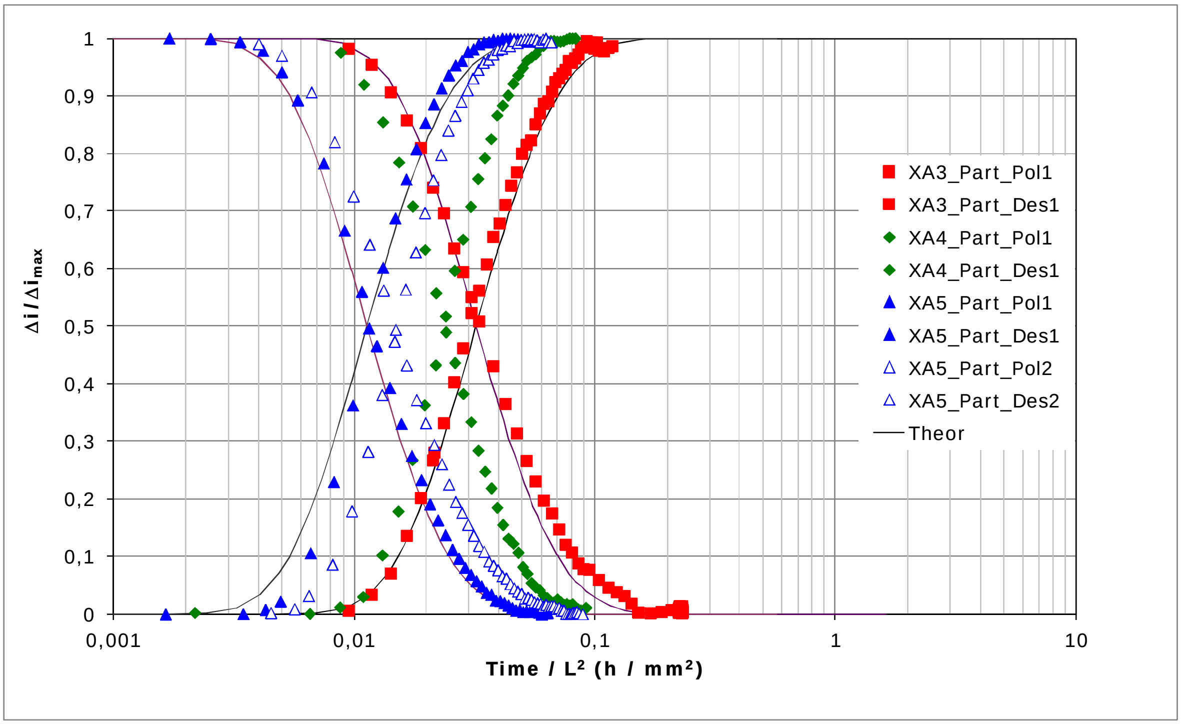

Figure 7.20 - First and second partial charging-partial discharging curves for XA3, XA4 and XA5 samples.

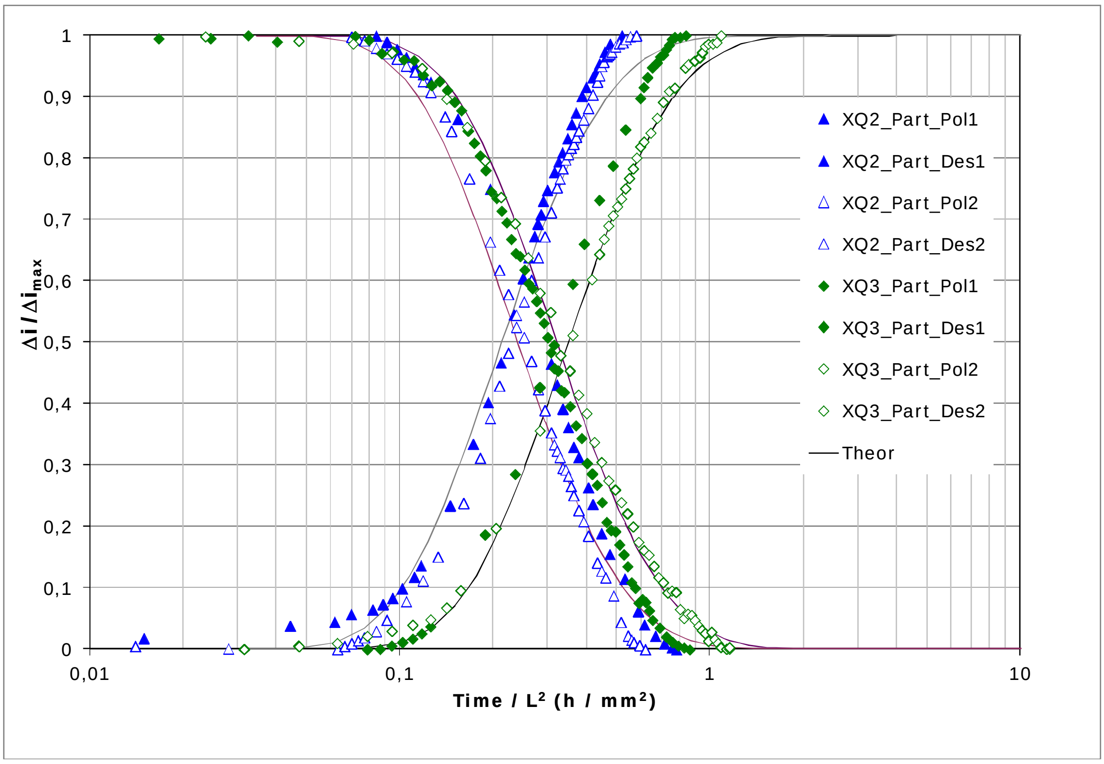

Figure 7.21 - First and second partial charging-partial discharging curves for XQ1, XQ2 and XQ3 samples.

7.3.1 Cathodic potential during partial transients

In Figure 7.22 the potential evolution during partial charge and partial discharge is plotted, with time=0 immediately after the cathodic current change. In particular, one representative curve for each microstructure is present. Some comments can be done: the surface needs very few seconds to respond to the initial changed current (see the decreasing points immediately after time=0), then it maintains constant values. Only the quenched sample shows a little oscillation in a close range. Then, when the partial discharge starts, again the new stable value is reached almost immediately by every test. This immediate changing of potential values and the stable electrochemical surface condition confirms that the procedure proposed by Zakroczymski and here adopted guarantees the constancy of the hydrogen fugacity on the cathodic side during the adsorption/desorption transients, which is fundamental for a correct diffusion coefficient measurement using the Devanathan and Stachurski method.

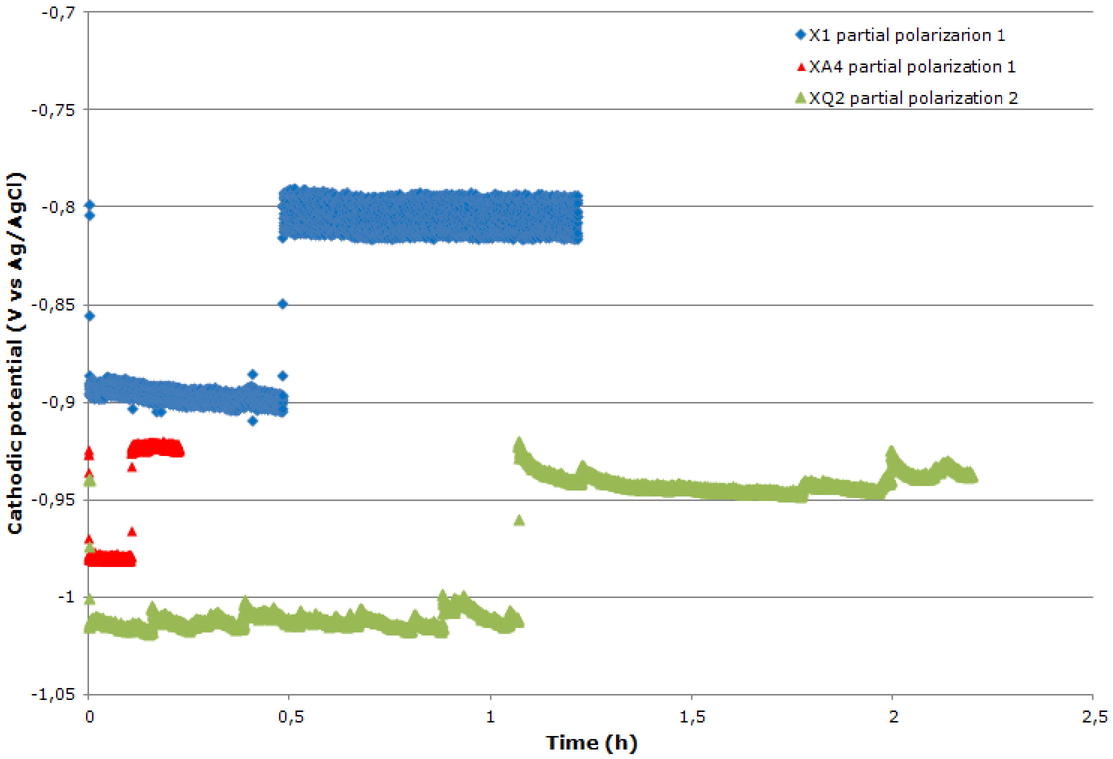

Figure 7.22 - Cathodic potential registered during partial charge and partial discharge for one sample for each microstructure.

7.4 Microstructural effects

In order to point out how the microstructure alters the hydrogen permeation behaviour the diffusion coefficient values obtained by the following methods have been compared:

- apparent diffusion coefficient, D_{app}, of complete charge/discharge method, according ISO 17081;
- lattice diffusion coefficient, D_L, of partial charge/partial discharge method;
- lattice diffusion coefficient, D_L, of desorption method (1 - 0.9 best fit region of experimental curves).

In Figure 7.23 a summarizing histogram is reported. In this histogram the maximum and minimum diffusion coefficient values measured in the different tests for the examined microstructures are reported. The following considerations can be done:

1. ISO 17081 method is the most scattered and it does not point out perceptible differences among the three microstructures;
2. other methods clearly show three bands of values in a reproducible way;
3. looking at partials method, the average value of D_L in martensitic microstructure is about 3 times lower than the bainitic one and about 14 times lower than annealed one;
4. the D_L found with desorption method shows minimum and maximum values slightly lower than D_L from partial method.

The last consideration makes you think that this method may be little affected by trapping phenomenon, which gives lower values of D as a consequence. The origin of this aspect should be ascribed to the determination of D_L: the best fit method of initial part of the desorption is quite arbitrary, e.g. where the best fit can be stopped, so some imperfections might alter this method. In Zakroczymski's method subjective choices like the one previously shown are not present. However the quality and the reproducibility of desorption results is good and similar to partials D_L.

The D_L values found with the partials methods is exclusively a lattice parameter, no trapping phenomena are involved. Therefore the differences among these values (point 3 above) are only due to the lattice differences. In particular, the transition from bcc lattice of annealed and Q&T to bct one of martensite, an increase of the fineness of the grains, the grain boundaries and/or the dislocation density lead to lower lattice diffusion coefficients.

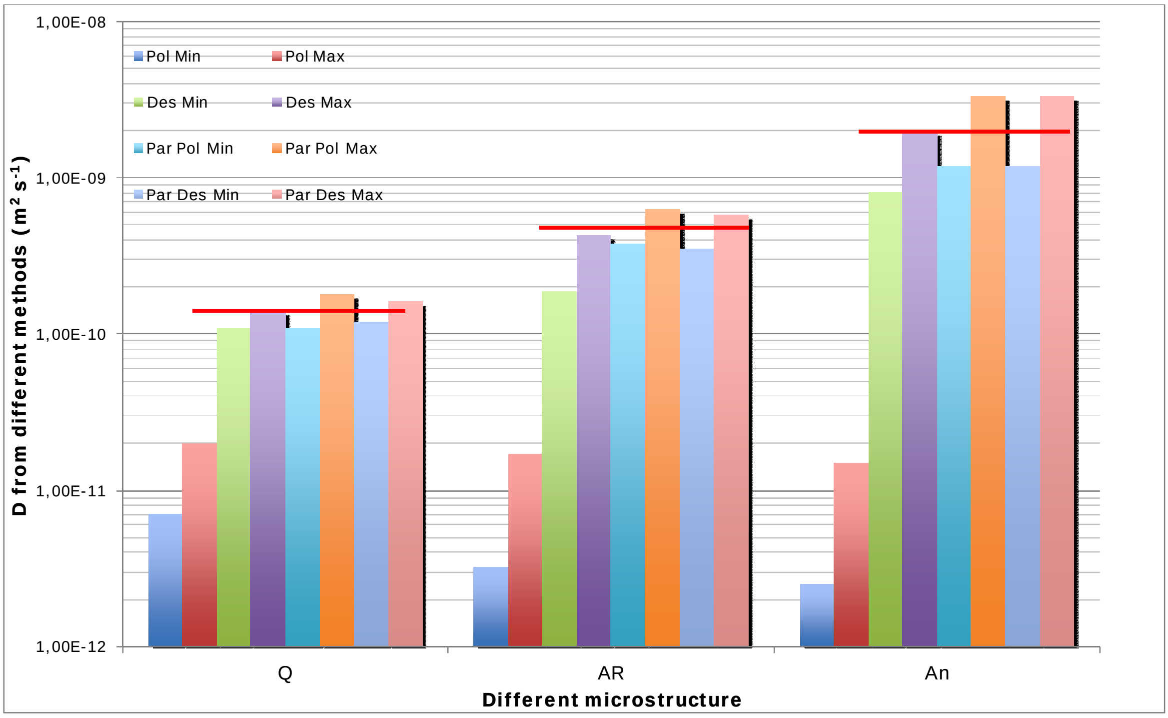

Figure 7.23 - Different diffusion coefficients summarizing histogram.

In Figure 7.24 all the partial transients are plotted, in order to appreciate the sensitivity of partial charge-discharge method with different microstructures. These permeation curves are distinctly grouped in bands.

In Figure 7.25 all samples are listed in a histogram with D_L calculated with the usual methods on y-axis. This histogram allows to separate the contribution to the scattering on the measured values of D_L due to different specimens and the one due to different measuring method.

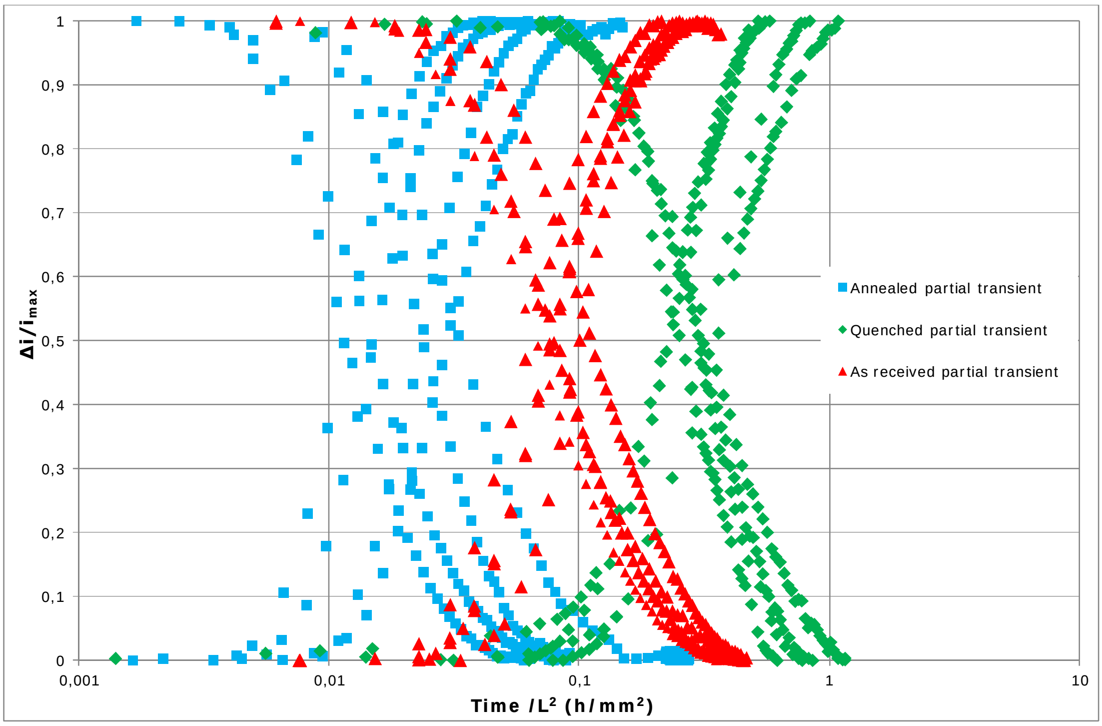

Figure 7.24 - Partial charge and partial discharge for all the specimens, first and second polarization.

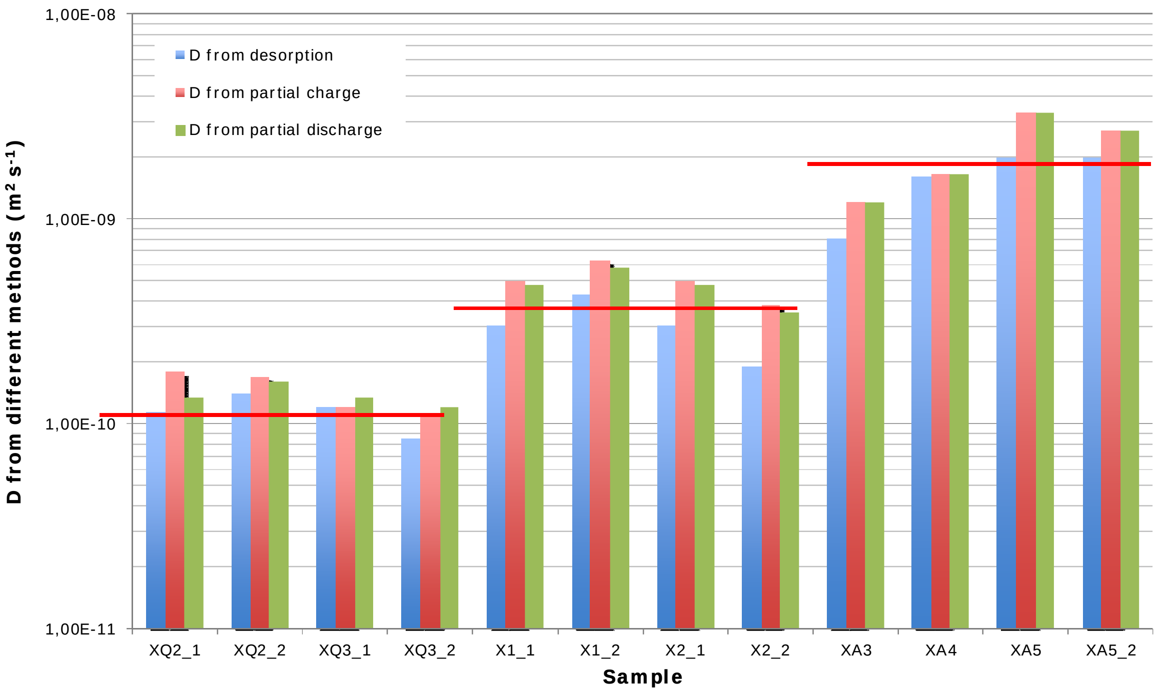

Figure 7.25 - Histogram concerning lattice diffusion coefficients from two different methods for every sample.

7.5 Reversibly trapped and lattice hydrogen release

Starting from Zakroczymski's work described in Paragraph 5.3, the comparison between the theoretical desorption curve with D_L and experimental discharge curve leads to estimate the amount of total, lattice and trapped hydrogen. The result of this calculation (in ppm), based on numerical integration of experimental desorption curves, is reported in Figure 7.26, regarding the total amount of hydrogen (lattice + reversible trapped) escaped from the anode, Figure 7.27, regarding only the reversibly trapped hydrogen which goes out from the anode, and Figure 7.28, regarding the theoretical desorption-experimental discharge ratio. All these results have been organized in ascending order for each microstructure.

Annealed samples show an average better capability to store hydrogen than the other two microstructures, followed by as received material which stores slightly more than quenched samples (Figure 7.26). Similar trend is observed for the reversibly trapped hydrogen, i.e. the hydrogen which is released after an initial phase of lattice releasing (Figure 7.27). In Figure 7.28 the ratio calculated emphasizes how the microstructures can modify the hydrogen permeation and its accumulation in different quantities and proportions. The average ratios for different microstructures are clearly distinct, with values in the following order: Average Quenched > Average As Received > Average Annealed.

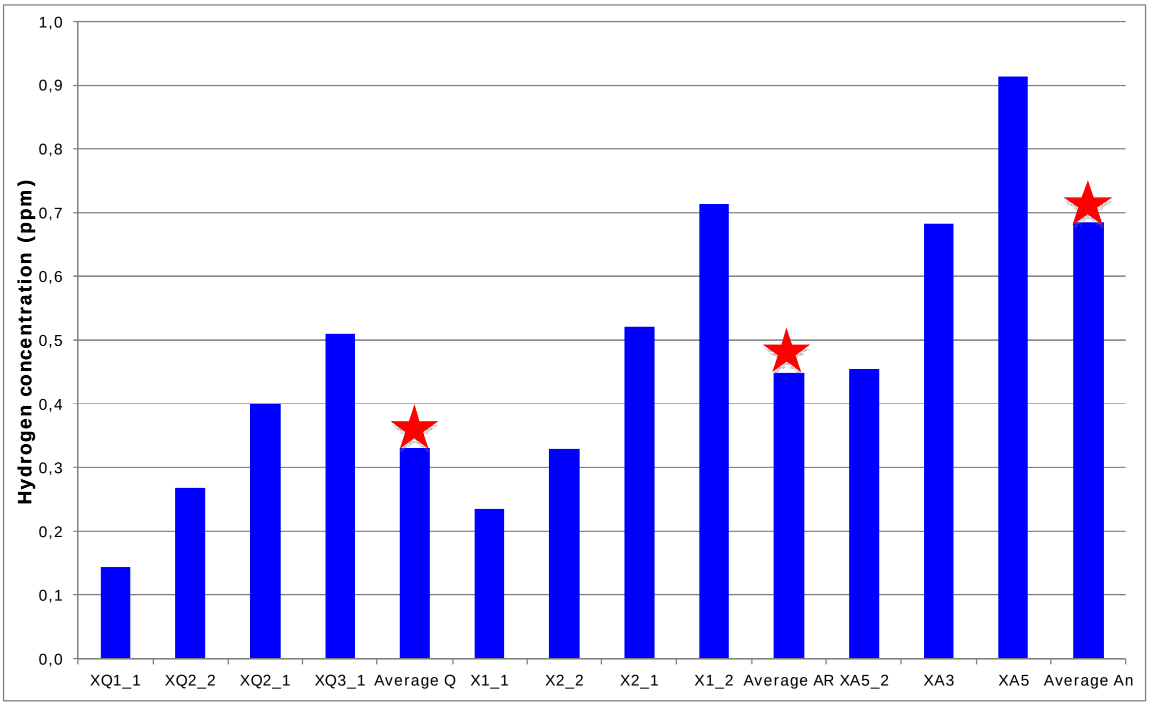

Figure 7.26- Histogram concerning the total amount of hydrogen for each sample (from the area below the experimental curve).

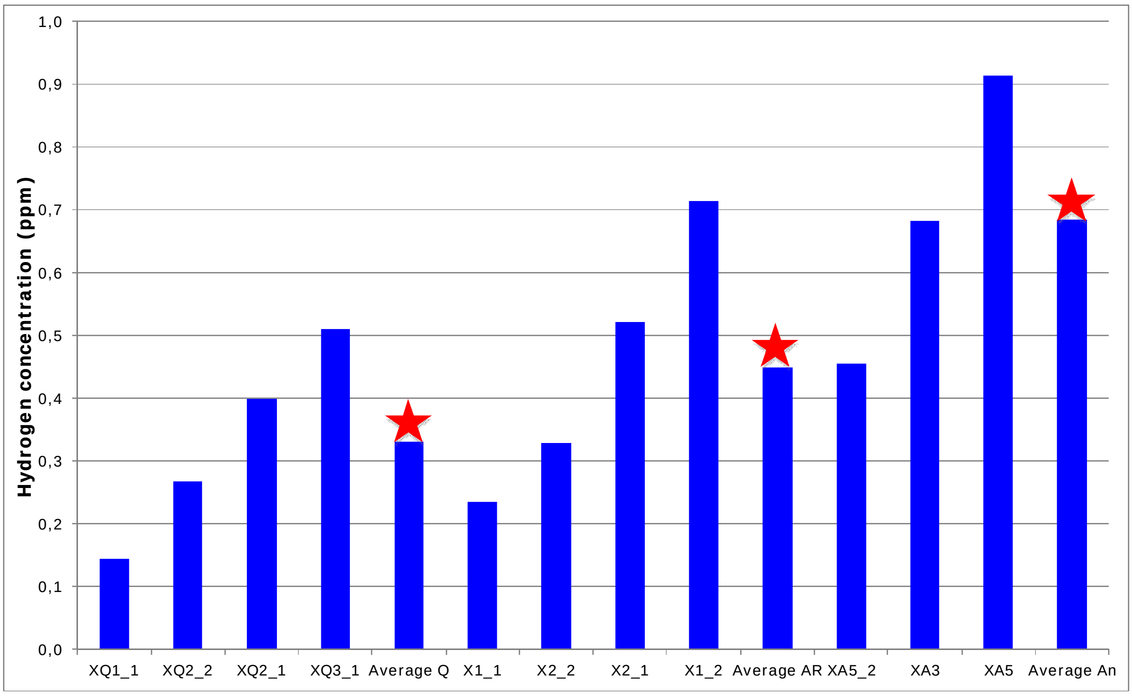

Figure 7.27 - Histogram concerning the reversibly trapped hydrogen for each sample (from experimental curve area minus theoretical curve area).

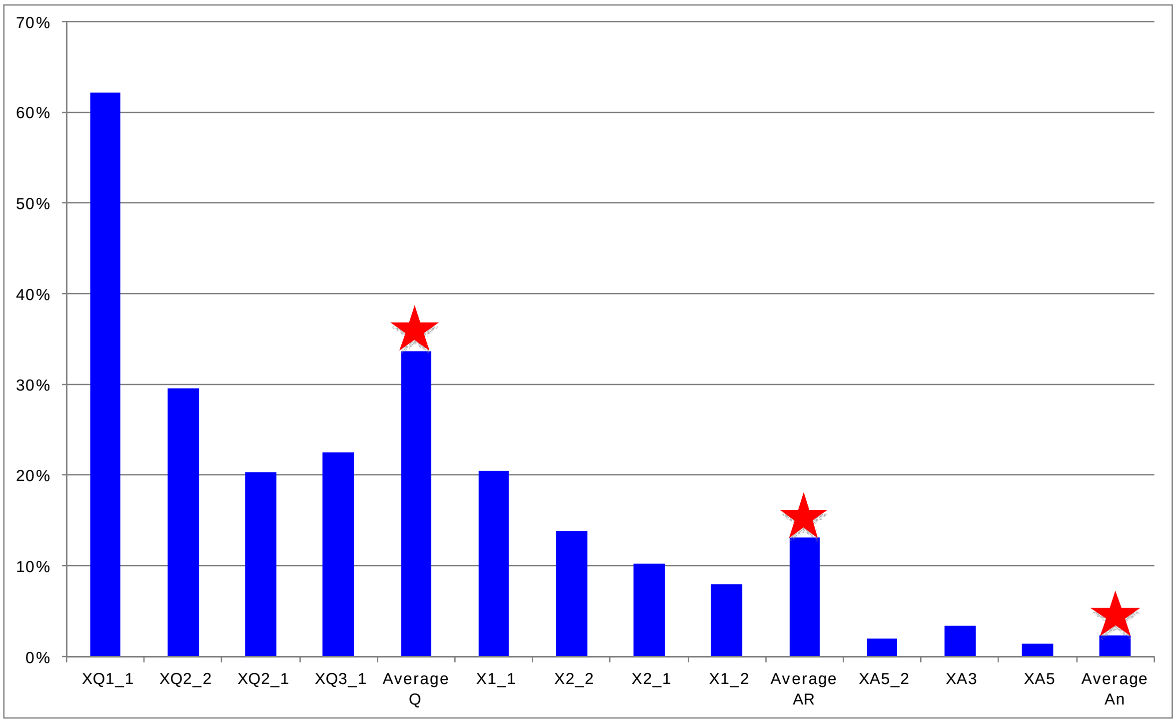

Figure 7.28 - Histogram representing the area below the theoretical curve divided the area below the experimental curve.

CONCLUSIONS

This thesis has investigated the hydrogen diffusion and trapping processes into API 5L X65 pipeline steel with three metallographic microstructures. The permeation tests have been performed in a modified Devanathan-Stachurski's cell with ad hoc experimental procedure. The experimental work may be divided into two parts. The first one has the aim of investigating on lattice and apparent diffusion coefficient in terms of reproducibility and physical meaning and its conclusions are summarized as follows:

- Charging transient (Devanathan and Stachurski's method standardized in ISO 17081) gives an apparent diffusion coefficient D_{app} strongly influenced by trapping effect and cathodic surface electrochemical alteration and at least it results one order of magnitude lower than lattice diffusion coefficient. D_{app} value is substantially insensitive to microstructural variations.
- D_{app} values do not fit theoretical Fick's curve. Diffusion coefficient values obtained at different points of the curves show values more than 25 times greater from the lowest ($D_{60\%}$) to the highest ($D_{1\%}$) with a decreasing trend.
- Cathodic potential analysis during charge phase underlines that tens of hours are required to obtain stationary potentials. The stationary potential values are dispersed in 0.2 V range.
- Diffusion coefficient measured during the first part of discharge is less influenced by trapping and electrochemical alterations, it is higher than D_{app} and slightly lower than D_L. It is sensitive to microstructural differences.
- Cathodic current partial charge and discharge procedure (Zakroczymski's method) shows less experimental data dispersion, it gives experimental curves perfectly symmetric (intrinsic reproducibility) which follow diffusion Fick's laws, i.e. no trapping processes. The obtained D values can be reasonably assumed as "true" lattice diffusion coefficient of materials. These values are sensitive to microstructural variations.
- Cathodic potential during partial charge and partial discharge is stable and changes very quickly during current modifications. It confirms Zakroczymski's assumption of cathodic electrochemical equilibrium during this phase.

The second part involves the investigation of the existing differences among three microstructures. The main results are:

- Martensitic X65 steel has D_L about 3 times lower than quenched and tempering (as received) X65 steel and about 14 times lower than annealed X65 steel.
- The amount of total, reversibly trapped and lattice hydrogen inside the samples has been calculated for the three microstructures in a quantitative way. The quenched samples store the lowest quantity of total and trapped hydrogen, the

quenched and tempered ones are in the middle and the annealed ones have the maximum storage capability.

In conclusion, the experimental procedure adopted in this project leads to reliable and meaningful results in permeation phenomena because it succeeds in eliminating disturbing elements such as the electrochemical alteration and in separating lattice related events from the trapping ones.

BIBLIOGRAPHY

[1] Nace Mr0175/ISO 15156-2 2009.

[2] **M. Ormellese**'s course, "Corrosion Engineering", A.A. 2011-2012.

[3] **P. Fassina, F. Bolzoni, G. Fumagalli, L. Lazzari, L. Vergani, A. Sciuccati,** "Influence of hydrogen and low temperature on pipeline steels mechanical behaviour of two pipeline steels", *Engineering Fracture mechanics*, V 81 (2012), pp. 43-55, ISSN 0013-7944.

[4] **P. Fassina, L. Lazzari, F. Brunella, G. Re, L. Vergani, A. Sciuccati**, "Fatigue Behavior of Pipeline Steel Under Hydrogen Environment and Low Temperature", 11th international Conference on the Mechanical Behavior of Materials, *Procedia Engineering*, V 10, Elsevier (2011), pp. 3354 - 3361 ISSN 1877-7058.

[5] **P. Pedeferri**, "Corrosione e protezione dei materiali metallici", vol. 2 , *Polipress,* 2007.

[6] **EFC Pubblications**, "Guidelines on materials requirements for carbon and low alloy steels for H2S-containing environments in oil and gas production", Number 16, second edition, *Maney*, 2002.

[7] **L. Lazzari**, "Encyclopedia of Hydrocarbons", Treccani, chapter 9, pp 485-501.

[8] **P. Fassina, F. Bolzoni, G. Fumagalli, L. Lazzari, L. Vergani, A. Sciuccati**, "Influence of hydrogen and low temperature on pipeline steels mechanical behaviour", Proceedings of 11th International conference of the Mechanical Behaviour of Materials, Procedia Engineering, Vol. 10, *Elsevier,* (2011), pp. 3354-3361.

[9] **L. Vergani, A. Sciuccati, G. Re, F. Bolzoni**, "Effect of hydrogen environment on fatigue behaviour of high toughness steels - Fatigue crack growth: mechanisms, behaviour and analysis", Editors: P. Tang and J.L. Zhang, *NOVA Publishers* (2012).

[10] API Standard 579-1/ASME FFS-1, Fitness-For-Service, Second Edition (2007).

[11] **M. Nagumo**, “Function of Hydrogen in embrittlement of high strength steels”, *ISIJ International*, Vol. 41, 2001, pp 590-598.

[12] **B. E. Wilde, C. D. Kim**, "The kinetics of hydrogen absorption and evolution on a carbon-manganese steel exposed to acidified solutions of sodium chloride", *Corrosion– NACE*, Vol. 37, no.8, 1981, 449-455.

[13] **A. Kawashima, K. Hashimoto, S. Shimodaira**, "Hydrogen Electrode Reaction and Hydrogen Embrittlement of Mild Steel in Hydrogen Sulfide Solutions", *Corrosion NACE*, Vol. 32, 1976, 321-331.

[14] **R.D. McCright**, "Effects of environmental species and metallurgical structure on the hydrogen entry into steel - Stress corrosion cracking and hydrogen embrittlement of iron base alloys",*NACE*, Vol. 5, 1977, 306-325.

[15] **R. Hudson**, *Corrosion*, 20, 1969.

[16] **R. McCright, R. Staehle**, "Effect of Arsenic upon the Entry of Hydrogen into Mild Steel as Determined at Constant Electrochemical Potential" *J. Electrochem Soc.*, Vol. 121, 1974, pp 609-618.

[17] **J. Newman, L. Shreir**, "Role of hydrides in hydrogen entry into steel from solutions containing promoters", *Corrosion Science*, Vol. 9, 1969, pp 631-441.

[18] **D Kiuchi, R. B. McLellan**, *Acta Met.* 31,961 (1983).

[19] **A. Turnbull**, "Hydrogen transport and cracking in metals", *The Institute of Materials Teddington*, UK, (1994), pp. 129.

[20] **A. H. M. Krom, A. Bakker**, "Hydrogen trapping models in steel", *Metall. And mat. Trans. B*, V 31B (2000), pp. 1475.

[21] **ISO 17081**, "Method of measurement of hydrogen permeation and determination of hydrogen uptake and transport in metals by an electrochemical technique", 1st edition (2004).

[22] **A. Turnbull, M. W. Carroll, D. H. Ferriss**, "Analysis of hydrogen diffusion and trapping in a 13% chromium martensitic stainless steel", *Acta metall.* V. 37, No. 7, (1989), pp. 2039-2046.

[23] **A. Turnbull, M. Saenz De Santa Maria, N.D. Thomas**, "The effect of H2S concentration and pH on hydrogen permeation in AISI 410 stainless steel IN 5% NaC1", *Corrosion science*, V 29 (1989), pp. 89-104.

[24] **N. Boes, H. Zuchner**, "Electrochemical methods for studying diffusion, permeation and solubility of hydrogen in metals", *Journal of less-common metal*, 49, 223 (1976).

[25] **M. A. V. Devanathan, Z. Stachurski**, “The adsorbtion and diffusion of electrolytic hydrogen in palladium”, *The Royal Society*, 1962.

[26] **J.B. Leblond, D. Debois**, "A general mathematical description of hydrogen diffusion in steels I. Derivation of diffusion equations from boltzmann-type transport equations", *Acta Met.* 31, 1459 (1983).

[27] **J.B. Leblond, D. Debois**, "A general mathematical description of hydrogen diffusion in steels II. Numerical study of permeation and determination of trapping parameters", *Acta Met.* 31, 1471 (1983).

[28] **A. McNabb, P. K. Foster**, "A new analysis of the diffusion of hydrogen in iron", *J. Trans. metallurgical Soc. AIME*, V 227, (1963), pp. 618-627.

[29] **R. A. Oriani**, "The diffusion and trapping of hydrogen in steel", *Acta metall.*, V 18, (1970), pp. 147-157.

[30] **L. Nanis, T.K. G. Namboodhiri**, "Mathematics of the Electrochemical Extraction of Hydrogen from iron", *Electrochemical Science and Technology*, vol. 199, (1972), pp. 691-694.

[31] **M. Iino**, "A more Generalized Analysis of Hydrogen Trapping", *Pergamon Press*, (1982), pp. 367-375.

[32] **G. M. Pressouyre and I. M. Bernstein,** "Quantitative analysis of H trapping", *Metallurgical transactions A*, V 9a (1978), pp. 1571-1580

[33] **G. M. Pressouyre,** "Trap theory of hydrogen embrittlement", *Acta metallurgica*, Vol 28 (1979), pp 895-911.

[34] **R. A. Oriani,** "The physical and metallurgical aspects of hydrogen in metals", *Fourth International Conference on Cold Fusion.*(1993), pp. 1-42

[35] **N. Parvathavarthini, S. Saroja, R. K. Dayal ,H. S. Khatak,** " Studies on hydrogen permeability of 2.25% Cr-1% Mo ferritic steel: Correlation with microstructure", *Journal of Nuclear Materials*, Vol. 288, Issues 2-3, (2001), pp 187-196.

[36] **S. Frappart, X. Feaugas, J. Creus, F. Thebault, L. Delattre, H. Marchebois**, "Study of the hydrogen diffusion and segregation into Fe-C-Mo Martensitic HSLA steel using electrochemical permeation test", *Journal of Physics and Chemistry of Solids*, Vol. 71, (2010), pp 1467-1479.

[37] **W. C. Luu, J. K. Wu**, "The influence of microstructure of hydrogen transport in carbon steels", *Corrosion science*, Vol. 38, No. 2, (1996), pp 239-245.

[38] **R. Réquiz, S. Camero, A. Rivas,** " Relationship between microstructure and hydrogen permeation of a plastic deformed seamless carbon steel pipe", *NACE corrosion 2010*, Paper no. 10181, (2010).

[39] **G. T. Park, S. U. Koh, H. G. Jung, K. Y. Kim**, " Effect of microstructure on the hydrogen trapping efficiency and hydrogen induced cracking of linepipe steel", *Corrosion Science*, 50, (2008), pp 1865-1871.

[40] **A. J. Haq, K. Muzaka, D. P. Dunne, A. Calka, E. V. Pereloma**, "Effect of microstructure and composition on hydrogen permeation in X70 pipeline steels", *Int. Journal of Hydrogen Energy*, 38, (2013), pp 2544-2556.

[41] **M. F. Stevens, I. M. Bernstein**, "Microstructural Trapping Effect on Hydrogen Induced Cracking of a Microalloyed Steel", *Metallurgical transaction*, Vol. 20A, 1989, pp. 909-919.

[42] **P. Manolatos, M. Jerome, J. Galland,** "Necessity of a palladium coating to ensure hydrogen oxidation during electrochemical permeation measurements on iron", *Electrochemical Acta,* V 40 (1995), pp. 867-871.

[43] **C. Ly, M. Jerome, J. Sojka, N. Ruscassier, J. -B. Guillot**, "Hydrogen permeation in different high strength steels. Influence of the microstructure", *EUROCORR*, 2008.

[44] **C. F. Dong, X. G. Li, Z. Y. Liu, Y. R. Zhang**, "Hydrogen-induced cracking and healing behaviour of X70 steel", *Journal of Alloys and Compounds,* 484, (2009), pp. 966–972.

[45] **C.F. Dong, Z.Y. Liu, X.G. Li, Y.F. Cheng**, "Effects of hydrogen-charging on the susceptibility of X100 pipeline steel to hydrogen-induced cracking", *Int. Journal of hydrogen energy*, Vol. 34, (2009), pp. 9879-9884.

[46] **V.P. Ramunni, T. De Paiva Coelho, P.E.V. de Miranda**, " Interaction of hydrogen with the microstructure of low-carbon steel", *Materials Science and Engineering*, 435–436, (2006), pp 504–514.

[47] **X. Yuan**, " Precipitates and hydrogen permeation behavior in ultra-low carbon steel", *Materials Science and Engineering*, 452–453, (2007), pp 116–120.

[48] **J. Woodtli, R. Kieselbach,** " Damage due to hydrogen embrittlement and stress corrosion cracking", *Engineering Failure Analysis*, 7, (2000), pp 427-450.

[49] **C.H. Norena, P. Bruzzoni**, " Effect of microstructure on hydrogen diffusion and trapping in a modified 9%Cr–1%Mo steel", *Materials Science and Engineering*, 527, (2010), pp 410–416.

[50] **ISO 17081,** "Method of measurement of hydrogen permeation and determination of hydrogen uptake and transport in metals by an electrochemcal technique", 1st edition (2004)

[51] **J. Kittel, F. Ropital, J. Pellier,** "New insight into hydrogen permeation in steel: measurements through thick membranes", *NACE Corrosion 2008*, Paper No. 08409.

[52] **T. Zakroczymski and J. Flis,** "Impedance characterization of the activation of iron surface for hydrogen entry from alkaline solution", *Electrochimics Acta,* Vol. 41. Nos. l/8. (1996), pp. 1245-1250,

[53] **J. Flis, T. Zakroczymski, V. Kleshnya1 1, T. Kobiela, R. Dus',** "Changes in hydrogen entry rate and in surface of iron during cathodic polarisation in alkaline solutions", *Electrochimica Acta*, V 44 (1999) pp. 3989-3997

[54] **A. Gajek, T. Zakroczymski,** "Long-lasting hydrogen evolution on and hydrogen entry into iron in an aqueous solution", *J. of Electroanalytical Chemistry,* V 578 (2005) pp. 171-182

[55] **S. Duval, R. Antaño-lopez, C. Scomparin, M. Jerome, and F. Ropital1, "**Hydrogen Permeation through ARMCO Iron Membranes in Sour Media", *Corrosion 2004,* NACE International p No 04740

[56] **H. Addach, P. Berçot b, M. Rezrazi, J. Takadoum,** "Study of the electrochemical permeation of hydrogen in iron", *Corrosion Science,* V 51 (2009) pp. 263–267

[57] **E. Fallahmohammadi, F. Bolzoni, L. Lazzari.** "measurament of lattice and apparent diffusion coefficient of hydrogen in X65 and F22 pipeline steels", *International journal of hydrogen energy,* V 38 (2013), pp 2531-2543.

[58] **T. Zakroczymski,** "Electrochemical determination of hydrogen in metals", *J. of Electroanalytical Chemistry,* V 475 (1999), pp. 82-88

[59] **T. Zakroczymski,** "Adaption of the electrochemical permeation technique for studying entry, transport and trapping of hydrogen in metals", *Electochemica Acta* V 51 (2006), pp. 2261-2266.

[60] **T. Zakroczymski, Z. Szklarska-Smialowska**, "Activation of the iron surface to hydrogen absorption resulting from a long cathodic treatment in NaOH", *Journal of the Electrochemical Society,* Volume 132,(1985), pp 2548-2552.

[61] **A.Monti**, "Diffusione di idrogeno in pipeline per acciai", Master of science thesis, A.A. 2010-2011.

[62] API specification 5L, "Specification for line pipe", 2004.

ANNEX I

Table I: Material and hydrogen permeation data. Legenda: current density = i (mA cm^{-2}), potential = E vs SHE (mV), a = anodic, c = cathodic, apparent diffusion coefficient = D (10^{-10} m^2 s^{-1}), hydrogen apparent concentration = $C_{app\ H}$ (mol m^{-3}), hydrogen flux at stationary state • thickness = $J_{ss\ H}$ L (10^{-10} mol m^{-1} s^{-1}).

ref. no.	steel type	strutture or thermal treatment	thickness / coating	T (°C)	anodic electrolyte	cathodic electrolyte	i_c or E_c	E_a	D_{app}	C_{app}	$J_{SS\ H}$ L
[37]	Mild steel	Annealed	1 mm / Ni	25	0.1 NaOH + 1g L^{-1} Na_2S • 9 H_20	0.1 NaOH + 1g L^{-1} Na_2S • 9 H_20	10	250	10.5	0.44	4.67
	S45C	Annealed							2.96	1.18	3.49
		Normalized							2.78	1.29	3.58
		Spheroidized							3.50	1.13	3.93
		Quenched							0.37	4.92	1.82
[39]	X65	F + AF (M/A=5.73)	1 mm / Pd	n.a.	0.1 N NaOH	NACE solution	0.5	250	4.05	20.91	84.7
		F + B (M/A=4.45)							4.44	27.13	120
		F + DP (M/A=1.28)							9.27	14.33	133
		F + DP (M/A=0.88)							9.38	13.79	129
[44]	X70	F + AF	0.77 mm / Ni	Troom	0.1 N NaOH	0.5 M H_2SO_4 + 250 mg/L As_2O_3	0.5	300	0.263	28.8	7.6
[45]	X100	F + B	0.5 mm / Ni	20	0.1 N NaOH	0.5 M H_2SO_4 + 250 mg/L As_2O_3	10	300	0.01	134	1.4
[38]	X52	As received	1 mm / Pd	n.a.	0.1 M NaOH	0.1 M Na_2SO_4	***-900***	150	0.3	-	-
		Normalized							1	-	-
		Annealed							0.9	-	-
		Quenched							0.38	-	-

ref. no.	steel type	strutture	thick / coat.	T (°C)	anodic electrolyte	cathodic electrolyte	i_c or E_c	E_a	D_{app}	C_{app}	$J_{SS\ H}$ L
[43]	Low alloyed steel	F + M (rare)	0.5-1.5 mm / Pd	n.a.	0.1 N NaOH	H_2SO_4	10	250	Bu: 10; D: 29	-	-
	VHS steel A	F + M(very low A)							Bu: 0.9; D: 1.6	-	-
	VHS steel B	F + M and/or A							Bu: 0.5; D: 0.9	-	-
	VHS steel C	F + M + B + A							Bu: 0.2; D: 0.4	-	
[40]	X70 Edge	F + P	1 mm	21 -23	0.1 N NaOH	0.1 N NaOH + $Na_2S\cdot H_2O$	3.52	-	1st 1.97 ± 0.09	0.84	1.66 ± 0.25
									2nd 1.77 ± 0.06		
	X70 Centreline	F + P						-	1st 2.25 ± 0.19	0.74	1.65 ± 0.23
									2nd 2.06 ± 0.17		
	MX70 Edge	F + P						-	1st 1.70 ± 0.04	1.2	1.95 ± 0.25
									2nd 1.57 ± 0.03		
	MX70 Centreline	F + P						-	1st 1.71 ± 0.01	0.90	1.55 ± 0.35
									2nd 1.52 ± 0.03		
	X70 TB Edge	F + B						-	1st 2.10 ± 0.19	0.80	1.67 ± 0.16
									2nd 1.33 ± 0.31		
	X70 TB Centreline	F + Granular B						-	1st 3.05 ± 0.17	0.77	2.34 ± 0.20
									2nd 2.15 ± 0.30		
	Normalized TB	F + P						-	1st 4.01 ± 0.02	0.60	2.42 ± 0.03
									2nd 3.82 ± 0.13		

ref. no.	steel type	strutture	thick / coat.	T (°C)	anodic electrolyte	cathodic electrolyte	i_c or E_c	E_a	D_{app}	C_{app}	$J_{SS\,H}$ L
[46]	SAE 1008	F + fine P	1 mm	27	0.1 N NaOH	0.1 N NaOH	***-1100***	-	1st 2.19 ± 0.11	-	-
									2nd 2.62 ± 0.15	-	-
	SAE 1008	F + fine globular C						-	1st 3.47 ± 0.11	-	-
									2nd 3.94 ± 0.25	-	-
									3th 4.18 ± 0.18	-	-
	SAE 1008	F + fine carbides						-	1st 6.43 ± 0.40	-	-
									2nd 7.78± 0.39	-	-
									3th 8.01 ± 0.32	-	-
[35]	ASTM SA182 F22	M	1.5 mm / Pd	n.a.	0.1 N NaOH	0.5 M H_2SO_4 + 200 ppm As_2O_3	0.05	200	4.47 ± 0.24	-	-
		B							5.19 ± 0.39	-	-
		F + globular B							40.00 ± 2.98	-	-

Bu: BUILD-UP = charge; D:DECAY= discharge; F: FERRITE; B: BAINITE; P:PEARLITE; DP: DEGENERATE PEARLITE; A: AUSTENITE; M:MARTENSITE; C: CEMENTITE